Time-Resolved Photoluminescence Studies Of GaAs-AlGaAs Quantum Well Structures

Richard Eccleston

A thesis submitted to the University of London for the degree of Doctor of Philosophy and Diploma of Imperial College.

Solid State Experimental Physics Group,
Department of Physics,
Imperial College of Science, Technology and Medicine,
LONDON.
SW7 2BZ.

June 1989.

Abstract

This thesis describes time-resolved photoluminescence measurements which have been made on GaAs-AlGaAs quantum well structures.

In particular, measurements are reported in a strongly coupled double quantum well structure as a function of externally applied perpendicular electric field and temperature. The excitonic radiative lifetime was found to increase with field at a rate ≈3 times faster than previously observed in single quantum well structures of the same overall width. The variation in lifetime was accurately modelled for the first time by an exciton envelope function calculation within the effective mass approximation. The agreement with calculation was found to be unaffected by changes in temperature in the range 4.2K to 27K, demonstrating the separability of the components of the exciton wavefunction describing the exciton centre of mass motion and the relative motion of the electron and hole. The temperature dependence of the exciton lifetime was successfully modelled for the first time using coherence area arguments, allowing the spatial extent of interface fluctuations to be determined.

Measurements are also reported on the variation of radiative lifetime in quantum wells as a function of injected free carrier density. A reduction in radiative lifetime was observed, attributable to the presence of electron-hole correlation within the degenerate free carrier sea. The lifetime data was used to determine the electron g-

factor in the plane of the wells as a function of quantum well width.

CW PL measurements are reported on the effects of ion-implantation and rapid thermal annealling on quantum well structures. The data is used quantitatively with complementary TEM measurements to demonstrate the presence of inhomogeneous strain within the samples, originating from the silicon nitride capping layer.

The time-resolved photoluminescence studies were performed using a streak camera with a novel photomultiplier based read-out system. The design and construction of this system is described, and its performance evaluated.

Acknowledgements

It gives me great pleasure to thank the following:

My supervisor, Dr. Chris Phillips, for his invaluable expertise and constant enthusiasm during the course of this work.

The following people who collaborated in the research. Dr. Steve Andrews and the G.E.C. Hirst Research Centre, who provided the exciton envelope function calculations used in chapters 4 and 5, and all the samples studied during the course of this work. Dr. Richard Harley and co-workers at Southampton University, who allowed me to use their CW PLE and Hanle data described in chapter 5. Drs. E. Bithell and W.M. Stobbs of Cambridge University who provided the TEM measurements, and Dr. R. Gwilliam of Surrey University, who performed the Ion Implantation processing, in the work described in chapter 6.

All the members of the Solid State Experimental Physics Group who provided assistance of any sort during this research; and all those who participated in those sanity-preserving moments of levity at one time or another.

Peter, Jean and Philippa Eccleston; Annelise, Gerry, Keith, Steve, Stephen and Seggie; for love and support during the course of this work.

CONTENTS

Abstract.

Acknowledgements.

Contents.

1. Introduction to Time-resolved Photoluminescence as a means of investigating the properties of Quantum Well Structures

1.1 Introductory Remarks.

1.2 Review of fundamental Quantum Well Physics.

1.3 The use of TRPL to study Quantum Well Structures.

2. Theory

2.1 Introduction.

2.2 The relationship between time-resolved bandgap photoluminescence curves and physical parameters.

2.3 Theoretical Description of the exciton envelope function in quantum wells in the presence of an electric field perpendicular to the plane of the well.

2.4 The variation of exciton radiative recombination lifetime in quantum wells as a function of temperature.

2.5 The Properties of the Strongly Coupled Double Quantum Well Structure.

3. Description of the mode-locked Dye Laser and Streak Camera used for the TRPL studies and description and evaluation of a novel photomultiplier based Streak Camera Read-out System

3.1 Introduction.

3.2 The mode-locked dye laser system.

3.2.1 The mode-locking of the Argon Ion Laser

3.2.2 The mode-locking of the 375B Styryl-8 Dye Laser.

3.3 The Streak Camera system.

3.3.1 Principles of operation, and generation of the streak image in the current system.

3.3.2 The Streak Camera read-out system.

3.4 Comparison of Serial and Parallel Read-out Systems.

3.5 Conclusions.

4. Time-Resolved Photoluminescence studies of a Strongly Coupled Double quantum well structure as a function of Electric field and Temperature

4.1 Introduction.

4.2 Review of Previous TRPL studies of Quantum wells in perpendicular electric fields.

4.3 Details of the experimental arrangement for the TRPL studies, and Description of the CQW sample.

4.4 Results of the TRPL measurements on the coupled quantum well structure as a function of electric field at 4.2K.

4.4.1 Description and Interpretation of the Experimental Data.

4.4.2 Details of the lifetime modelling calculations.

4.4.3 Comparison between theory and experiment.

4.5 TRPL measurements on the coupled quantum well structure between 4.2K and 60K.

4.5.1 Description and Interpretation of the Experimental Data.

4.5.2 Theoretical modelling of $\tau(T)$.

4.6 Conclusions.

5. Time-Resolved Photoluminescence studies in quantum wells containing a significant free carrier density

5.1 Introduction

5.2 Description of sample and discussion of CW PLE spectra.

5.3 The PL lifetime measurements as a function of applied bias and temperature.

5.4 Explanation of the observed reduction in PL lifetime with increasing free carrier density.

5.5 Determination of the effective in-plane g-factor for electrons in a quantum well, using TRPL data to complement Hanle photoluminescence studies.

5.6 Conclusions.

6. The use of Photoluminescence and complementary TEM measurements to study the effect of Ion Implantation and Rapid Thermal Annealling treatment on a GaAs/AlGaAs Multiple quantum well

6.1 Introduction and description of sample processing.

6.2 Results of the PL measurements after implantation and

rapid thermal annealling treatment.

6.3 Quantitative comparison of the PL spectra with the TEM measurements.

6.4 Conclusions.

References.

CHAPTER 1 INTRODUCTION TO TIME-RESOLVED PHOTOLUMINESCENCE AS A METHOD OF INVESTIGATING THE PROPERTIES OF QUANTUM WELL STRUCTURES

1.1 Introductory Remarks

This thesis describes time-resolved photoluminescence measurements which have been performed on semiconductor quantum well structures. These structures consist of alternate ultra-thin layers of narrower and wider bandgap semiconductors. As a result of the discrepancy in bandgap, and if the layers are sufficiently thin (<300Å), electrons and holes within the narrower bandgap layer become confined to a quasi two-dimensional plane (fig. 1.1a). The spatial confinement quantum mechanically modifies many of the physical properties of the thin layer compared to the bulk semiconductor. Of particular relevance here is the behavior of the coulombically bound electron-hole or "exciton" state at the band-edge of the confined layer. Studies are restricted to the AlGaAs-GaAs quantum well system which has been the most extensively studied because of ease of growth. Techniques such as molecular beam epitaxy (MBE) and metallo-organic chemical vapour deposition (MOCVD) permit routine growth of these structures to a given specification with the accuracy of one atomic monolayer. Study of quantum well structures has in part been driven by the possibility of new electronic and optoelectronic device applications. Bearing particular relation to this work is the construction of novel electro-optical modulator and all-optical switching

devices [1.1] which offer the possibility of enhanced performance and easy integration with existing devices.

In this chapter the basic properties of quantum well structures are reviewed and the specific infomation that may be obtained from time resolved photoluminescence measurements is described.

1.2 Review of Fundamental Quantum Well Physics

In this section, the most general aspects of the physics of quantum wells are presented. Emphasis is placed on the linear optical and electro-optical properties which concern this thesis, the non-linear optical [1.2] and transport properties [1.3] of these systems are largely ignored.

Almost all basic quantum well physics stems from the near-two dimensional confinement of carriers within the narrower bandgap layer. In particular the optical properties of the quantum well become modified with respect to the bulk material. The principle features are:

(1) For a quantum well which is sufficiently thin (≈300Å for the GaAs-AlGaAs system), the allowed free carrier states in the valence band and conduction band become modified by confinement with respect to the bulk material [1.4]. The free carrier wave vector, and hence kinetic energy, in the direction perpendicular to the plane of the well becomes

quantised and the allowed free carrier states split into a series of quantised subbands (fig. 1.1a) with the kinetic energy quantised in the direction perpendicular to the plane of the well but allowed to vary freely in the plane of the well where the motion is unconfined (fig 1.1b). The degeneracy of the light and heavy hole valence bands is lifted because the confinement energy is a function of carrier effective mass. In the ideal 2D limit, the density of states is a constant within each subband, ie. proportional to E^0 (cf. $E^{+1/2}$ in the bulk), the result obtained by summing k-states of constant energy in 2D. The total density of states therefore becomes a series of steps which coincide with the onset of each quantised subband (fig. 1.1c).

(2) The transition probability, W, for an optical transition between valence band and conduction band states is also modified by the confinement. The transition rate is proportional to the square of the dipole matrix element connecting the initial and final state wavefunctions [1.5]:

ie. $$W\alpha|\underline{M}|^2 \qquad \text{eqn (1.1)}$$

where: $$\underline{M}=\langle\Phi_{cb}|\underline{H}'|\Phi_{vb}\rangle \qquad \text{eqn (1.2)}$$

Φ_{cb} is the initial (conduction band) wavefunction, Φ_{vb} is the final (valence band) wavefunction and $\underline{H}'$ is the perturbational Hamiltonian for optical transitions, given (assuming the photon wavevector to be negligibly small) by:

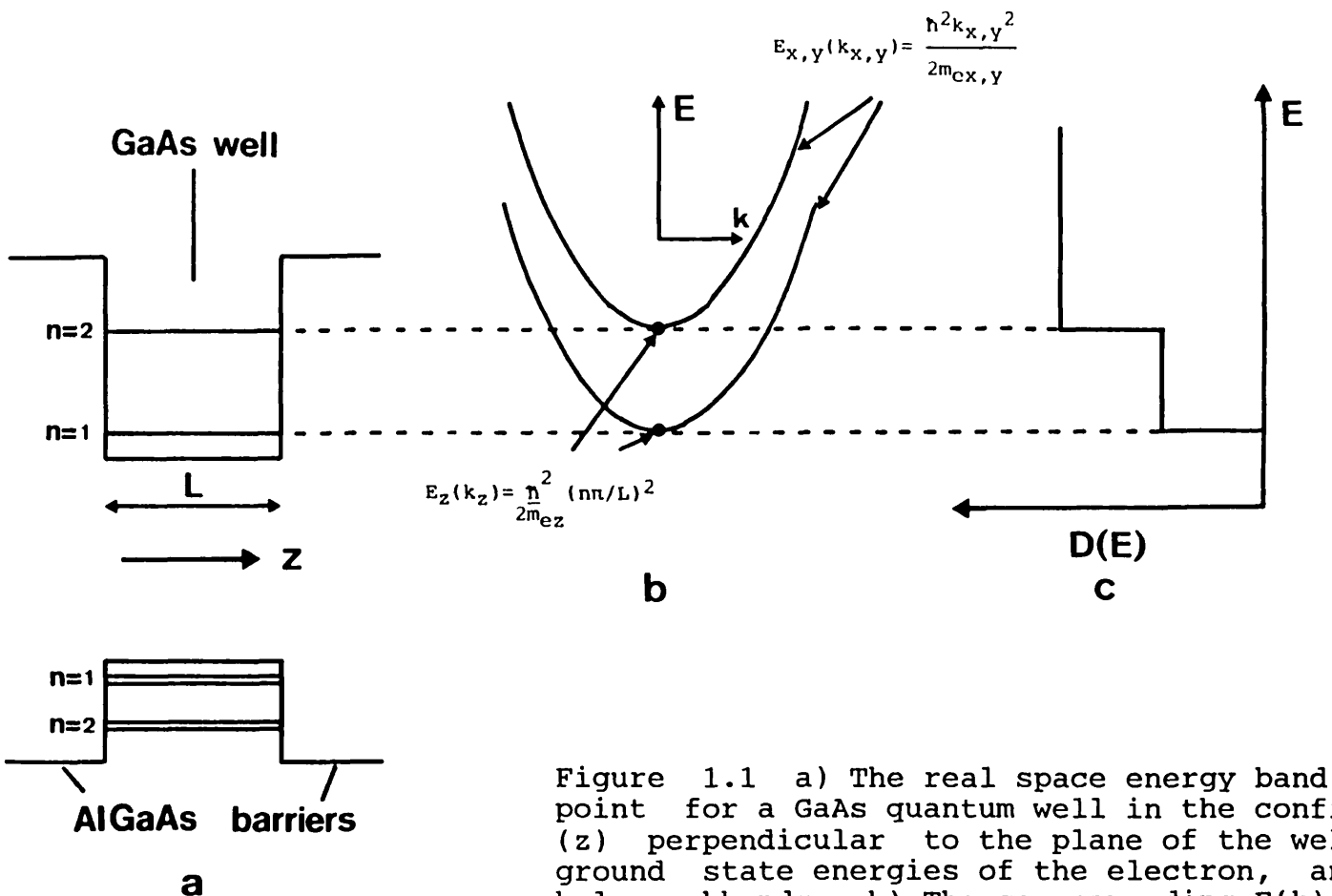


Figure 1.1 a) The real space energy band diagram at the Γ point for a GaAs quantum well in the confinement direction (z) perpendicular to the plane of the well, showing the ground state energies of the electron, and light and heavy hole subbands. b) The corresponding E(k) diagram for each electron subband, with E_z and k_z fixed in the confinement direction, but $E_{x,y}$ and $k_{x,y}$ freely varying in the plane of the well. c) The corresponding density of states function, D(E), for electrons in the conduction band, indicating the step-like density of states function, with D(E) constant within each 2D subband.

$$\underline{H'} = \frac{-eA}{2m_o c}\ \underline{a}.\underline{p} \qquad \text{eqn. (1.3)}$$

where $\underline{p}$ is the momentum operator, $A\underline{a}$ is the vector potential and m_o is the free electron mass.

The wavefunction components in the plane of the well are unconfined plane wave Bloch states, however the components of the wavefunctions in the direction perpendicular to the plane of the well (by convention the z direction) are confined by the barrier potentials. The wavefunction may be described most simply within the envelope function approximation whereby the wavefunction Φ, is assumed to be separable into the product of a bulk-like Bloch function, u, for a free carrier in the conduction or valence band, and an envelope function, $\varphi(z)$, which describes the confinement of the wavefunction in the z direction:

$$\text{ie.}\quad \Phi = \varphi(z).u \qquad \text{eqn. (1.4)}$$

$\varphi(z)$ is the solution to the 1D Schroedinger equation for the confinement potential $V_{cb}(z)$ or $V_{vb}(z)$ for electrons and holes in the conduction band and valence band respectively. Figure 1.2 indicates the form of the sine-like envelope function solutions for a quantum well with two confined subbands (light hole envelope functions omitted for clarity).

Substituting eqn. (1.4) into eqn. (1.2) gives:

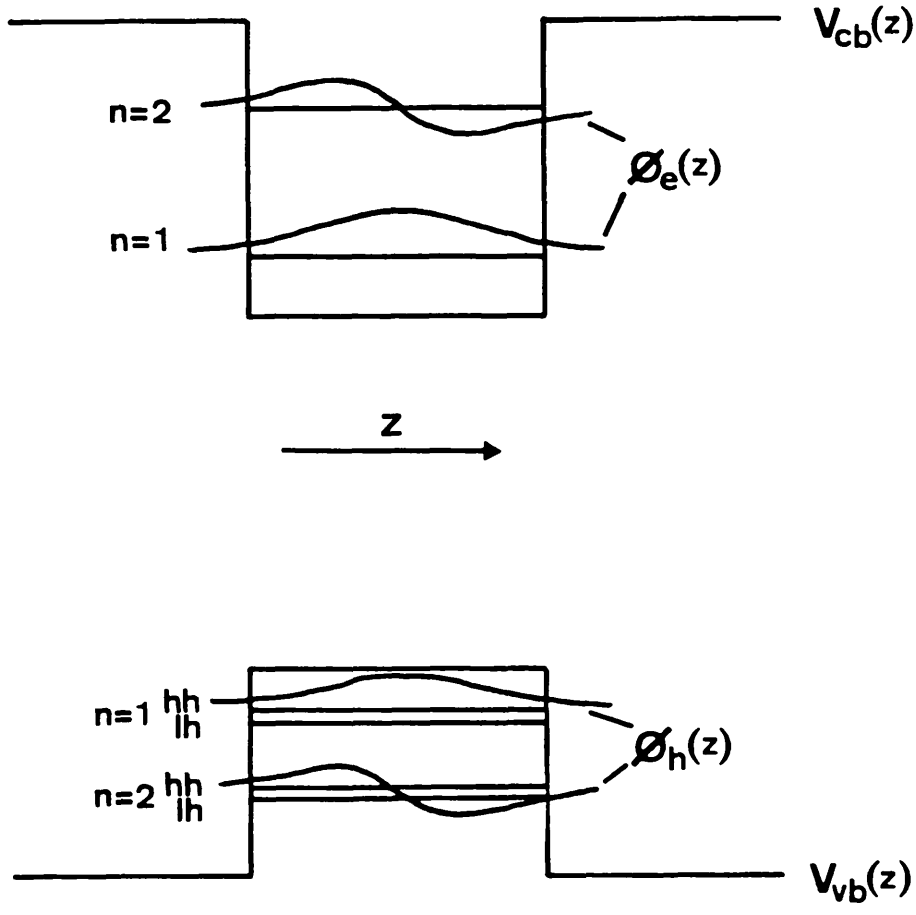


Figure 1.2 The real space energy band diagram in the z direction for a quantum well in zero external electric field with two confined subbands in the valence band and conduction band, indicating the sine-like envelope functions $\varphi_e(z)$ and $\varphi_h(z)$ for the n=1 and n=2 electron and heavy hole bands.

$$\underline{M} = \langle \varphi_e(z) | \varphi_h(z) \rangle \langle u_{cb} | \underline{H}' | u_{vb} \rangle + \langle u_{cb} | u_{vb} \rangle \langle \varphi_e(z) | \underline{H}' | \varphi_h(z) \rangle \qquad \text{eqn. (1.5)}$$

The second term may be considered negligibly small, since $\underline{H}'$ contains a d/dz operator and the $\varphi(z)$ envelope functions may be assumed to be slowly varying with respect to the Bloch functions. In the first term $\langle \varphi_e(z) | \varphi_h(z) \rangle$ is the overlap integral between the initial and final state envelope functions and the $\langle u_{cb} | \underline{H}' | u_{vb} \rangle$ term is equivalent to the bulk matrix element without confinement (eqn.(1.2)). The overlap integral $\langle \varphi_e(z) | \varphi_h(z) \rangle$ becomes very small for transitions between subbands of different subband index, n, because in this case the sine-like envelope functions are nearly orthogonal. As a result, optical transitions are only strongly allowed between subbands of the same n.

In the bulk, the matrix element $\langle \Phi_{cb} | \underline{H}' | \Phi_{vb} \rangle$ may be reduced to the momentum matrix element $\langle u_c | \underline{p} | u_v \rangle$ [1.5][1.6], where u_c, u_v are the cell periodic components of the initial and final state Bloch functions in the conduction and valence bands and $\underline{p}$ is the momentum operator. An oscillator strength, proportional to the transition probability, W, may be defined:

$$f_o = \frac{2 | \langle u_c | \underline{p} | u_v \rangle |^2}{\hbar w m_o} \qquad \text{eqn. (1.6)}$$

Making the assumption that the cell periodic components of the Bloch functions are unaffected by confinement, the same procedure may be followed for 2D, with $\langle \Phi_{cb} | \underline{H}' | \Phi_{vb} \rangle$ replaced by $\langle u_{cb} | \underline{H}' | u_{vb} \rangle \langle \varphi_e(z) | \varphi_h(z) \rangle$ from eqn. (1.5). The

quasi 2D oscillator strength for free carrier transitions in a quantum well (excluding exciton effects) is then given by:

$$f_{2D}=f_o \times |\langle\varphi_e(z)|\varphi_h(z)\rangle|^2 \qquad \text{eqn. (1.7)}$$

As required, f_{2D} becomes very small for transitions between subbands of different n. The form of the 2D density of states (fig. 1.1c) and the $\delta n=0$ selection rule, result in the 2D joint optical density of states for free carrier transitions adopting a similar step-like structure to the 2D density of states.

(3) The excitonic state within the confined layer is also substantially modified [1.4]. Confinement of the exciton wavefunction within the quantum well potential causes a decrease in the exciton radius and an increase in exciton binding energy (by a factor of four in the ideal 2D limit [1.2]). In 3D, the exciton wavefunction may be expressed as:

$$\Phi_x=\exp(i\underline{K}.\underline{R})\ \Phi_e(\underline{r}_e)\ \Phi_h(\underline{r}_h)\ \varphi_{eh}(\underline{r}_{eh}) \qquad \text{eqn. (1.8)}$$

where $\Phi_e(\underline{r}_e)$, $\Phi_h(\underline{r}_h)$ are the ground state wavefunctions of free electron or holes at the bottom of the conduction band and valence band, and the $\varphi_{eh}(\underline{r}_{eh})$ term is an envelope function which describes the binding between the free carriers. In the absence of this term the position and motion of the electron and hole would be uncorrelated. The vector , $\underline{r}_{eh}$, is the electron and hole separation: ie. $\underline{r}_{eh}=\underline{r}_e-\underline{r}_h$. The $\exp(i\underline{K}.\underline{R})$ term describes the centre of mass

motion of the exciton, where $\underline{R}$ is the centre of mass position vector and $\underline{K}$ is the wave vector describing the centre of mass motion. The transition probability for radiative recombination of the electron and hole within an exciton, described by the wavefunction of eqn (1.8), is given by [1.7]:

$$W_x \alpha \; |\langle \Phi_{cb} | \underline{H}' | \Phi_{vb} \rangle|^2 \; |\varphi_{eh}(0)|^2 \qquad \text{eqn. (1.9)}$$

Shinada and Sugano [1.8] have shown that this result remains true in the ideal 2D case, where φ_{eh} becomes the exciton envelope function in 2D. Apart from the constant factor $|\varphi_{eh}(0)|^2$, eqn. (1.9) is identical in form to eqn. (1.1). Following the same approach as for free carriers, the oscillator strength for exciton transitions in a quantum well is given by:

$$f_{ex} = f_o \; |\langle \varphi_e(z) | \varphi_h(z) \rangle|^2 \; |\varphi_{eh}(0)|^2 \qquad \text{eqn. (1.10)}$$

$|\varphi_{eh}(0)|^2$ is the probability of finding the electron and hole in the same unit cell, which increases as the exciton radius is reduced by the effect of confinement. A large increase in the exciton oscillator strength (a factor of 8 in the ideal 2D limit [1.2]) is therefore observed in quantum wells compared to the bulk value, although the ideal 2D limit is never achieved due to the finite well thickness and finite barrier height. The enhanced oscillator strength, coupled with greater separation from the continuum due to the enhanced binding energy, cause the exciton feature to

become more prominent in the absorption spectrum of the quantum well with respect to the bulk semiconductor. Furthermore carrier-phonon scattering is largely unaffected by confinement, so, in marked contrast to the bulk where exciton resonances are only observed at low temperatures due to thermal broadening, exciton features in a quantum well may be easily observed at room temperature. The combination of the 2D joint density of states for free carriers and the exciton resonances at each subband edge produce the typical optical absorption spectrum for a quantum well (fig. 1.3).

(4) Also of basic importance in this work is the so-called Quantum Confined Stark Effect (QCSE), first reported by Miller et al. [1.9], which describes the shift in exciton and subband energies in a quantum well under the application of an electric field perpendicular to the plane of the well. The shift is due to the modification of the confinement potentials by the field, as shown in fig. 1.4a. The most marked difference from the bulk is the behavior of the 2D exciton. In the bulk, an excitonic state is rapidly ionised under the application of a small electric field as the electron and hole are pulled in opposite directions, and any observable optical transition is destroyed by lifetime broadening. The Stark shift in the exciton ground state energy due to the modification of the coulomb potential by the electric field is limited to only ≈10% of the (bulk) binding energy before the lifetime broadening dominates and the transition may no longer be observed. However, for a

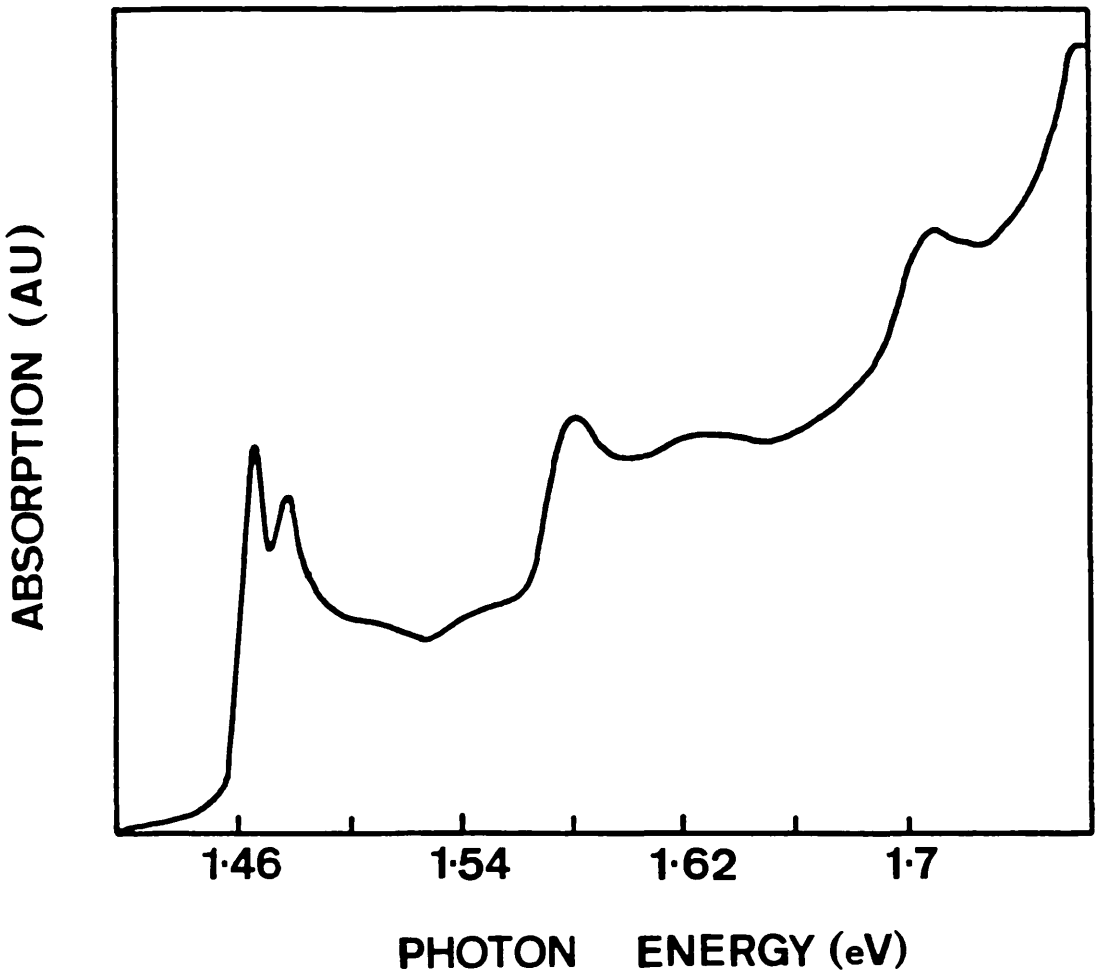


Figure 1.3 A typical absorption spectrum for a 100Å quantum well, illustrating the step-like structure of the joint optical density of states, and the heavy and light hole exciton resonances at the onset of each quantised subband. From ref. [1.2].

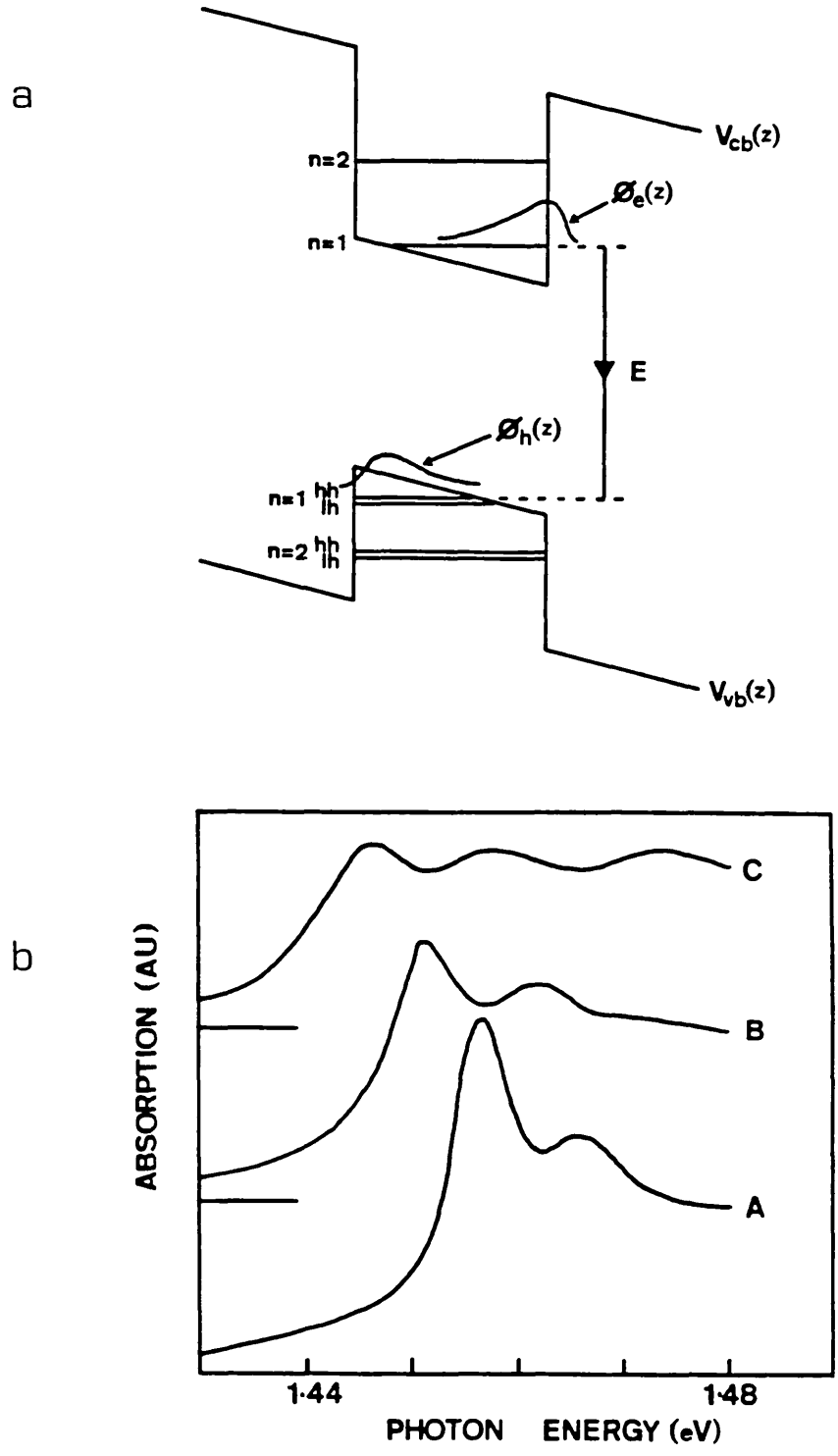


Figure 1.4 a) The modification of the confinement potentials in a quantum well in the presence of an electric field applied in the z direction, showing the displacement of the electron and hole wavefunctions to opposite sides of the well. The ground state transition energy, E, between the n=1 subband minima is reduced compared to the zero field value. b) Typical absorption spectra from a quantum well at room temperature at different values of perpendicular electric field, showing the "Stark shift" in the subband energies and the exciton resonances still clearly visible. Curve A: 10kV/cm. Curve B: 43kV/cm. Curve C: 73kV/cm. From ref.[1.1].

field applied perpendicular to the plane of a quantum well, the spatial separation of the electron and hole wavefunctions is limited by the confinement potentials of the valence band and conduction band (as indicated in fig. 1.4a). In this case the exciton resonance may persist to greatly increased applied field with small lifetime broadening, while the subband with which the exciton is associated shifts substantially in energy due to the modification of the form of the confinement potentials. In this way, so-called "quantum confined" Stark shifts in the exciton resonance position of 3-4 times the (confined) exciton binding energy may be observed (fig.1.4b), up to a factor of 100 greater than the bulk limit [1.1]. It is the modification of the transition wavelength of an exciton absorption resonance which persists to room temperature with large oscillator strength under the application of an external electric field which gives quantum well structures potential as electro-optic modulator devices. Miller et al. [1.1] have described room temperature single quantum well waveguide devices with modulation depths of 95% in a 100μm length with switching speeds of 100ps, and make reference to many other devices that have been reported.

1.3 The use of TRPL to study quantum well structures

In this section, the relationship of the current Time-Resolved Photoluminescence measurements (TRPL) to the basic

quantum well physics described above, is discussed. In a TRPL measurement, the semiconductor is excited by a very short pulse of light, typically of only a few picoseconds in duration and of photon energy greater than the bandgap. The temporal evolution of the luminescence emitted after photoexcitation is related to the characteristic radiative lifetime of the excited species, in this case, the exciton. The spectral evolution of the luminescence over time is related to the cooling of the photocreated carriers which may be out of thermal equilibrium with the lattice due to the excess photon energy given to the carriers above the bandedge [1.10].

The radiative lifetime, τ, of an excited electronic state is inversely proportional to the effective oscillator strength, f_{eff}, for that transition [1.11], ie.:

$$\tau \alpha 1/f_{eff} \qquad \text{eqn. (1.11)}$$

A measurement of τ therefore gives infomation about f_{eff}, which for a quantum well depends on the form of the envelope functions from eqn. (1.10). TRPL therefore provides a tool for testing proposed analytical forms for the envelope functions in quantum wells directly. Good accuracy is possible since τ may often be determined to within ±1% from fits to TRPL profiles over several orders of magnitude.

In these studies, a quantum well structure has been used to investigate the variation in exciton lifetime with perpendicular electric field. As has been discussed, the

application of such a field causes the electron and hole to move to opposite sides of the well (fig. 1.4a), although the quantum well potential constrains the complete separation of the electron and the hole and prevents the destruction of the exciton. From eqns. (1.7) and (1.11), a spatial separation of the electron and hole wavefunctions in the z-direction produces a decrease in the 2D oscillator strength because the overlap between the electron and hole envelope functions is reduced, and an increase in τ is predicted. Conversely, the quantitative variation of τ with field may be used to infer a form for the exciton envelope functions. In this thesis, measurements are described which test the forms of the exciton envelope functions which have been proposed. Accurate characterisation of these functions, particularly as a function of electric field, is an important requirement for reliable design of the novel electro-optical and non-linear optical modulators that may be constructed from these structures. As has been seen, the exciton envelope functions determine the oscillator strength for excitonic interband transitions and hence the absorption coefficient, which is required to model the modulation depth which may achieved in a device of a given size. It will be emphasised that accurate measurement of oscillator strength values is only possible in the case of samples which approach idealised behavior. Experiments are also described on samples where non-ideal character is prominent. In this case, some of the effects which may modify the lifetime data are described.

How does TRPL compare with other techniques for acquiring such infomation? As shown in section 2.3, modelling from Stark shift measurements alone is not strongly sensitive to the actual form of the free carrier envelope functions in the z direction, and almost independent of the form of the envelope function in the plane of the well. The variation in exciton binding energy in principle provides a more sensitive measure of the envelope functions. However, binding energy measurements from PLE (photoluminescence excitation) or absorption spectra have proved difficult to perform accurately in practice, because of the difficulty in separating the small change in exciton binding energy from the large subband shift at typical exciton linewidths. In any case, it will be shown that the sensitivity of radiative lifetime to electric field exceeds that of exciton binding energy by up to a factor of 40. Absorption measurements may in principle be used to estimate relative exciton oscillator strengths from integrated peak area measurements. However, the measurement is tightly restricted to samples of very high quality where broadening effects are small and the distinction between the subband continuum and the exciton resonances is clear. Miller et al. [1.1] achieved agreement within a factor of 2 at high fields for the variation of light hole oscillator strength (considering the variation in $\langle\varphi_e(z_e)|\varphi_h(z_h)\rangle$ alone) using this method. In comparison to these techniques, it is clear that TRPL provides a particularly suitable approach for determining exciton envelope functions in quantum wells.

CHAPTER 2 THEORY

2.1 Introduction

In this chapter, the basic concepts introduced in the preceding chapter are developed into those detailed theoretical considerations which are relevant to the experiments which are to be described. The theoretical formalism for the form of TRPL traces and their relation to physical parameters is presented. The various theoretical treatments which have been used to describe the exciton wavefunction in a quantum well, particularly as a function of electric field, are reviewed. The variation of the exciton lifetime with temperature is discussed. Finally the special characteristics of the strongly coupled double quantum well structure which has been used for some of these studies, are described.

2.2 The relationship between Time-resolved Bandgap Photoluminescence curves and physical parameters.

This topic has been most recently reviewed by Bimberg and Christen [2.1]. A measurement of the PL intensity with time after photoexcitation is a measurement of the first derivative with time of the concentration of the recombining species. However it is necessary to make a sharp distinction between the possible intrinsic radiative decay species: excitons and free electron hole pairs. Excitonic decay is the dominant intrinsic decay process in quantum wells at low

temperatures where kT is less than the exciton binding energy (ie. T<140K for a 10meV binding energy) and if the excited or doped carrier concentration is less than $10^{17}/cm^3$ [2.1] so that carrier screening of the electron-hole coulomb interaction may be neglected. Conversely, free carrier pair recombination dominates in the high density regime, $>10^{17}/cm^3$. In the high temperature, low doping regime, the origin of the decay is dependent on the excitation density since the enhanced probability of exciton recombination (due to electron hole binding) competes with the higher probability of free electron-hole formation. Unlike excitonic decay, the probability of free electron-hole pair recombination is excitation density dependent (and also produces non-exponential decays), so the dependence of the radiative decay "lifetime" on excitation density distinguishes between the two possibilities. The different decay dynamics which apply in these two cases are now explained in detail.

(1) Excitonic decay

Excitonic decay is a monomolecular process where a given electron - hole pair may be considered as a single particle state. This single particle decays with a characteristic lifetime τ, which is determined by the simple rate equation:

$$I(t) \alpha -\frac{d}{dt} N_{ex}(t) = \frac{1}{\tau} N_{ex}(t) \qquad \text{eqn. (2.1)}$$

where I(t) is the PL intensity after photoexcitation at

t=0, an $N_{ex}(t)$ is the number of photocreated excitons at time t.

In this case a simple exponential decay of luminescence intensity is obtained:

$$I(t) = I(0) \exp(-t/\tau) \qquad \text{eqn. (2.2)}$$

It is worth noting that, from eqn. (2.1), I(t) is proportional to the concentration of the recombining species, $N_{ex}(t)$. However, this is only true in the monomolecular case because it so happens that the exponential function is its own first derivative. In general, I(t) need not follow the variation of N(t), only its first derivative.

(2) Free-electron hole pairs

In the case of non-degenerate free electron hole pairs, the probability of an electron and hole recombining is proportional to the total concentration of electrons and holes (N and P), and proportional to a bimolecular recombination coefficient, α:

$$\text{ie:} \quad \frac{dn(t)}{dt} = -\alpha NP = \frac{dp(t)}{dt} \qquad \text{eqn. (2.3)}$$

In general, N and P are the sum of the background concentrations N_o and P_o and the photocreated populations n and p.

ie: $N=n+N_o$ eqn. (2.4)

$P=p+P_o$

So eqn. (2.3) becomes (n=p):

$$\frac{dn(t)}{dt} = -\alpha\,[(N_o+P_o)n(t) + [n(t)]^2] \qquad \text{eqn. (2.5)}$$

which has the solution:

$$n(t) = \frac{n(0)\exp(-t/\tau_\infty)}{1+[n(o)/(N+P)][1-\exp(-t/\tau_\infty)]} \qquad \text{eqn. (2.6)}$$

where: $\tau_\infty=1/\alpha(N_o+P_o)$

Two regimes may be identified. If a background carrier, electrons say, is present in concentrations which greatly exceed the photocreated concentration, an exponential decay is again predicted from eqn.(2.6), with a single lifetime proportional to N_o^{-1}. In this case, a measure of the lifetime becomes a measure of N_o. However, this argument applies only to non-degenerate majority carrier densities. If the majority carrier density is degenerate, the lifetime is independent of N_o because all states available for recombination are filled [2.2]. Finally, if $n,p >> N_o,P_o$ then:

$$n(t)=n(0)/[1+n(0)\alpha t] \qquad \text{eqn. (2.7)}$$

and a hyperbolic decay with a time varying "lifetime" is obtained.

In this way it may be seen that, where the doped carrier density is low with respect to the excited carrier density, excitonic recombination (assuming constant exciton temperature) may be distinguished by a single exponential decay in the PL emission intensity with a characteristic lifetime which is independent of excitation density.

This formalism assumes a purely radiative recombination of the photocreated population. In fact, in real semiconductors, recombination of an electron with a hole via non-radiative paths is also common, for example via an impurity, defect or interfacial state. In this case, the electron-hole or exciton concentrations are reduced faster than would be otherwise observed. For radiative and non-radiative processes which are both governed by exponential decay, the resultant luminescence decay profile is still exponential, however the measured luminescence lifetime, τ_{pl}, is reduced with respect to the true radiative lifetime:

$$1/\tau_{pl} = 1/\tau + 1/\tau_{nr} \qquad \text{eqn. (2.8)}$$

where τ_{nr} is the lifetime associated with the nonradiative rate.

2.3 Theoretical description of the exciton envelope function in quantum wells in the presence of an external electric applied perpendicular to the plane of the well

In this section the problem of the exciton envelope functions in a quantum well in the presence of a perpendicular electric field is presented in detail. The analytical and computational methods that have been used by other workers to model these envelope functions are reviewed. By means of comparison, evidence that the procedure adopted in this work is consistent with other methods is obtained.

2.3.1 General Formalism

Within the effective mass and envelope function approximations, the total exciton envelope function is given from eqns. (1.8) and (1.4) by:

$$\Phi_{ex} = \varphi_e(z_e)\ \varphi_h(z_h)\ \varphi_{eh}(r_{eh}) \qquad \text{eqn. (2.9a)}$$

where the centre of mass term has been omitted by assuming negligible photon wavevector so that by momentum conservation only excitons exactly at K=0 contribute to optical transitions. The effect of finite exciton coherence time which partly relaxes the K=0 selection rule is discussed in section 2.4. The Hamiltonian for an exciton in a quantum well in the presence of an electric field may be expressed by rewriting the Schroedinger equation in cylindrical polar relative and centre of mass co-ordinates

(r,Θ,z,R) where r is now the relative separation of the electron and hole in the x,y plane (ie. $r^2=x_{eh}^2+y_{eh}^2$) (r_{eh} is the total separation of the electron and hole) and R is the position vector of the exciton centre of mass. The Hamiltonian then becomes:

$$\begin{aligned}\underline{H}=&E_e(z_e) + V_{cb}(z_e) - eFz_e \\ &+E_h(z_h) + V_{vb}(z_h) + eFz_h \\ &+E_{eh}(r) - e^2/4\pi\varepsilon|\underline{r}_{eh}|\end{aligned} \qquad \text{eqn. (2.9b)}$$

where: $E_e(z_e)$ and $E_h(z_h)$ are the kinetic energy operators for the electron and hole (at z coordinates z_e and z_h) for motion in the z direction, given by [2.3]:

$$E_e= \frac{-\hbar^2}{2m_{ez}} \frac{d^2}{dz_e^2} \qquad E_h= \frac{-\hbar^2}{2m_{hz}} \frac{d^2}{dz_h^2}$$

$E_{eh}(r)$ is the kinetic energy for the relative motion of the electron and hole in the x,y plane at coordinate r :

$$E_{eh}= \frac{-\hbar^2}{2\mu}\left[\frac{d^2}{dr^2} + \frac{1}{r}\frac{d}{dr}\right]$$

μ is the reduced effective mass in the plane of the well, given by:

$$\mu = \frac{m_{exy}\, m_{hxy}}{m_{exy} + m_{hxy}}$$

where m_{ez}, m_{hz} and m_{exy}, m_{hxy} are the electron and hole effective masses parallel (xy) and perpendicular (z) to the plane of the well respectively, and F is the electric

field strength. The term in $d^2/d\Theta^2$ has been set to zero by assuming circular symmetry in the plane of the well, ie. only s-like envelope functions are considered for φ_{eh}, this assumption is discussed further later. The centre of mass kinetic energy term has been omitted because only excitons at K=0 are considered. The solution of eqn.(2.9a) at each field may be conveniently separated into a determination of the free carrier terms, $\varphi_e(z_e)$ and $\varphi_h(z_h)$, and a determination of the excitonic binding term, $\varphi_{eh}(r)$. These two aspects are now considered in turn.

(1) The free carrier envelope functions

$\varphi_e(z_e)$ and $\varphi_h(z_h)$ are the solutions of the Schroedinger equation in a 1D potential well in the presence of an electric field. For electrons in the conduction band, this may be expressed by collecting the free carrier terms in z from the Hamiltonian of eqn.(2.9b):

$$\underline{H} = \frac{-\hbar^2}{2m_{ez}} \frac{d^2}{dz_e^2} + V_{cb}(z_e) - eFz_e \qquad \text{eqn. (2.10)}$$

with an equivalent expression for holes in the valence band.

The problem is not analytically soluble, except in the case of infinite barriers where solutions given by Airy functions are obtained. In the more realistic case of finite barriers true bound state solutions do not strictly exist because the electron or hole may always tunnel to free

carrier states outside the well with finite tunnelling probability. However, if the field is not too strong then the tunnelling probability is low and the states may be considered "quasi-bound" and "real" wavefunctions may be computed justifiably. Bastard et al. [2.4] have derived an inequality to express this field regime, within which there is negligible penetration of the wavefunction into the barrier. A variety of approximate methods have been used to describe the finite barrier case; these are now discussed.

The technique that has been adopted in the work described here, and used by other authors [2.3] is the resonant tunnelling method. In this technique, the triangular confinement potential is modelled by a series of thin rectangular barriers. A set of matrices are calculated to describe the quantum mechanical transmission and reflection coefficients at successive interfaces for a plane wave of a given energy traveling along the +z direction. The product of this matrix set gives the tunnelling probability for the whole structure. Resonances in the tunnelling probability as the energy of the incident wave is varied denote the energies of the quasi-bound states within the structure, because the tunnelling probabilty will be enhanced at these values. A variational envelope function, which must however still be chosen, may be adjusted to fit the ground state energy which has been obtained. Miller et al. [2.3] have compared the resonant tunnelling calculation to more complicated variational and perturbational

calculations by Bastard et al. [2.4] which however use an infinite barrier well. They use a variational envelope function of the form:

$$\varphi_{e,h}=N(\beta)\ \cos\pi z/L\ \exp[-\beta[z/L+1/2]],\ |z|/L<1/2 \quad \text{eqn. (2.11)}$$

where β is a variational parameter and $N(\beta)$ is a normalisation constant.

Miller et al. find that good agreement may be achieved between the energy eigenvalues that may be obtained from the resonant tunnelling method and from the pure variational method with infinite barriers if an effective well width, L_{eff}, is used in the variational envelope function which is adjusted to compensate for the use of infinite barriers.

Alternatively, Bastard et al. extend their approach to finite barrier wells by allowing exponential penetration of the envelope function into the barrier. In this case $\varphi_{e,h}(z)$ becomes:

$$\varphi_{e,h}(z)=\begin{cases} A\ \exp[(q-\beta)[z/2+1/2], & z\leq -L/2 \\ B\ \sin[kz/L+\delta]\exp[-\beta z/L], & |z|\leq L/2 \\ C\ \exp[-(q-\beta)[z/L-1/2], & z\geq L/2 \end{cases} \quad \text{eqn. (2.12)}$$

where A,B,C are normalising constants found by matching φ and φ' at the interfaces.

More recently, Hong and Singh [2.5] have adopted a

purely numerical approach to the solution for φ by complete numerical integration of the 1D Schroedinger equation in the vicinity of the quantum well, requiring only that $\varphi=0$ and $d\varphi/dz=0$ for $z=\pm 2.5L$. In this case, no initial envelope function or energy need be assumed. Austin and Jaros [2.6][2.7] have used a numerical Airy function treatment which can be extended to finite barriers. In both these methods, the authors are able to extend their calculations to the region of significant tunnelling and consider more novel systems such as asymmetric and graded barriers. Saunders and Bajaj [2.8] have used a more complicated perturbation approach including finite barriers and valence band mixing. The calculations adopted in this work (described in detail in chapter 4) use the resonant tunnelling method to calculate the free carrier ground state energy and numerical integration of the Schroedinger equation at that energy to determine the envelope function. Again, in the case of numerical integration, no analytical variational envelope function need be assumed.

A comparison of the predicted ground state energy eigenvalues that are generated by these different approaches demonstrates broad agreement between the methods compared by Miller et al. and the more recent calculations. The Stark shift in the energy of an optical transition between the n=1 subbands, which is obtained by summing the individual shifts in the valence band and conduction band, shows a quadratic dependence with field at low field, which becomes closer to

a linear variation at higher fields. It should be noted however that close agreement between the energy eigenvalues generated by the different techniques need not imply that the envelope functions will themselves be similar, since different trial envelope functions or purely numerical methods have been used. This is of significance here because it is the form of the wavefunction which determines the overlap integral and hence the radiative lifetime of the state.

(2) The electron-hole binding term

In the case of the $\varphi_{eh}(r_{eh})$ binding term, a 1s-type wavefunction form, which follows from the hydrogenic nature of the exciton state, may be adopted. Only s states need be considered because higher angular mommentum states have $|\varphi_{eh}(0)|^2=0$ and so the oscillator strength for inter-band transitions vanishes for these excited states from eqn. (1.7). Higher s states may be neglected because $|\varphi_{eh}(0)|^2$ in 2D is 27 times greater for a 1s wavefunction compared to a 2s wavefunction [1.2], and in any case at the low temperatures of interest here (<60K and principally 4.2K) few higher s states will be occupied. Φ_{ex} therefore becomes (dropping the suffixes in z for clarity):

$$\Phi_{ex}= \sqrt{(2/\pi)}\ \varphi_e(z)\ \varphi_h(z)\ 1/a\ \exp(-r_{eh}/a) \quad \text{eqn (2.13)}$$

where the 1/a term is required for wavefunction

normalisation and a is a variational parameter which determines the spatial extent of φ_{eh}, that is , the effective exciton Bohr radius.

A further simplification is possible. By assuming that the confinement of the electron-hole pair in the z-direction due to the barrier potentials is much greater than that due to coulombic binding, the z dependence in the binding term may be dropped and r_{eh} becomes r, the electron-hole separation in the plane of the well, a function of x and y only. The z-dependence of the exciton wavefunction is then expressed solely by φ_e and φ_h. Φ_{ex} now becomes mathematically separable in z, which is analytically more convenient. Bastard et al. [2.9] have performed a detailed comparison of the separable and non-separable solutions in zero electric field but as a function of well width. They find negligible difference in the exciton binding energy obtained from the two solutions for well widths less than 400Å. For wider wells, the confinement of the electron-hole pair by the barrier potentials becomes comparable to or less than that due to coulombic binding and the separable solution becomes progressively less accurate. For very narrow wells with finite barriers, the energy of the confined ground state increases such that significant penetration of the barrier occurs. Again the spatial confinement of the carriers by the barrier potential becomes less than the coulombic binding and again the separable solution becomes inaccurate. Given similar restrictions, the separable solution treatment may be extended to the non-zero

field case, although the allowed well width regime may be modified by the field.

The value of a, and hence the exciton binding energy, E_{be}, is obtained by minimising the expectation value of the hamiltonian of eqn.(2.9), <E>, with respect to a and any other variational parameters in φ_e and φ_h. The exciton binding energy is determined by subtracting <E> from the free particle wavefunction energies. For a 100Å well with φ_e,φ_h in the form of eqn.(2.12), and the separable form for φ_{eh}, Brum and Bastard [2.10] have obtained an additional value of E_{be} by keeping the variational parameters in φ_e and φ_h fixed at their free carrier values. This is value is shown to be within 1.5% of the value obtained from the full variational method, which expresses again that the z-dependence of the exciton wavefunction is dominated by the barrier potentials. In the current work, a 1s type envelope function is adopted (eqn. (2.13)), however both the separable and non-separable forms are considered.

In all the studies, a reduction in exciton binding energy with increasing electric field is predicted, consistent with an increase in the separation of the electron and hole. However, in addition to the separation of the electron-hole pair in the z direction which is to be expected from the free carrier wavefunctions alone, a spatial separation is also observed in the plane of the well orthogonal to the field: that is, a increases with field. This effect is

closely analogous to the in-plane increase in exciton radius as a function of well width at zero field [2.9].

Some of the binding energy calculations that have been described have been recently compared by Nojima [2.11]. In each case the separable form of φ_{eh} has been used with no z dependence. The calculations are distinguished by the different methods that have been used to obtain φ_e and φ_h. Upon correcting algebraic errors in the treatment of Miller et al., the author shows (fig. 2.1) that the treatments of Hong et al. (numerical integration), Brum and Bastard (variational minimisation of φ_e, φ_h in the finite well case), Bajaj and Saunders (including valence subband mixing) and Miller et al. (resonant tunnelling method and variational matching to eqn (2.11)) all produce similar variations for E_{be} with electric field. Also indicated in figure 2.1 is the result using the method adopted in this work for a 100Å single quantum well, demonstrating close agreement with other methods. The differences are attributed to the different effective mass values that have been adopted (these are not accurately known) and the variation in aluminium molar fraction, x, which affects the AlGaAs barrier height. This agreement is significant as far as a calculation of the variation of radiative lifetime with electric field is concerned. As has been discussed, the similarity in the Stark shifts predicted by the different methods need not imply that the variation in radiative lifetime will also be the same. However, the binding energy

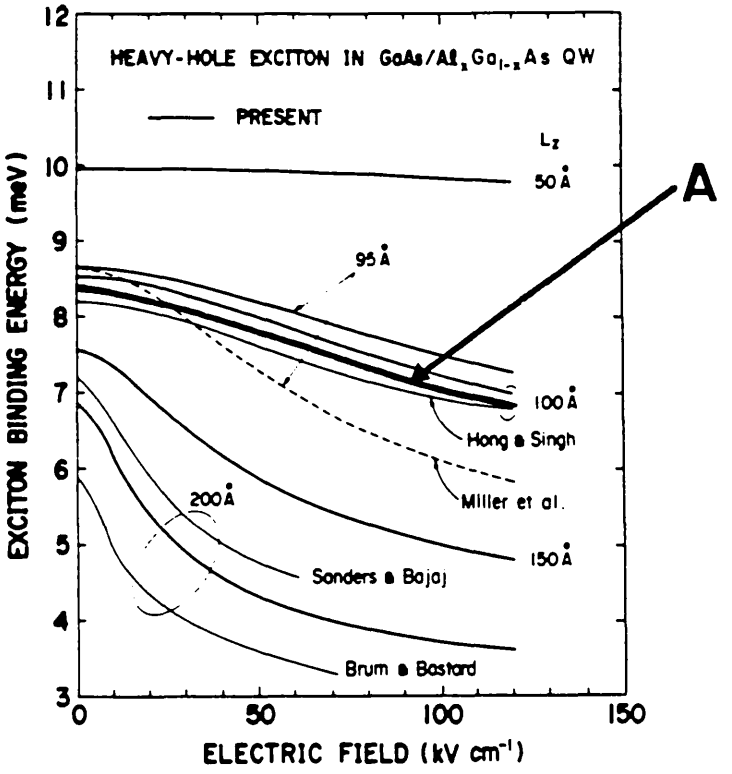


Figure 2.1 A comparison of the variation of binding energy with electric field calculated using some of the techniques described in the text. Taken from S. Nojima [2.11]. The comparision demonstrates close agreement between the different computational methods of calculating exciton envelope functions in quantum wells as a function of electric field. Curve A is the binding energy variation for a 100Å well calculated using using the method adopted in this work, showing good agreement with other methods.

results are more closely related to the electron-hole separation and the spatial extent of the envelope function Φ_{ex}, from which the 2D exciton oscillator strength is calculated. The above comparison, which demonstrates close agreement between the different theoretical results, suggests that the choice of a particular method is not critical in these calculations and that the resonant tunnelling method is as appropriate as any other approach. In particular, the agreement with the calculations of ref. [2.8] which includes valence band mixing is significant since the resonant tunnelling method neglects such effects. Equally, it will not be possible to determine the relative validity of different theoretical approaches. However, it will be possible to test the validity of those aspects that are common to all the theories. In fact, these aspects are the most fundamental. They are: the separability of the exciton wavefunction into free carrier and binding terms, the use of a single 1s separable wavefunction to describe the binding term φ_{eh} and the quantitative variation of exciton binding energy and exciton radius with applied field.

The purpose of this section has been to compare the theoretical methods that have been used to describe the problem of the exciton wavefunction in a quantum well under perpendicular electric field. Three principle conclusions have been drawn. Firstly, that an increase in the radiative lifetime of the exciton is expected due to spatial separation of the electron and hole both in the direction of

the field and in the plane of the well. Secondly, that given the common assumption of a 1s-like separable form for the exciton wavefunction, there is close agreement between different theoretical studies of the binding energy variation in an electric field, from which close agreement between results for the lifetime variation may be inferred. Finally, that in particular, the resonant tunnelling and numerical integration approaches which have been adopted here are in agreement with other methods.

2.4 The Variation in exciton radiative recombination lifetime as a function of temperature.

In this section, the variation of the excitonic radiative lifetime in quantum well structures with temperature is discussed. In the data presented in this work, a significant increase in radiative lifetime was observed as the temperature was increased. Recently, Feldmann et al. [2.12] have reported similar measurements in multiple quantum wells of various widths and presented a theory to explain this behavior. They attribute the increase in τ with temperature to a variation in the homogeneous component of the exciton linewidth.

Conservation of K vector in optical transitions (where K is the wave vector describing the exciton centre of mass motion in the plane of the wells) suggests that for

momentum conservation only excitons at K=0 may recombine (that is, annihilate) radiatively since the wave vector of the emitted photon may be assumed negligibly small. However, there exists in practice a finite spectral width (and hence finite range of K) over which recombination of any exciton may occur: the homogeneous linewidth of the transition, Γ. This finite range becomes allowed because the exciton wavefunction is never coherent for infinite time and so the K-vector and energy of the exciton may never be perfectly defined. The finite radiative lifetime of an excited state places a fundamental upper limit on the coherence time of the excited state wavefunction and a lower limit on Γ: $\Gamma \approx h/\tau$. In real solids this contribution is usually exceeded by temperature dependent scattering processes, eg. from phonons or impurities, which also destroy the coherence of the wavefunction but occur with an average time between scattering events, τ_{SC}, which is much less than τ. In this case: $\Gamma \approx h/\tau_{SC}$. The oscillator strength for perfectly coherent excitons becomes shared equally between all states within Γ, and so the effective oscillator strength available to any exciton, which is only coherent between scattering events, reduces as Γ increases. For an exciton in the ideal 2D limit, an effective 2D oscillator strength per unit cell can be defined [2.12]:

$$f_{eff}^{2D} = f_o \frac{4\pi\hbar^2}{A_X M} \frac{1}{\Gamma(T)} \qquad \text{eqn. (2.14)}$$

where: f_o is the bulk oscillator strength for interband transitions.

M is the sum of the in-plane electron and hole masses.

A_X is the exciton area

For clarity only the centre of mass motion has been considered and zero electric field assumed so that $\langle\varphi_e|\varphi_h\rangle=1$. $\varphi_{eh}(r_{eh})$ has been assumed to be 1s-like and so $|\varphi_{eh}(0)|^2$ correctly normalised becomes $2/A_X$.

However, at finite temperature momentum conservation does require that only the fraction of excitons, r(T), that lie within the homogeneous linewidth may recombine. For Maxwell-Boltzmann statistics, which govern excitons (strictly bosons) under all practical conditions:

$$r(T)=1-\exp(-\Gamma(T)/kT) \qquad \text{eqn. (2.15)}$$

So eqn. (2.14) becomes:

$$F_{eff}= f_o \frac{4\pi\hbar^2}{A_X M} \frac{r(T)}{\Gamma(T)} \qquad \text{eqn. (2.16)}$$

The absolute lifetime of the 2D exciton is related to the oscillator strength for the optical transition by [1.11][2.12]:

$$\tau_{2D}= \frac{2\pi\varepsilon_o m_o c^3}{ne^2w^2F_{eff}} \qquad \text{eqn. (2.17)}$$

where n is the refractive index and w is the photon angular frequency. So, from eqn. (2.16):

$$\tau_{2D} \alpha \frac{1}{A_x M} \frac{r(T)}{\Gamma(T)} \qquad \text{eqn. (2.18)}$$

Two regimes may be identified in eqn. (2.18) (see fig. 2.2). When $\Gamma(T)>>kT$, the exciton population lies wholly within the homogeneous linewidth and τ is determined solely by the size of Γ. Using $r(T)\approx1$, eqn. (2.18) gives $\tau\alpha\Gamma(T)$. When $\Gamma(T)<<kT$, τ is determined by the fraction of excitons which have energies lying within Γ, and eqn. (2.18) becomes $\tau\alpha kT$.

How does Γ vary with temperature for excitons in quantum wells? A theoretical study by Lee et al. [2.13] has suggested that in the low temperature regime of interest here (4.2K to 80K) LA phonon scattering greatly exceeds LO phonon and piezoelectric scattering. Recent homogeneous linewidth measurements in quantum wells (made by direct measurement of the exciton phase coherence times using four wave mixing techniques) by Schultheis et al. [2.14] have shown that the linewidth varies with temperature in a 113Å well according to:

$$\Gamma(T)=\alpha+\beta T \qquad \alpha=0.5\text{meV} \quad \beta=5\mu\text{eV/K} \qquad \text{eqn. (2.19)}$$

where α is a temperature independent contribution attributed to impurity, interfacial and defect scattering; βT is a temperature dependent contribution attributed to LA phonon scattering; and that $\Gamma<<kT$ for $T>10K$. A linear variation of excitonic lifetime vs. temperature is therefore expected in the region 10K to 80K.

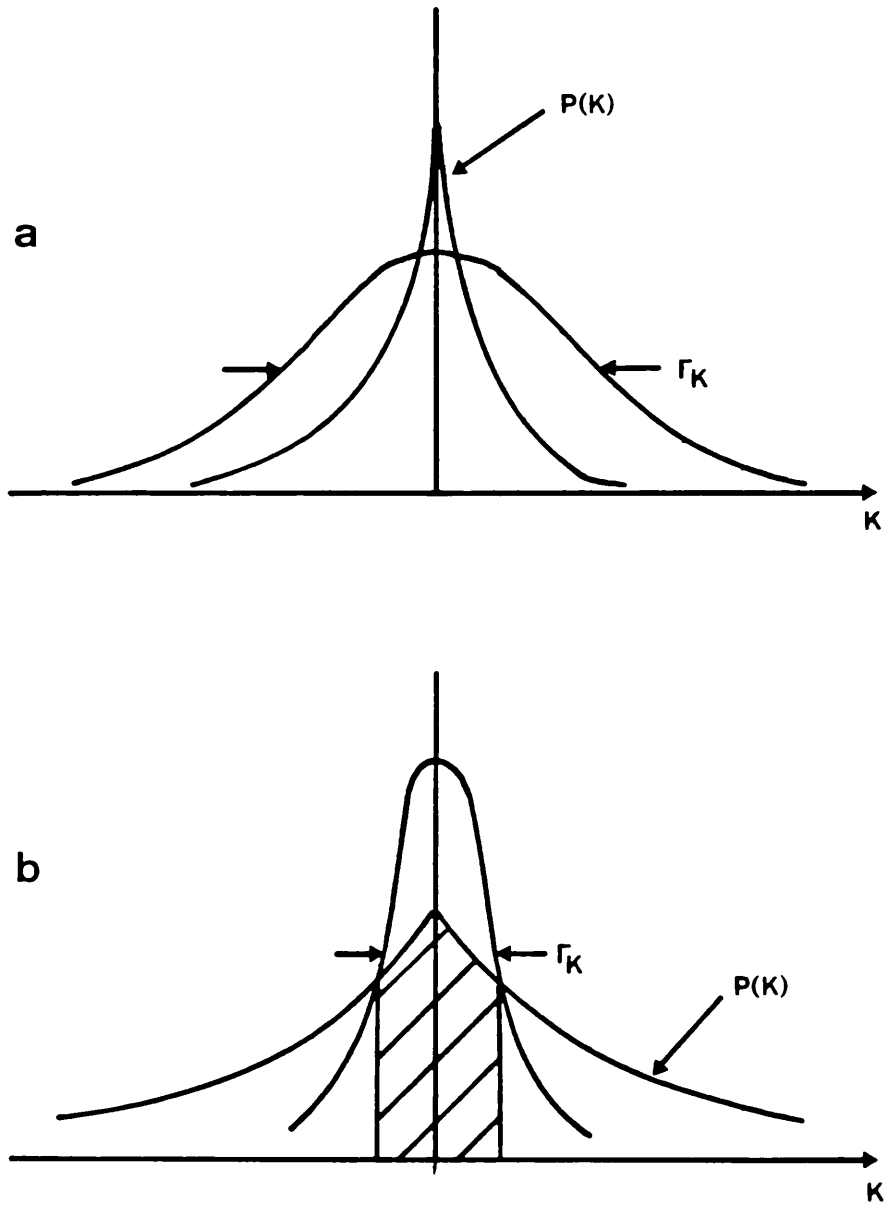


Figure 2.2 The two limiting regimes of the coherence volume argument illustrated schematically. a) If $\Gamma >> kT$, the Maxwell-Boltzmann probability distribution of exciton K values, P(K), lies almost entirely within the spread of K values, Γ_K, corresponding to the homogeneous linewidth, Γ. All excitons may recombine, with a lifetime determined by Γ, ie. the number of states over which the oscillator strength for coherent excitons becomes shared: $\tau \alpha \Gamma$. b) If $\Gamma << kT$, only the fraction of excitons with K values within Γ_K (the shaded area: equivalent to the fraction of excitons with centre of mass motion kinetic energies within Γ) may recombine irrespective of the value of Γ_K: $\tau \alpha kT$.

The argument in terms of the coherence time of the exciton wavefunction may be usefully re-expressed in terms of the area of centre of mass motion over which the exciton wavefunction is coherent before encountering a scattering event. Within eqn. (2.14), a coherence area, A_c, may be identified, given by:

$$A_c = \frac{2\pi\hbar^2}{\Gamma(T)M} \qquad \text{eqn. (2.20)}$$

So, from eqn. (2.14), becomes:

$$F_{eff} = 2f_o\, A_c/A_x \qquad \text{eqn. (2.21)}$$

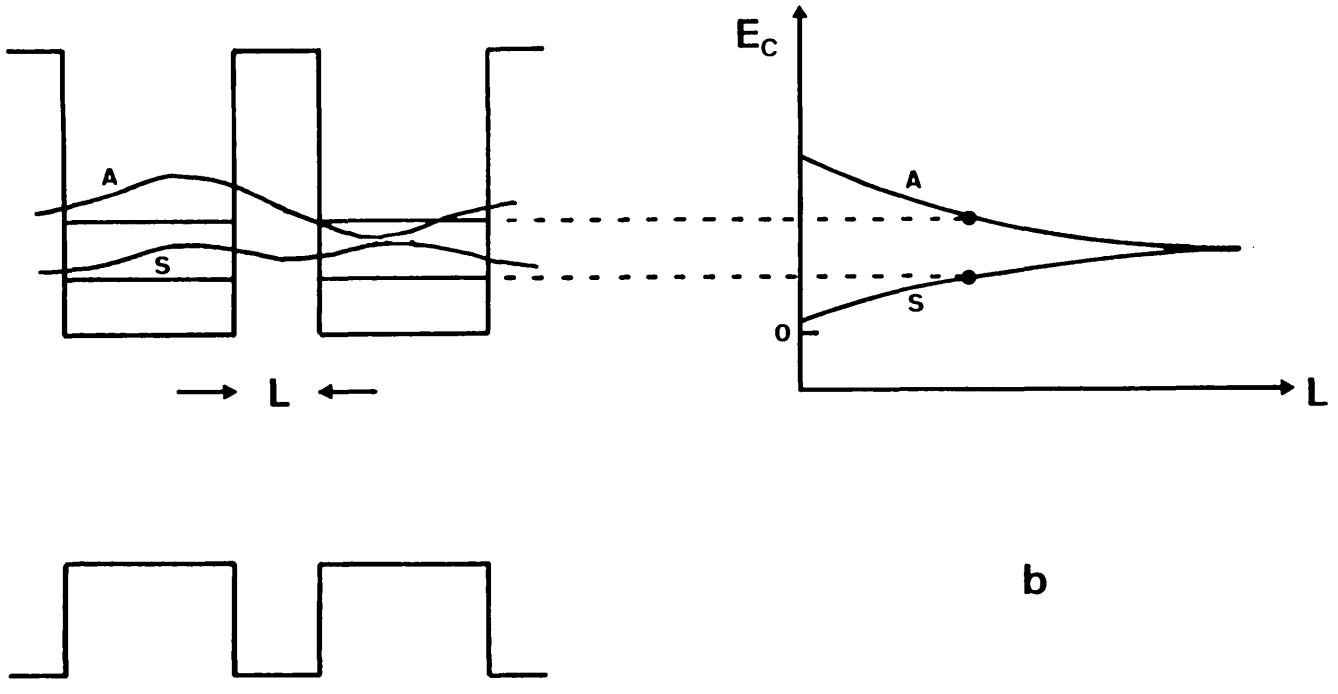
Feldmann et al. presented measurements of τ vs. T for MQWS with wells of different widths. A reasonably linear variation was obtained with similar gradients, consistent with the $\Gamma << kT$ regime, except in the case of a 25Å well structure, where a sublinear variation of the PL lifetime was observed for T<20K. This effect was tentatively attributed to localisation of the exciton wavefunction in "islands" of wider well width, introduced by monolayer fluctuations in well width as a result of the GaAs/AlGaAs interfaces within the structure not being perfectly sharp. Such islands exhibit a lower confinement energy, so that, at low temperature, excitons may become localised within these regions. Assuming the coherence area of the free exciton to be larger than the localisation island size, the island size determines the coherence area of the exciton and the radiative lifetime tends to a constant value as the exciton

population becomes localised. It should be noted however that no homogeneous linewidth measurements were made on the actual samples used in ref. [2.12].

2.5 The Properties of the Strongly Coupled Quantum Well system

In this work, the radiative lifetime measurements which have been used to investigate the exciton envelope function, have been performed on a strongly coupled double quantum well, or simply, coupled quantum well (CQW) structure. In this section, the special properties of this type of structure are discussed. The typical CQW consists of two single quantum wells separated by a narrow barrier of thickness 10Å-20Å (fig.2.3a). This structure is a particularly good example of the way that growth technology allows sample parameters to be adjusted to optimise particular properties. In this case, the presence of the thin barrier substantially enhances the electro-optic modulation depths of these structures compared to single quantum wells.

The CQW structure used in this study has been studied in CW PL and PLE by Andrews et al. [2.16] (48Å wells, 16Å barrier) and a comparable structure has been studied by Chen et al. [2.15] (75Å wells, 16Å barrier). The barriers in these structures were sufficiently thin to allow significant penetration of the single quantum well wavefunctions into



2.3 a) Real space band diagram of a coupled quantum well structure with central barrier width L. Showing the conduction band ground state confinement energies (E_C) and envelope functions of the first symmetric (S) and anti-symmetric (A) states. As L is reduced, the symmetric-antisymmetric splitting of the confinement energies increases. Application of a perpendicular electric field is analogous to reducing L, and the S-A splitting again increases as the wells become more strongly coupled. This splitting must be added to the usual Stark shift in the subband energies, enhancing the Stark shift for symmetric states and tending to cancel the Stark shift for anti-symmetric states.

the adjacent well. The degenerate isolated well states hybridise to form single particle states for the double well structure. The behavior is closely analogous to that found in the familiar hydrogen molecule problem. The isolated well wavefunctions combine to form symmetric and anti-symmetric pairs of double well wavefunctions which are split in energy, the symmetric state moving to lower energy than the isolated well state and the anti-symmetric state moving to higher energy. As the thickness of the central barrier is reduced, the symmetric-antisymmetric splitting increases (see fig. 2.3b). The application of a perpendicular electric field is analogous to reducing the central barrier width. The coupling between the wells increases as the confinement effect of the dividing barrier is reduced, and an increase in the symmetric-antisymmetric splitting again occurs. This increased symmetry splitting must be added to the usual Stark shift in the subband energies in the structure. In the case of the ground state of the system, which is the exciton of the n=1 symmetric subband, an enhanced Stark shift is consequently observed compared to a single quantum well of the same width. Andrews et al. have shown by PLE measurements that the behavior of all the confined states of the system is in agreement with this explanation. More particularly, it is demonstrated that the Stark shifts which are observed may be successfully modelled numerically by the resonant tunnelling method.

CHAPTER 3 DESCRIPTION OF THE MODE-LOCKED DYE LASER AND STREAK CAMERA SYSTEM USED FOR TRPL STUDIES AND DESCRIPTION AND EVALUATION OF A NOVEL PHOTOMULTIPLIER BASED STREAK CAMERA READOUT SYSTEM [3.1]

3.1 Introduction

There are two fundamental equipment requirements for TRPL measurements: a pulsed optical source with a pulse width less than the luminescence decay time; and a detector with a temporal resolution less than the luminescence decay time, and with sufficient sensitivity to detect the luminescence signal. Mode-locked dye laser systems [3.2] permit the routine generation of ultra-short optical pulses in the visible region, typically of ≈1ps duration; much less than may be achieved by pulsed gain or Q-switched laser systems. Picosecond sources are frequently required in TRPL studies of semiconductors where radiative lifetimes as short as a few hundred picoseconds are commonly encountered. Such lifetimes are beyond the temporal resolution of conventional optical detectors such as photomultipliers and photodiodes (typically 1ns). Alternatively, electro-optic Streak Camera systems [3.3] operating in synchroscan mode permit the detection and temporal dispersion of optical signals with a resolution of ≈25ps. Even greater resolution may be achieved in "single shot" mode (≈1-3ps) although the very large reduction in signal makes this mode only usually applicable to laser pulse diagnostic applications.

In this chapter, the mode-locked dye laser system and streak camera system which has been used in the course of this work is described and its performance evaluated. This aspect forms a significant section of this thesis because the mode-locked laser system was adapted from a commercial CW system "in-house" and a novel streak camera read-out system was designed and constructed. The readout system was designed to provide the high sensitivity and wide dynamic range required in TRPL applications where measurement of the luminescence decay profiles over several orders of magnitude is required in order to accurately determine the radiative lifetime and to distinguish between different types of recombination dynamics (see section 2.2).

3.2 The Mode-locked Dye Laser System

The principles of the operation of dye lasers have been reviewed by several authors [3.4][3.5], and the principles of mode-locking have been described by Yariv [3.5] and the references therein. In brief, dye lasers exploit the large population inversions that may be achieved within the excited states of certain large organic dye molecules in solution. Gain is supplied by optical pumping from another laser, usually an ion laser or frequency doubled Nd-YAG laser. The many vibrational and rotational modes of the dye molecules broaden the excited states and permit the laser wavelength to be continuously varied over a broad spectral range, typically ≈100nm. The use of different dyes allows

dye laser operation from around 350nm to 1200nm.

Where significant wavelength tunability is required, mode-locking in dye lasers is in general accomplished actively by synchronous pumping of the dye laser cavity with a pump laser which is itself mode-locked. Passive mode-locking by means of saturable absorber, while often simpler in implementation, in general restricts pulsed operation to a narrow spectral range. In synchronous pumping, the round trip time of the dye laser cavity is matched to the pump pulse separation time and a dye laser pulse excited by a given pump pulse receives maximum gain at the dye jet after one cavity round trip, thereby maintaining pulsed operation within the dye laser cavity. Furthermore, gain saturation within the dye jet causes compression of the dye laser pulse with respect to the pump pulse. For a typical pump pulse duration of ≈100ps, pulse compression down to ≤5ps may be achieved.

In this work, a commercial Spectra-Physics 2020-05 Argon-Ion laser [3.6][3.7] and 375B jetstream dye laser using Styryl-8 dye [3.8][3.9], have been adapted for mode-locked operation at low cost in comparison to commercial systems. The system is shown schematically in figure 3.1. The mode-locking and performance of the Argon laser and of the dye laser are now described in turn.

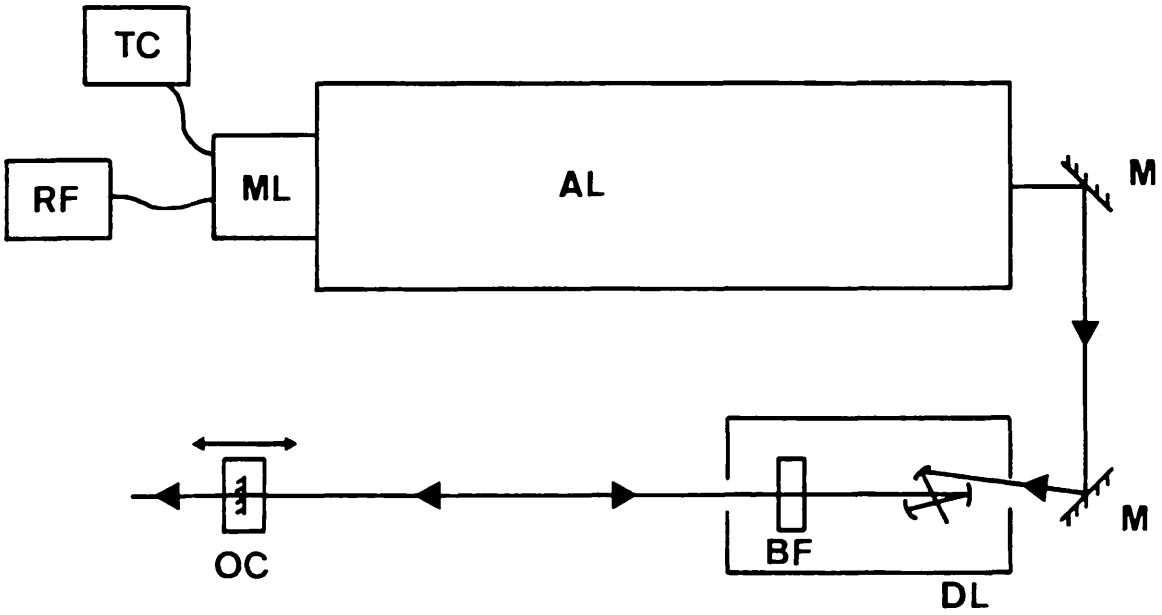


Figure 3.1 Schematic Diagram of the modelocked Argon Ion/Dye Laser system. ML modelocker assembly (fig. 3.2). RF RF source and power amp. TC modelocker temperature controller. AL 2020 Argon laser. M high reflectivity plane mirrors (96% at 500nm). DL 375B dye laser. BF 2 plate birefringent tuning filter. OC extended cavity dye laser output coupler, mounted on a differential thread translation stage.

3.2.1 The Mode-locking of the Argon Ion Laser

As suggested by the synchronous mode-locking principle, the successful mode-locking of the Argon laser presents the main technological obstacle to mode-locking of the entire system, and the performance of the mode-locked dye laser is principally determined by the duration and stability of the pump pulses. Mode-locking of the Argon laser was achieved in this work by intra-cavity loss modulation using an acousto-optic modulator (AOM) [3.5]. Sinusoidal modulation of the cavity loss at the round trip time of the cavity (that is, at a frequency equal to the spacing of the longditudinal cavity modes) causes sum and difference frequency mixing of gain between the cavity modes which then maintain a constant phase relationship (ie. become "locked"). In this case, the inter-cavity radiation bunches up into a short pulse of minimum duration, τ_{min}, given from Fourier transform arguments by a gain bandwidth-time product, $\delta f \delta\tau_{min}$, where δf is the gain bandwidth. For gaussian pulses:

$$\delta f \, \delta\tau_{min} = 0.44$$

The mode-locking process may be expressed by summing the electric field at time , t, due to the N intracavity modes within the gain bandwidth centred at frequency f_o with mode separation Ω_m (assuming constant mode amplitude):

$$E(t)=\sum_{n=-\frac{N+1}{2}}^{n=\frac{N-1}{2}} \exp[2\pi i(f_o+n\Omega_m)t+\varphi_n] \qquad \text{eqn.(3.1)}$$

If the modes maintain a constant phase relationship by sinusoidal modulation at the round trip frequency and choosing $\varphi_n=0$, eqn. (3.1) becomes:

$$E(t)= \exp(2\pi i f_o t)\ \frac{\sin(N\pi\Omega_m t)}{\sin(\pi\Omega_m t)} \qquad \text{eqn.(3.2)}$$

E(t) is then a sinusoidal carrier wave at the centre mode frequency modulated by an amplitude function corresponding to a series of pulses of width $1/N\Omega_m$ separated by $1/\Omega_m$, the cavity round trip time. Successful mode-locked operation requires precise frequency matching between the modulation frequency and the longditudinal cavity mode spacing which is determined by the cavity length.

Acousto-optic modulators function by means of an acoustic standing wave which is generated in a block of glass by a piezo-electric Lithium Niobate ($LiNbO_3$) transducer bonded onto the side of the block. Acoustic standing wave resonances are set up in the glass whenever the length of the block is equal to an integer number of half acoustic wavelengths. On a resonance, the amplitude of the acoustic standing wave modulates the refractive index of the glass (the acousto-optic effect) at a frequency equal to twice the

acoustic wave frequency, creating a diffraction grating whose amplitude (and hence diffraction efficiency) varies sinusoidally at twice the driving frequency. Placed within the laser cavity, the power diverted into the diffracted orders by the AOM may be used to modulate the intracavity loss.

In this work, a Spectra Physics single-line end mirror assembly was adapted for use as a mode-locker assembly in the 2020 laser. The assembly is shown schematically in figure 3.2. Single line operation, which is preferable for optimum mode-locked performance, is established by means of a Brewster angle prism tuning element (P in fig. 1.2). In this instance, the prism was adapted to form the AOM. The modulator was constructed by bonding a $LiNbO_3$ transducer (L) onto the side of the prism by means of an Indium cold weld. The transducer was chosen to have a third harmonic resonant frequency in the 60MHz region, ie. the modulation frequency required for mode-locking in the 2020 cavity (length ≈1.20m). The bonding was performed by Gooch and Housego Ltd., who also evaporated gold front and back contacts on the transducer. With the exception of the area directly opposite the transducer, the opposite surface of the prism was bead blasted to create a roughened surface to destroy any coherent internal reflection of the acoustic waves from the sides of the prism except from the area directly opposite the transducer. The area of the front contact was 6mm, chosen to match the impedence of the transducer to 50Ω at 60MHz. 50Ω miniature coax (RG174) was contacted to the

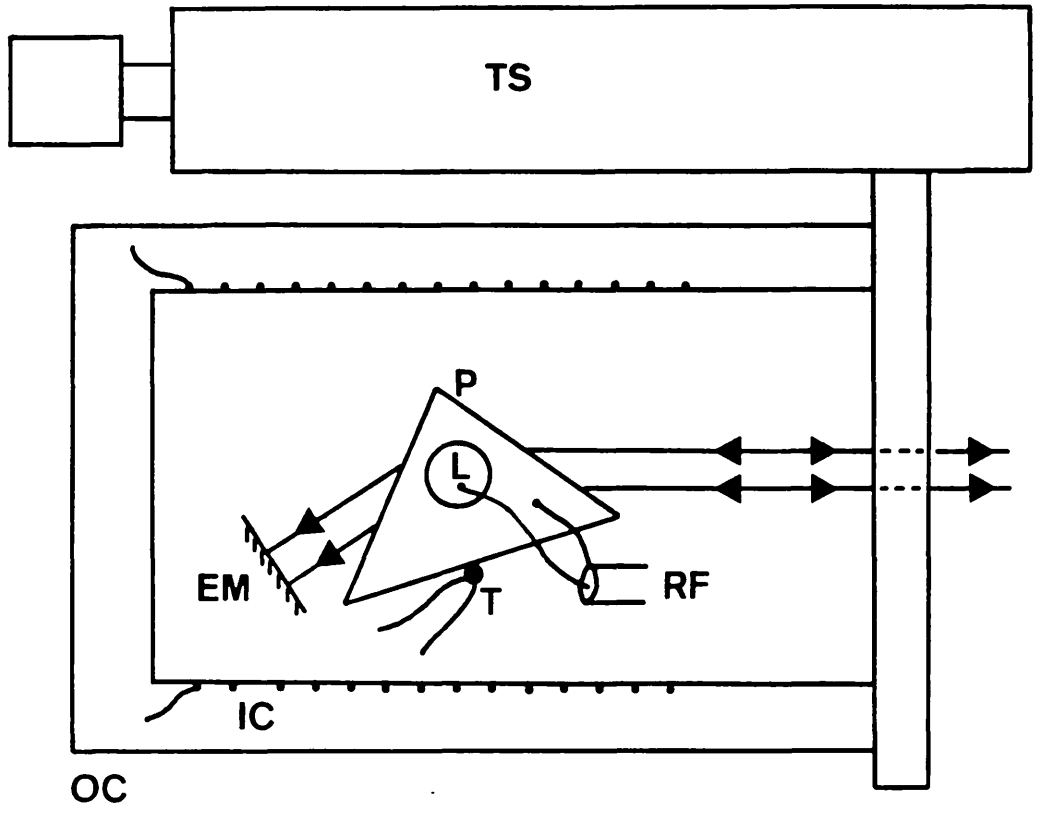


Figure 3.2 Schematic diagram of modelocker assembly indicating the path of the intra-cavity radiation. TS differential thread translation stage for cavity length adjustment. P brewster angle quartz prism. L $LiNbO_3$ transducer. EM 100% reflecting cavity end mirror. RF coaxial cable supplying RF drive to modelocker. T thermistor, heat sunk to bottom of prism. IC cylindrical inner cover with wire wound heater. OC cylindrical outer protective cover.

transducer using Demetron silver loaded paint. Good thermal stability was required within the assembly because the frequencies of the standing wave resonances of the prism are a strong function of temperature. The temperature of the modulator was maintained at 45°C by means of a wire-wound heater mounted around the inner cylindrical cover enclosing the modulator assembly (IC in figure 3.2). The modulator temperature was measured by a thermistor (T) mounted underneath the prism (P) and thermally anchored to it using heat sink compound, and the heater power (connections not shown) was controlled by a PID temperature controller (CRL 205). The operating temperature of the assembly was chosen so that the power supplied by the heater was much greater than any change in heat input due to changes in the RF power supplied to the modulator. During usual operating conditions the temperature could be held constant to within ±0.1°C. A differential screw translation stage with up to 13mm travel (TS) was incorporated into the assembly so that the effective cavity length of the Argon laser could be matched accurately to the modulation frequency of the AOM when the latter was on resonance.

When the $LiNbO_3$ transducer was bonded to the prism, the large Q value resonance of the transducer ($Q \approx 10^6$) became damped by the large mass of the glass. Diffracted orders could be generated by the modulator at a series of frequencies separated by 375KHz, each satisfying the standing wave condition in the prism, within an envelope of 8MHz centred on 59MHz, corresponding to an effective Q-value

of ≈7 for the transducer/prism combination. An RF frequency synthesizer (Racal 9081) was used to select a resonance in the 60MHz region with good diffraction efficiency. At the selected frequency, 62.615MHz, a single pass diffraction efficiency of 20% could be observed under standard operating conditions of 1W input power with a standing wave ratio (SWR) of 2 as measured using a Zetargi 203 SWR meter, and at least 6 diffracted orders were easily visible each side of the zeroth order beam. Trials with unsuccessfully bonded transducers indicated that this number of orders must be generated by a modulator if the required modulation depth for good modelocking is to be achieved.

The mode-locker assembly was driven intracavity under the above drive conditions and the endplate adjusted to select the 514nm argon line. The cavity length was then adjusted until pulsed operation was observed using a fast photodiode (BPW28) and sampling oscilloscope (Tektronix 3S2/3T2/S4). Optimisation of the mode-locking was greatly facilitated by measuring the pulse width using the streak camera system. Best pulse widths were achieved by replacing the usual 2020 output coupler (G3876-006) with 4% transmission by a 488nm and 514nm line only mirror with 12½% transmission (G3814-016), as expected from mode-locking theory. Using this output coupler, pulse widths of 85ps at 400mW output power were measured using the streak camera (fig. 3.3), comparable in duration to those achieved in commercially available systems. To eliminate the phase

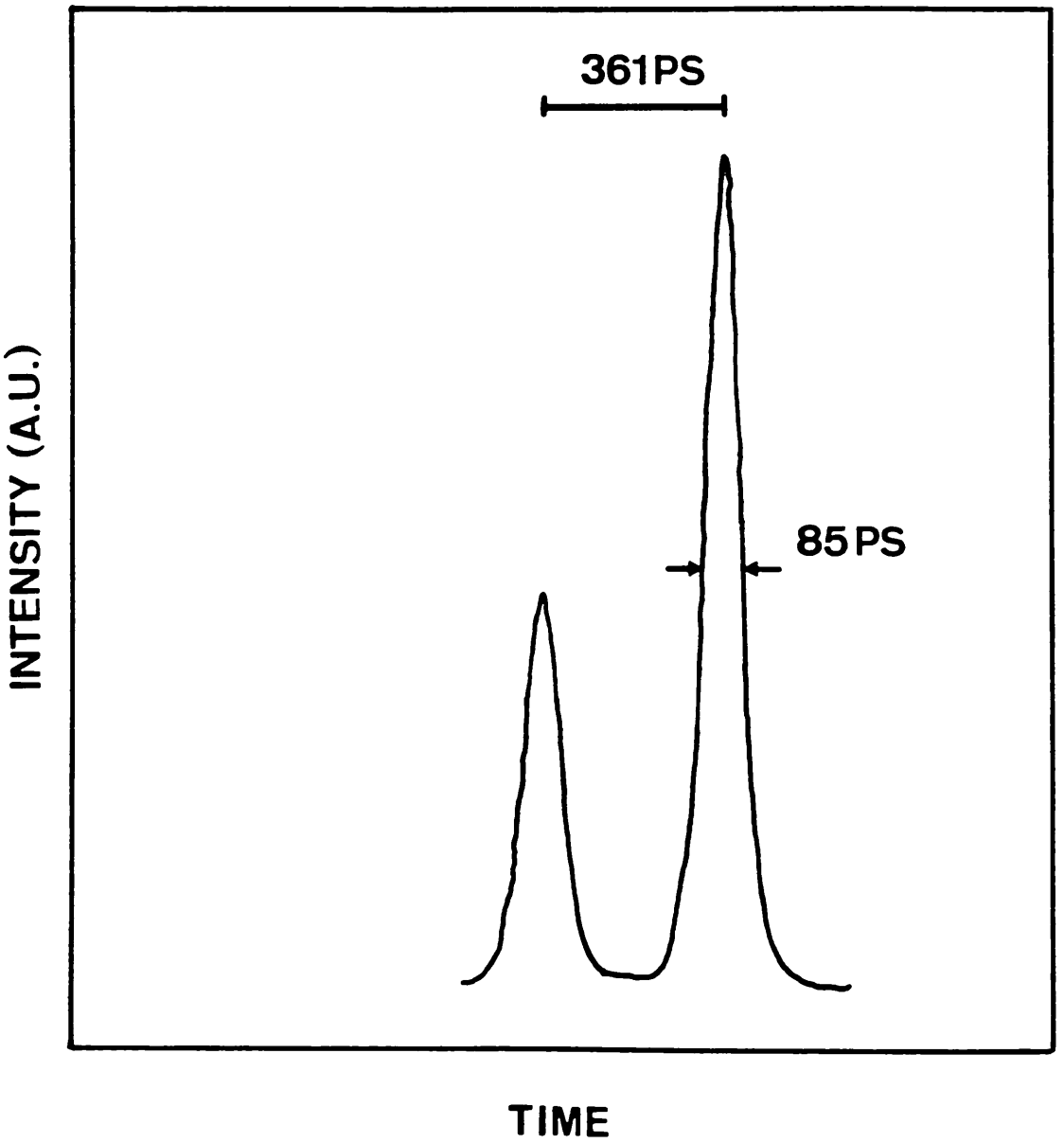


Figure 3.3 Optimised Argon Laser pulses of 85ps FWHM, as measured by the streak camera.

noise associated with RF frequency synthesizers, the synthesizer was subsequently replaced by a home built temperature stabilised fixed frequency quartz crystal oscillator using a Butler emitter follower RF oscillator circuit [3.10] and a commercial 62.615MHz 3rd harmonic crystal maintained at 50°C.

3.2.2 The mode-locked 375B Styryl-8 dye laser

Styryl-8 dye [3.8] was used for these studies, producing tunable radiation in the 720nm to 830nm region, allowing optical pumping of quantum well structures at low temperatures at photon energies either resonant with or above the n=1 heavy hole exciton line. A water cooled dye chiller operating at 10°C was constructed to prolong dye lifetime. The dye laser cavity was extended to match the argon laser cavity by replacing the 375B output coupler with an externally mounted assembly incorporating a differential micrometer translation stage with up to 5cm travel. In this way, the precise matching of the cavity lengths (to within 10μm) which is required for optimised mode-locked performance could be achieved. For wavelengths less than 780nm a specially commissioned output coupler with 10% transmission between 700nm and 800nm was used. Above 780nm the Spectra Physics Styryl-9 output coupler (G0230-009) was used. Styryl-9 high reflectors (G3845-011) were used in both cases. An intracavity birefringent filter with a bandwidth of 0.8 meV and a free spectral range of 80nm was used to tune the laser wavelength. The use of different output

couplers allowed the maximum tuning range of the dye to exceed the free spectral range of the filter.

Using a typical mean pump power of 400mW, laser action was observed in the dye laser over a 5mm range of cavity length and pulsed operation over a range of 2mm. Figure 3.4 shows the optimised laser pulses as detected by the streak camera. The measured pulse width of 25ps corresponded to a deconvolved dye laser pulse width of 18ps, obtained by deconvolving the static spatial resolution of the streak tube: 17ps at 10 Watts RF power. Such pulse widths are typical of synchroscan streak camera systems, the resolution being determined by RF phase jitter between the streak camera and the mode-locker. The single pulse duration was determined using a home built real time scanning second harmonic autocorrelator [3.2] (fig. 3.5). An autocorrelation width of 2.7ps FWHM was obtained under optimised conditions (fig. 3.6) with the expected 3:1 ratio, implying a FWHM pulse width of 1.92ps assuming gaussian pulses, close to the Fourier transform limit of 1.87ps for a 0.42nm spectral bandwidth.

3.3 The Electron-optical Streak Camera system

3.3.1 Principles of Operation and the Generation of the streak image in the current system.

In streak cameras, the transient optical signal to be detected is incident upon a photocathode at the input of the

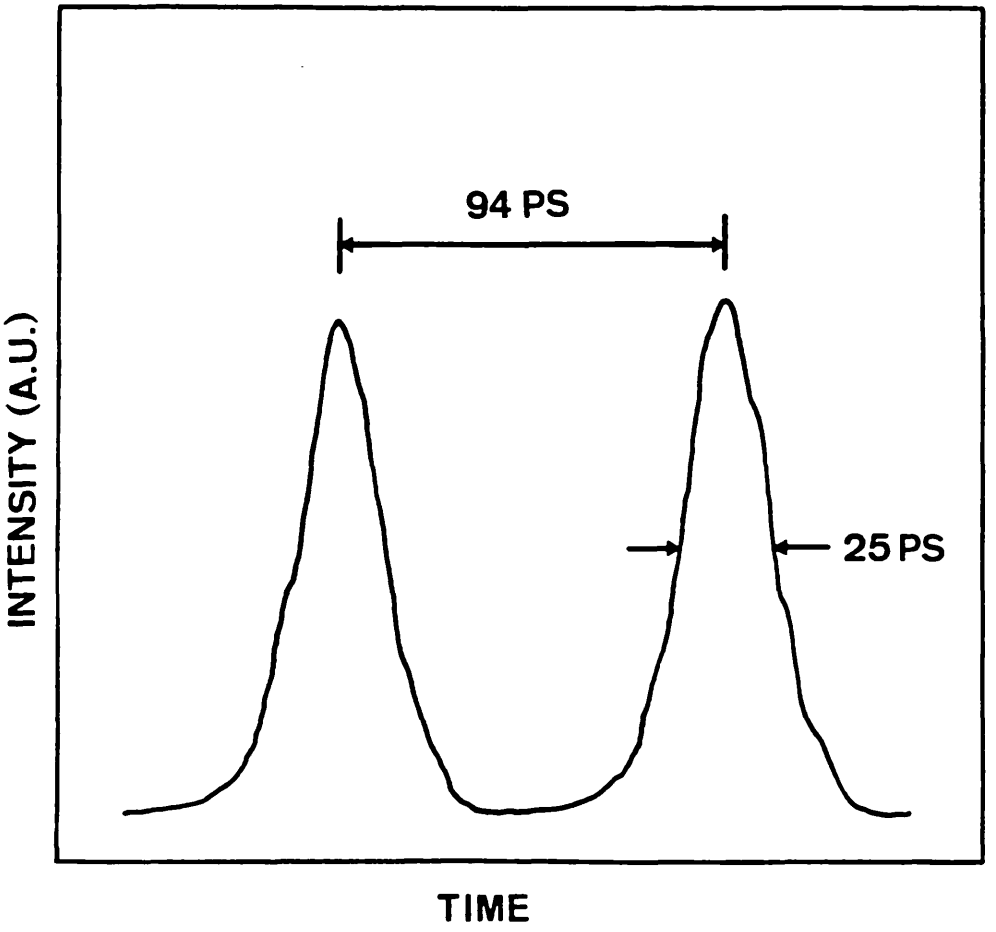


Figure 3.4 Optimised Styryl-8 Dye Laser pulses of 25ps FWHM as measured by the streak camera.

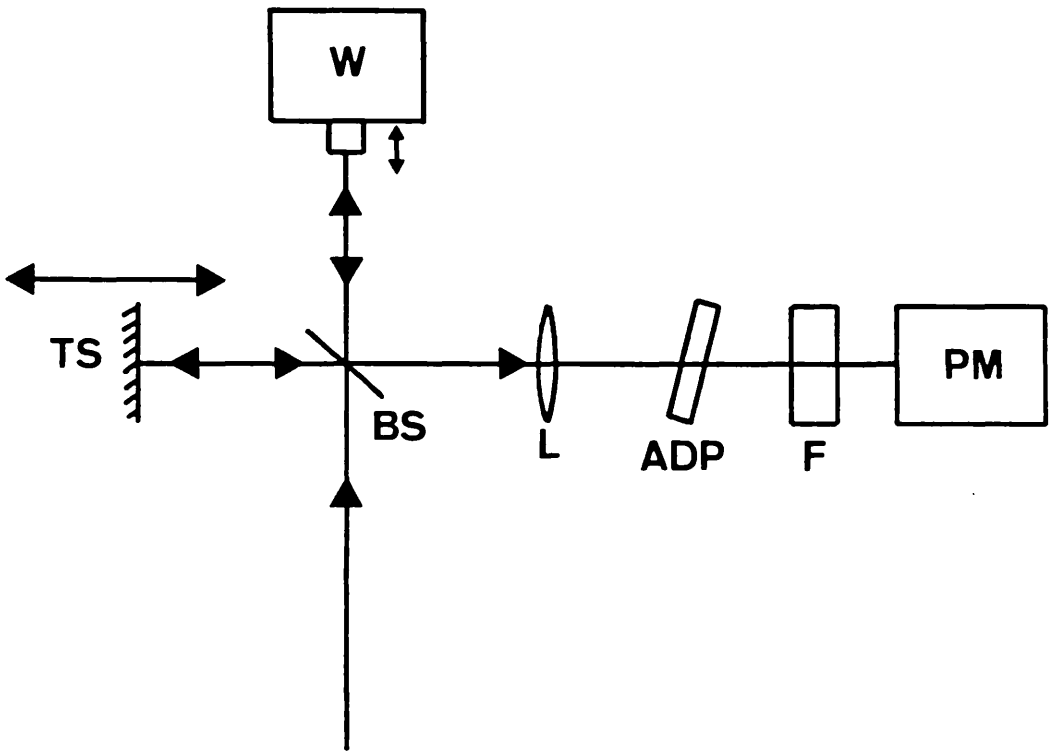


Figure 3.5 Schematic Diagram of the Second Harmonic Auto-correlator. BS 50:50 dielectric beamsplitter. TS mirror mounted on translation stage for slow scanning. W Bruel and Kjaer minishaker for real time autocorrelation measurements. L focussing lens D=15mm f=12cm. ADP ADP second harmonic generation crystal, orientated for correct phase matching. F four 3mm thicknesses of BG23 filter to remove radiation at the fundamental wavelength. PM photomultiplier tube.

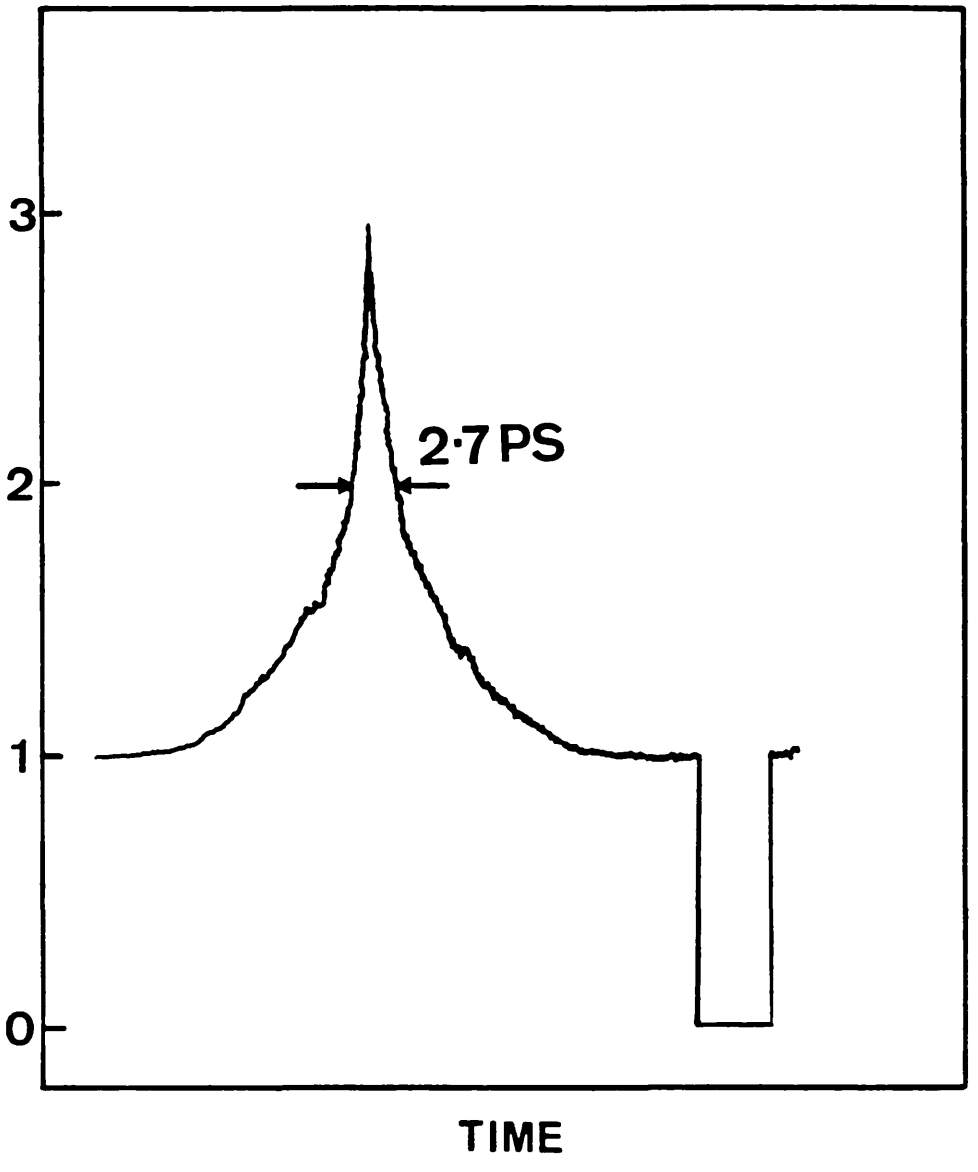


Figure 3.6 Second Harmonic Autocorrelation trace of the optimised dye laser pulses. The FWHM of the autocorrelation peak, 2.7ps, is equivalent to a FWHM pulse width of 1.92ps, assuming gaussian pulses.

vacuum streak input and converted into a pulse of photoelectrons with the same temporal profile as the input signal. The photoelectrons are imaged onto a phosphor screen at the streak tube output by appropriate electron optics. A sinusoidal HT RF sweep voltage is applied to deflection plates within the streak tube and sweeps the image across the phosphor creating a spatial distribution of phosphor emission intensity which is proportional to the temporal distribution of the incident photoelectrons and hence of the optical input signal. When used with synchronously modelocked laser systems, the deflection circuitry and the mode-locker may be driven from the same RF source. In this case, the streak camera sweep rate is matched to the pulse repetition rate and the signal due to successive pulses is superimposed allowing many pulses to be integrated: the so-called synchroscan mode.

In this work, a basic streak tube with an S1 photocathode and a P11 phosphor, but with a DC HT supply and electron imaging optics only, was supplied by Delli-Delti Ltd. The sensitivity of the S1 photocathode was determined using a fourier transform interferometer and usable sensitivity was observed for wavelengths up to 1μm (fig. 3.7). Standard high Q RF LC series resonance circuitry (fig. 3.8) was added to the deflection plates of the streak tube and tuned to resonate at the mode-locker drive frequency using a variable capacitor (VC in fig. 3.8). The RF drive was derived from the modelocker oscillator and coupled inductively (RF) into the LC circuit. On resonance a large RF voltage was

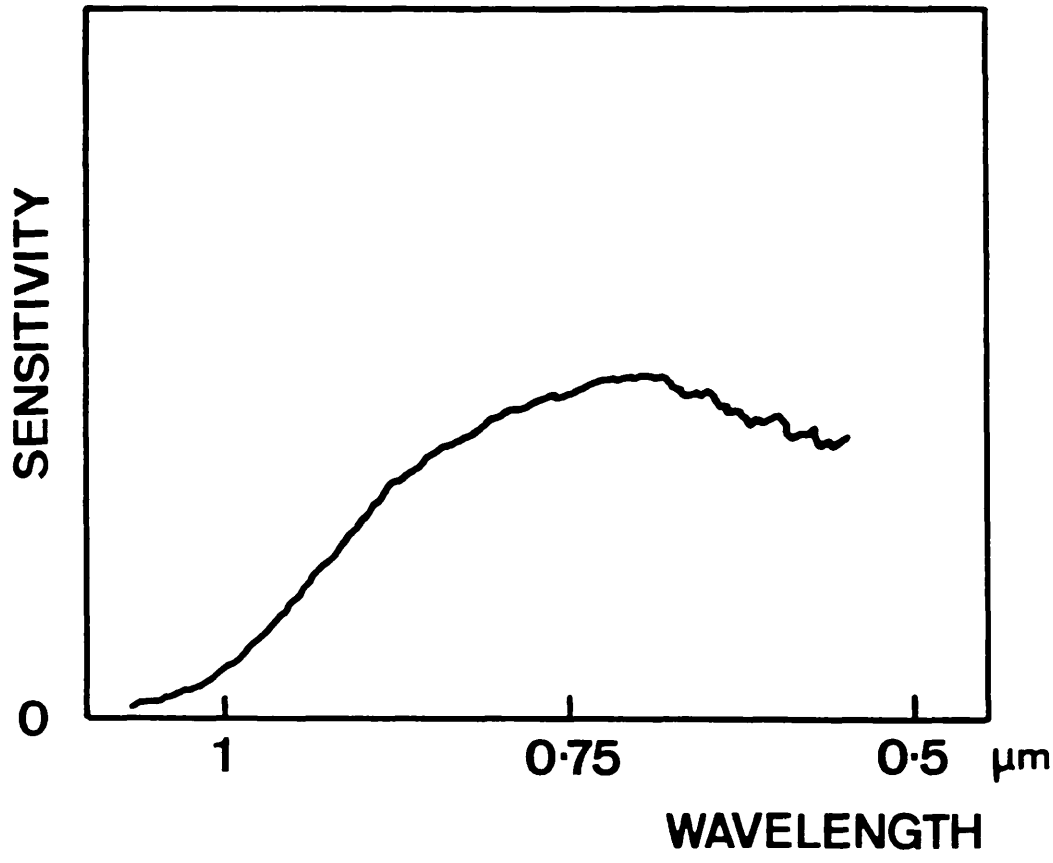


Figure 3.7 Spectral sensitivity (arbitary units) of the streak camera photocathode, as measured using a Fourier Transform Interferometer. The curve has been ratioed to compensate for the spectral profile of the interferometer source.

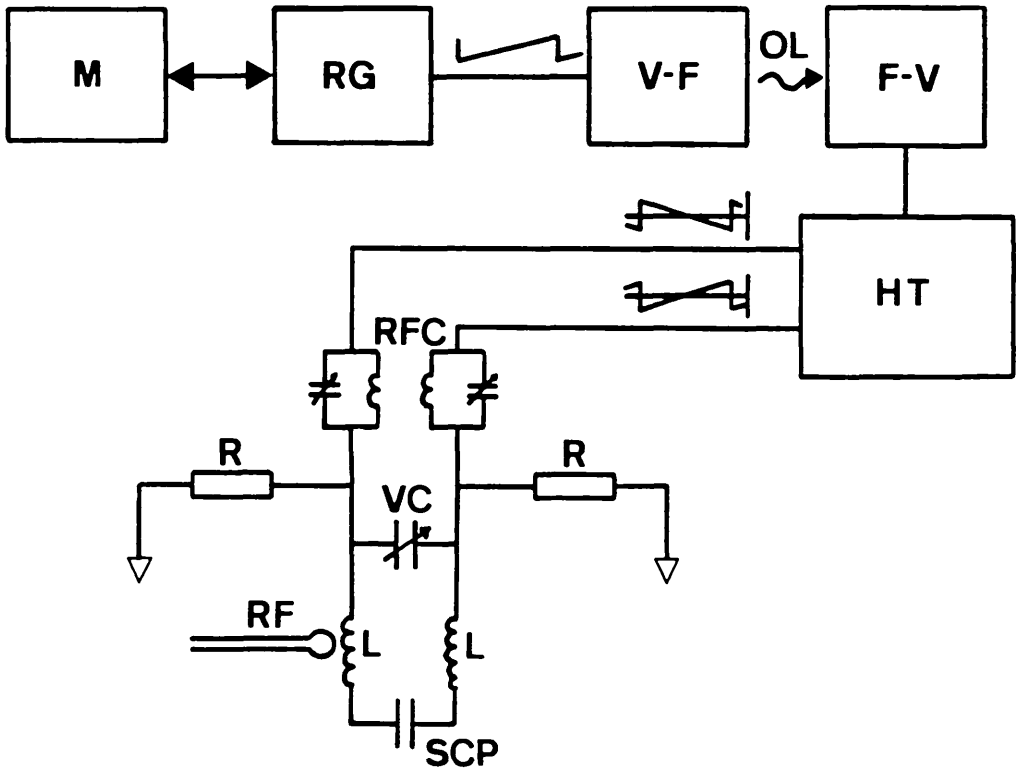


Figure 3.8 Schematic Diagram of the Streak Camera deflection circuitry and LF ramp circuit. M microcomputer. RG low voltage ramp generator unit. V-F voltage-to-frequency converter. OL opto-isolator link. F-V frequency-to-voltage converter. HT high voltage ramp circuitry. RFC high Q parallel resonance RF chokes. R 1MΩ bleed resistors. VC variable capacitor for tuning streak camera resonance ciruit. L wire-wound inductors. SCP streak camera deflection plates. RF inductive loop for coupling RF drive to streak camera.

generated across the streak camera deflection plates (SCP). In this configuration, two symmetric streak images written in opposite directions are generated per RF sweep period. A diode-doubler amplifier to drive the streak camera at twice the modelocker drive frequency generating only one output image per sweep was omitted in this case to allow slower luminescence decays (up to 4ns) to be measured without significant streak wrap-around effects. Better time resolution was obtained when the deflection circuitry was driven by a suitable proportion of the output of the modelocker drive amplifier (0-15W) rather than using a separate amplifier connected to the RF oscillator source. A set of switchable coax cables of variable length were used to adjust the relative phase of the input signal and the RF sweep voltage in order to position the streak images at the centre of the RF sweep.

3.3.2 The Streak Camera Read-out System

Streak cameras used in TRPL applications require an optical read-out system with 1D spatial resolution in order to record the spatial profile of the streak image at the phosphor. Typical commercially available image analysis systems such as CCD arrays, silicon diode arrays and SIT vidicon optical multi-channel analysers, function in parallel by detecting the luminous intensity in each spatial element simultaneously. These systems use the output signal generated at the phosphor efficiently since all generated photons are available for detection at all times. However,

such systems are often characterised by low signal gain, large dark currents, small dynamic range and high cost. In this work, a low cost photomultiplier tube (PMT) based streak camera readout system has been developed. Here, a low frequency HT sawtooth ramp voltage is added to the RF sweep voltage present on the streak tube deflection plates causing the entire streak image to be scanned across the phosphor at the ramp voltage repetition rate. In this case the streak image may be read-out "in-series" by the PMT by placing an output slit over the phosphor screen, orientated so that only signal from the same time window is detected at a given instant. The entire streak image may then be detected in sequence as it is scanned across the slit by the ramp voltage. The high gain and low noise achievable in PMT's compensates for the large percentage of the total signal which is discarded at any given time in this configuration.

Simple PMT based streak camera readout systems have previously been reported [3.11][3.12]. Bradley et al. (ref [3.11]) used a 50Hz HT transformer to generate the low frequency sweep voltage but found temporal resolution to be limited by the decay time of the phosphor. In this work, a computer controlled linear ramp generator has been designed and constructed to scan the streak image across the output slit arbitrarily slowly thereby avoiding any phosphor decay time effects. The circuit is also shown schematically in fig. 3.8. The generator produces two symmetrical positive

and negative going ramp voltages of maximum amplitude 500V pk-pk, thereby generating a total voltage swing of 1000V at the streak plates. The low voltage ramp generator circuitry (RG) was connected to the HT circuitry (HT) via a frequency converted opto-isolator link (V-F,OL,F-V) so that the HT circuitry was perfectly floating. In this way, the local earth of the ramp voltages was determined only by the 1MΩ streak camera deflection circuitry bleed resistors (R), ensuring that the deflection was symmetrical about the axis of the streak tube. In this way, the output slit could be placed on the centre of the tube axis where the spatial and hence temporal resolution of streak tube is optimised in streak tube design.

In order to minimise the reduction in the Q of the RF deflection circuit, and to prevent corruption of the ramp generator ciruitry by large RF voltages, the HT ramp generator was connected to the deflection circuit via tunable high Q LC parallel-resonance RF chokes (RFC). At resonance, these circuits present an infinite impedence to the RF signal, effectively isolating the streak camera at RF frequencies but presenting very low impedence to the low frequency ramp. The ramp voltage resulted in a maximum of 17.5 mm of total movement of the streak image: 175 times the static resolution of the streak tube. The luminous intensity passed by the streak camera output slit was imaged by an f/1 lens onto an EMI 9558 photomultiplier with an S20 photocathode cooled to 0°C using a Peltier effect cooler. The PMT output was amplified by standard op-amp circuitry

with adjustable time constants and fed into the analogue port of a microcomputer (Acorn Archimedes). For long scan times such as required in TRPL applications, the ramp generator voltage could be controlled directly from the 8-bit output port of the microcomputer (M in fig. 3.8). This facility allowed convenient co-adding of several scans, compensating for slow drift in laser output power. For rapid scanning, as required in real time laser pulsewidth measurements, the ramp generator could be driven by an internal clock at repetition rates of up to 100Hz.

Noise tests on the streak camera indicated that the dark count originating from the fraction of the room temperature streak camera S1 photocathode area which was imaged onto the output slit at any given instant was approximately twice the dark count from the cooled PMT (≈70counts/second). Some spatial variation in the dark count from the streak camera photocathode (≈5%) was observed, however this effect could be corrected by background subtraction routines within the data processing software. It should be noted that either of these noise figures could in principle be further optimised. Since the predominant phosphor emission is in the blue region of the spectrum, the S20 based PMT could be replaced by a bialkali photocathode photomultiplier with no loss of sensitivity. Dark currents down to 2 photons/sec may be achieved using cooled bialkali photocathode PMT's [3.13]. Substantially lower streak camera photocathode dark counts (and higher quantum efficiency) could be achieved where very

long wavelength sensitivity (>840nm) is not required by using an S20 photocathode streak tube or by cooling the S1 photocathode. In this case a reduction in streak camera photocathode dark count rate of a factor of 100 would be expected [3.13]. In this way it may be seen that noise limits of less than 10 counts per second per channel could be easily achieved in an S20 streak camera system. In addition, since measurements of the system efficiency have shown that each streak tube photoelectron produces ≈10 PMT counts spread over one phosphor decay time, in principle the PMT noise could be eliminated totally by means of a charge integrating discriminator circuit set to integrate over a phosphor decay time (≈0.1ms). However, since this implies rather long dead times between separate detection events, such a technique is restricted to low initial count rates. Since the S1 streak camera photocathode used in this study was itself rather noisy, early experiments with such circuits were discontinued.

The overall system was operated under two sets of typical operating conditions. For laser pulsewidth measurements such as those shown in figs. 3.3 and 3.4, the streak tube was driven by 10W of RF power with the input slit set to 70μm and the output slit matched at 100μm, allowing for a streak tube magnification of x1.3. The data was taken on a single LF scan of 20 sec with a time constant of 50 msec and the time calibration was obtained by standard delay line techniques. Since a single pulse duration of 2ps was determined using the second harmonic autocorrelator, the

measured pulsewidth of 25ps represents the resolution of the dye laser/streak camera system when operated in synchroscan mode.

For TRPL studies, the RF power to the streak camera was reduced to ≈2W and for typical signal strengths from single quantum wells, the input and output slits widths were increased to 120μm and 175μm respectively, yielding a time resolution of 50ps. Typical data shown in fig. 3.9 was taken during the coupled quantum well experiments described in chapter 4 using four coadded scans each of 102secs. duration and a time constant of 0.5s. The signal strength corresponded to a time integrated luminous flux of 7.2pW. Time calibration was obtained in this case by measuring the total RF streak amplitude and calibrating the streak in terms of one quarter of the RF period (4ns). The raw data has been processed under software control in order correct for the sinusoidal nature of the RF scanning voltage. This correction technique restricts the maximum RF power (and hence time resolution) that may be used by the requirement that at least one half of the streak image can be scanned across the output slit by the LF ramp voltage so that the RF amplitude may be determined. In fig. 3.9, both halves of the RF sweep have in fact been measured, providing two complementary measures of the PL decay time. In addition, the data has also been processed to subtract the noise background, as previously described. The software also contained the facility to ratio out fluctuations in dye

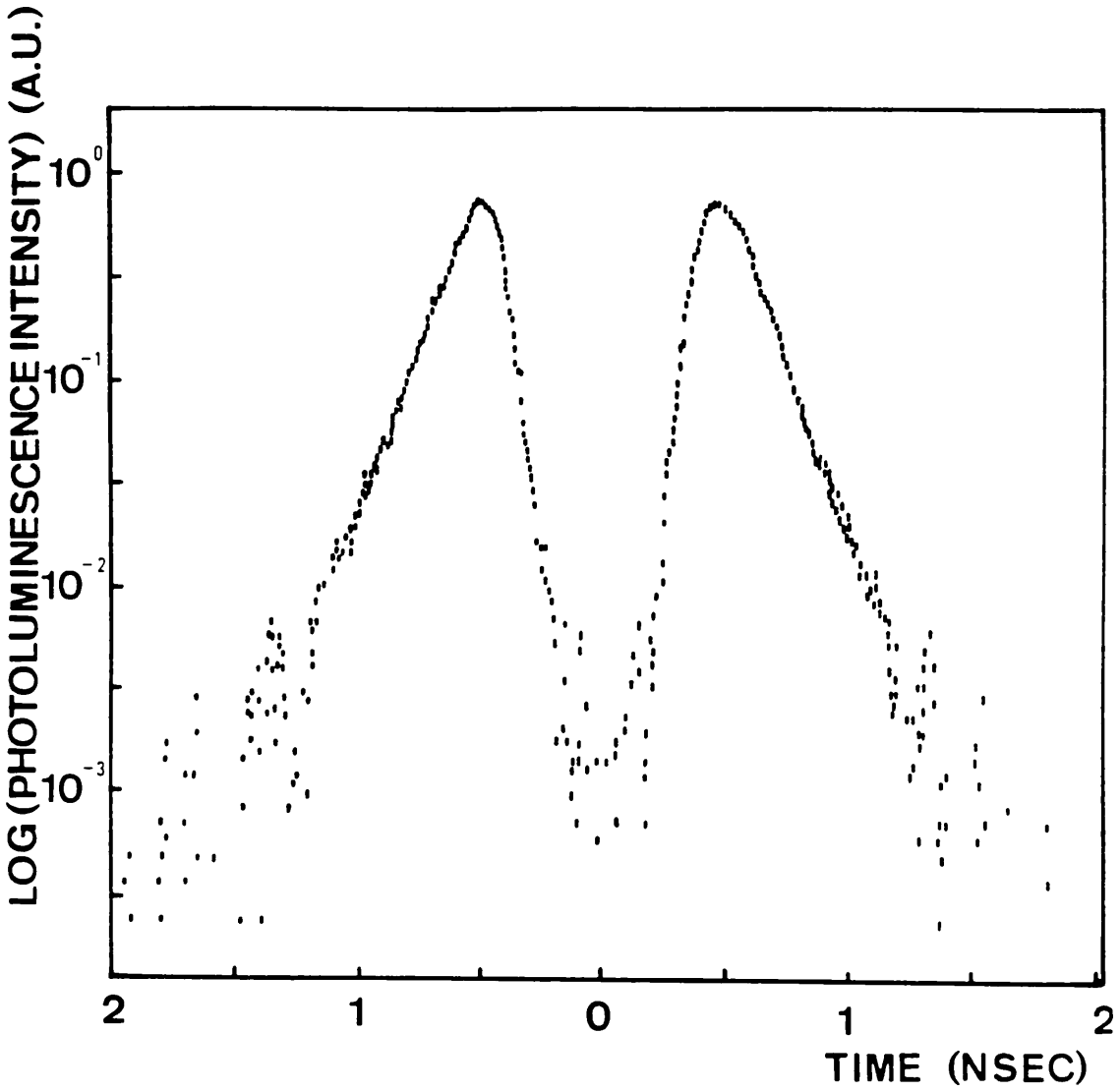


Figure 3.9 Typical TRPL data from the coupled quantum well studies described in chapter 4.

laser intensity by sampling the signal generated from a photodiode fed with a small fraction of the dye laser output on a second analogue channel and with a time constant matched to that of the PMT amplifier. In fact, due to the long time constants that were used, and the coadding technique, this facility proved to be unnecessary.

3.4 Comparison of the Serial and Parallel Read-out Configurations

For comparison with parallel detection systems, the signal-to-noise ratio (S/N) of the serial system must be derated because for a spatial resolution corresponding to C discrete channels, the single channel system integrates the phosphor intensity in each channel for a time 1/C shorter than for a multichannel system. Assuming the noise to be dominated by photon shot noise, for D photons/sec dark count and S photons/sec of detected signal, the (S/N) ratio of the multichannel system in a given channel is:

$$(S/N)_m = \sqrt{T}\,\frac{\eta_m S}{\sqrt{(\eta_m S + D_m)}} \qquad \text{eqn. (3.3)}$$

where T is the total measurement time over which the channel is integrated and η_m is the net system quantum efficiency of the multichannel system. For simplicity, zero amplification noise has been assumed in eqn. (3.3). In some multichannel systems this contribution may be significant and increase the effective shot noise associated with the $\eta_m S$ term. By contrast, PMT's exhibit negligible

amplification noise.

For the single channel system, (S/N) becomes:

$$(S/N)_S = \sqrt{(T/C)}\ \frac{\cap_S S}{\sqrt{(\cap_S S + D_S)}} \qquad \text{eqn. (3.4)}$$

Where $\cap_S$ is the quantum efficiency of the photomultplier photocathode. The relative performance, R, of the single channel and multichannel configurations may then be expressed by dividing (3.3) by (3.4):

$$R = \frac{(S/N)_S}{(S/N)_m} = \frac{1}{\sqrt{C}}\ \frac{\cap_m \sqrt{(\cap_S S + D_S)}}{\cap_S \sqrt{(\cap_m S + D_m)}} \qquad \text{eqn. (3.5)}$$

Considering first the large signal regime where the dark count may be neglected, ie. $\cap_S S > D_S$, $\cap_m S > D_m$: for the simple case of multichannel detection with $\cap_m = \cap_S$ and $D_m = D_S$, and taking C=100 typically, the signal to noise in the multichannel system exceeds that of the single channel system by a factor of 10 (ie. $\sqrt{C}$). Conversely however, for the large values of S implied by $\cap S > D$, the effect of shot noise is small and may be neglected in most applications. In practice, the quantum efficiencies and dark count rates vary between different devices. Assuming that the input optics have equal collection efficiencies throughout, if $\cap_m / \cap_S \leq 1/C$, the signal loss of the single channel configuration is completely compensated for by the greater net quantum efficiency of the photomultiplier. This is the case in photodiode array and conventional CCD systems which

typically have $\cap_m$ equal to 1/1600 and 1/400 respectively [3.14] compared to $\cap s$=0.25 for a typical S20 PMT at 400nm. More complex and expensive intensified SIT vidicon or cooled high performance CCD systems systems achieve $\cap p \approx 0.1$ and 10 dark counts/sec/pixel [3.14][3.15] so that $D_p \geq 160$ assuming coupling into at least 16 25μm pixels per channel for a streak camera spatial resolution of 100μm. In this case, (S/N) is a minimum of a factor of $\sqrt{(0.1C/0.25)}$ greater in the multichannel system in the large signal regime, although (S/N) is in any case high in this limit. This factor would rise rapidly in the small signal regime (assuming $D_S=D_p$) as the signal becomes lost amongst the noise. However, from eqn. (3.4), a large difference in dark count performance between the two systems can compensate for the signal loss in the single channel system, the minimum ratio of dark currents at which the signals become equal is $D_p/D_S \approx C\cap_S/\cap_p$ in the small signal limit, rising rapidly in the large signal regime. Therefore, in comparison to D_p=160, it may be seen that an optimised bialkali PMT system with $\cap_S$=0.25 and D_S=2 could becomes comparable or superior to the ISIT and cooled CCD systems in the small signal regime where good signal to noise is most required. Where appropriate, the signal loss in the single channel system can be further minimised by programming the ramp generator to integrate longer in regions where the signal is weak (and S/N poorest) or to skip regions where no signal is present (effectively reducing C).

The most favourable application of the single channel system has not yet been discussed. In the case of time resolved spectral studies of photoluminescence (eg. in spectral studies of carrier cooling phenomena [1.10]), a single time window is monitored and the spectrometer scanned to determine the spectral profile of the luminescence at that time. Since the ramp generator may be conveniently stalled at any time window, C=1 in this mode, and eqn (3.4) becomes similar to eqn (3.3). In this case, the relative performance of the single channel and multichannel systems is then determined only by the relative quantum efficiencies when both detectors are in the large signal regime and by the relative dark count rate per channel in the small signal limit. Since, as has been described, in an optimised system D≈2 counts/sec could be expected, the PMT system is likely to outperform even state of the art multichannel detectors at substantially reduced cost.

Finally, it should be noted that a PMT based system may exhibit further advantages in given experimental circumstances because it may be conveniently interfaced with standard analogue signal processing techniques such as phase sensitive detection for modulation experiments eg. luminescence polarisation measurements etc. In addition, where large dynamic range is required (important in TRPL), photomultipliers with a typical dynamic range of 10^6:1 offer improvements over multichannel systems, which typically offer a dynamic range of around 10^4-10^5:1.

3.5 Conclusions

In summary, a commercial Spectra-Physics CW argon ion/dye laser system has been adapted for mode-locked operation at low cost. The performance of the system has been evaluated and shown to be comparable to commercially available systems. An S1 photocathode streak camera system has been used in conjunction with the laser and a limiting time resolution of 24ps has been demonstrated for the laser/streak camera combination when operated in synchroscan mode, similar to that achieved in commercial systems. A novel photomultiplier based single channel readout system has been designed and constructed for the streak camera at low cost. The performance of the readout system has been evaluated and compared with multichannel systems. For scanning applications, the optimised PMT based system is comparable to the best conventional multichannel systems available where the signal strength is weak, and exhibits greater dynamic range in all signal regimes. For single channel time-resolved spectral studies, the current system will exhibit superior signal to noise than any commercially available system whose single channel performance does not match that of a cooled photomultiplier tube.

CHAPTER 4 TIME RESOLVED PHOTOLUMINESCENCE STUDIES OF A STRONGLY COUPLED DOUBLE QUANTUM WELL STRUCTURE AS A FUNCTION OF ELECTRIC FIELD AND TEMPERATURE

4.1 Introduction

In this chapter, time-resolved photoluminescence measurements which have been made on a strongly coupled double quantum well structure are described, and comparison is made with theoretical models. Previous reported TRPL studies in quantum wells as a function of electric field are reviewed and details of the current experimental procedure are described. The results of the PL lifetime measurements as a function of electric field are then presented and compared to theoretical calculations. Finally the variation of exciton lifetime with temperature is presented and successfully fitted to a quantitative theoretical model for the first time.

4.2 Review of Previous TRPL studies of Quantum Wells in Perpendicular Electric Fields

The earliest studies of TRPL in quantum wells as a function of electric field by Kash et al. [4.1] did not show the expected lifetime enhancement with increasing field. Instead (in a 6 period 30Å multi-quantum well), a rapid decrease in the PL lifetime and integrated PL efficiency were observed, consistent with a large increase in the non-radiative recombination rate within the

structure. The field dependent non-radiative component was attributed to extraction of carriers from the well via quantum mechanical tunnelling through the 100 Å AlGaAs barriers, rather than via impurity related non-radiative recombination within the barriers. Non-radiative recombination is often more likely within the AlGaAs barriers because of the lower purity which is typically achieved in MBE growth of AlGaAs in comparison to GaAs. However, the calculated wavefunction penetration into the barrier (≈7% for holes, ≈0.2% for electrons) was judged to be too small in comparison to the calculated tunnelling time ($\approx 10^{-13}$s.) at a typical field of 50kV/cm. Carrier extraction may be considered equalent to a non-radiative recombination process in terms of its effect on the observed PL lifetime (eqn. (2.8)) because the number of carriers available for radiative decay is reduced in exactly the same manner as for true non-radiative decay.

In a later study by Polland et al. [4.2], the expected increase in luminescence lifetime with field was observed in single quantum well samples of widths 50Å, 100Å and 200Å. Greater increases in lifetime were observed for larger well widths, as expected for spatial separation of electrons and holes within the well. Lifetime increases of up to a factor of 100 with absolute values of 100ns were reported in the case of the 200Å well. However, while in agreement with the expected qualitative trend, the measured lifetime increases were in rather poor quantitative agreement with a simple

theoretical calculation based only on the expected variation in free carrier wavefunction overlap integral term, $|\langle\varphi_e(z)|\varphi_h(z)\rangle|^2$. In most cases, the theoretical calculations overestimated the observed increases. Had the calculations included the additional contribution to the lifetime enhancement due to the increase of the exciton radius in the plane of the well, $|\varphi_{eh}(0)|^2$ (as discussed in section 2.3), the agreement would have been even poorer at high fields. This discrepancy between theory and experiment provided part of the motivation for the current work. The data for the 50Å well showed negligible lifetime enhancement at low fields and a rapid decrease in the lifetime for fields greater than 120KV/cm, again attributed to carrier extraction.

More recently Kohler et al. [4.3] have extended the data of ref. [4.2]. A variation in the value of field at which non-radiative effects became significant in the lifetime data was observed in two 214Å SQW samples with different AlGaAs barrier thicknesses, 140Å and 240Å. This result is consistent only with carrier extraction and demonstrated clearly that quantum tunnelling rather than non-radiative recombination in the barriers was the origin of the reduction in luminescence lifetime at high fields in these samples. However, as in [4.2], a similar discrepancy between theory and experiment was observed in the lifetime data and the effect of excitonic binding was again neglected.

4.3 Details of the Experimental Arrangement for the TRPL Measurements and Description of the CQW sample

The complete experimental arrangement used in these studies is shown schematically in figure 4.1. The samples were mounted in an Oxford Instruments 1204 continuous flow helium cryostat and illuminated by radiation from the mode-locked Styryl-8 dye laser at an angle of 45° to the sample normal. The laser radiation was focussed onto the sample by a spherical lens (L6 in fig. 4.1) for high excitation densities, and by an additional cylindrical lens (L7) when lower excitation densities were required. Cylindrical lenses were used so that lower excitation densities could be achieved with minimum loss of total signal. The lenses were mounted on a 50cm length of optical bench so that the excitation density could be conveniently varied. The luminescence was collected at 45° to the sample through a second output window by a 5cm diameter 8cm focal length lens (L5) and imaged onto the input slit of a Bentham 1/4m grating monochromator which was used to spectrally disperse the luminescence and filter the elastically scattered laser light. Because the rejection of the 1/4m monochromator was relatively poor, the elastically scattered light was additionally filtered by a 780nm high pass filter (Schott RG780) prior to entering the monochromator and a stop was used to spatially filter the specular reflection from the sample surface. The output from the monochromator was collected by a 5cm diameter 10cm focal length lens (L3) and focussed into the input slit of the streak camera using a

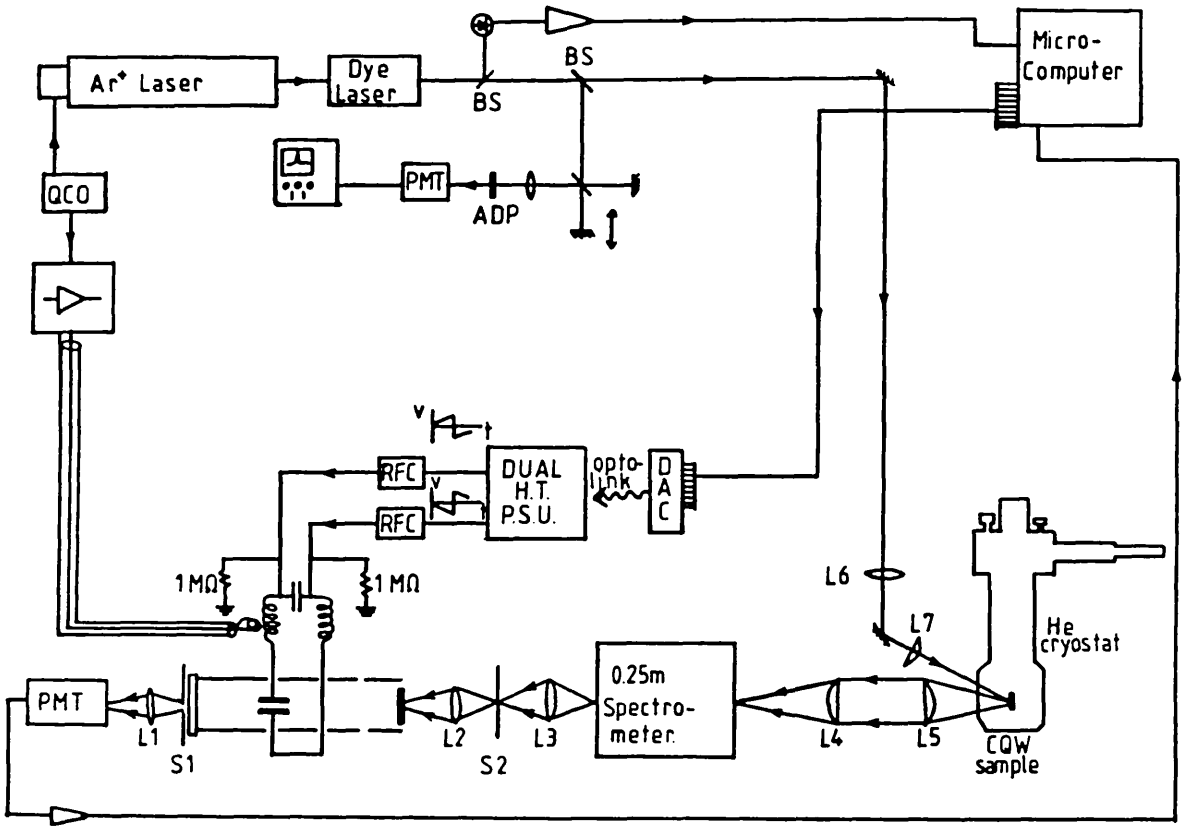


Figure 4.1 Schematic Diagram of the Time-Resolved Photoluminescence apparatus

5cm diameter 3.9cm focal length aspherical lens (L2). The final lens was chosen to have the smallest possible focal length without falling below the f number of the streak camera input optics in order to demagnify the image of the monochromator output slit so that the smallest possible streak camera input slit width, and hence highest possible temporal resolution, could be used. The sample temperature was controlled using an Oxford Instruments 3120 temperature controller with standard Au/Fe/Cr thermocouple sensor, and also by a calibrated Allen Bradley resistor mounted on the cold finger adjacent to the sample. When hysteresis was observed between the two sensors, the Allen Bradley resistor was taken as the best measure of the sample temperature. The details of the modelocked dye laser and streak camera system illustrated in figure 4.1 are contained within chapter 3.

The coupled quantum well (CQW) sample used in this study was identical to that studied by Andrews et al. [2.16]. The sample was grown by molecular beam epitaxy on a Si doped (100) GaAs substrate and is shown schematically in figure 4.2. The sample dimensions shown have been adjusted slightly from the nominal growth specification in order to match the calculated zero field PL line position to that observed. The use of a single quantum well structure (rather than a multiple quantum well) is important in electric field studies in order to eliminate well-to-well field inhomogeneity through the sample. However, this is achieved at the price of reduced PL signal strength.

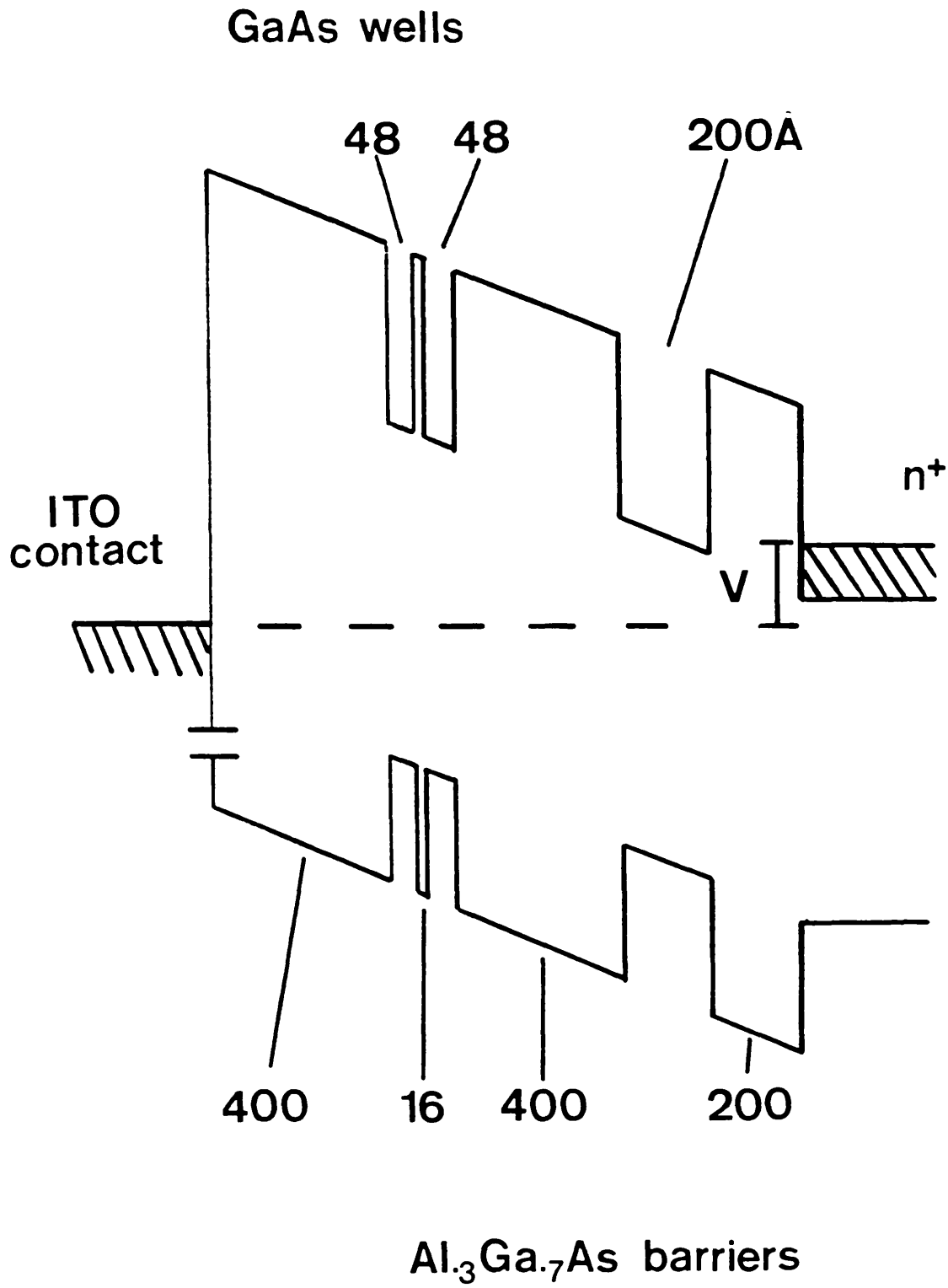


Figure 4.2 Diagram of the Coupled Quantum Well structure used in this study, indicating the structure dimensions, the ITO Schottky contact and the built-in internal voltage. The properties of the 200Å well are ignored in this study.

A perpendicular electric field was applied to the structure by means of a 5mm diameter 100nm thick sputtered Indium Tin Oxide (ITO) Schottky barrier contact at the top surface of the sample and by an Indium soldered wire contact to the n+ substrate. The thickness of the ITO layer was chosen to form an anti-reflection coating with 95% transmission at 800nm. Contact to the ITO layer was made using thin copper wire adhered to the sample by silver loaded paint (Demetron Contacting Silver 200). The painted contact could be easily washed away using acetone, allowing easy cleaning of the sample and reducing the risk of permanent damage associated with permanent contacting techniques. The ITO Schottky contacts were prone to damage if exposed to large voltage spikes such as those generated by mains switch-on transients in mains powered equipment. Consequently, bias voltage was applied to the sample only through a battery powered DC voltage supply using a 3KΩ current limiting series resistor and measured using a battery powered DVM.

4.4 Results of the TRPL measurements on the Coupled Quantum Well structure as a function of Electric Field at 4.2K

4.4.1 Description and Interpretation of the Experimental Data

Figure 4.3 shows (curve A) the PL emission line position at 4.2K as a function of applied bias voltage at an excitation density of 2×10^9 excitons/cm^2. The excitation

densities were calculated throughout assuming an absorption coefficient of $1x10^{6}m^{-1}$. The excitation wavelength, 735nm, was used throughout these studies, except where the excitation wavelength dependence of the PL lifetime was being investigated explicitly. An excitation wavelength close to the bandedge was chosen in order to minimise any hot carrier effects due to non-equilibrium heating of the photocreated exciton population by large excess photon energies. Net zero field across the sample, where the in-built field of the Schottky barrier contact was perfectly cancelled by the external bias, was determined from the minimum Stark shift in the PL line position and found to correspond to a bias voltage of +1.05V. The measured curve was in close agreement with that measured in ref [2.16] except that for a small uniform shift of 5Å to shorter wavelength, attributable to slight differences in the sample thickness between different parts of the wafer. However, a 5Å shift is equivalent to less than a 1 monolayer shift in total well width at these confinement energies, so the same adjusted sample parameters adopted in ref [2.16] have been adopted here for the lifetime modelling. Also shown (curve B) is the expected Stark shift with bias obtained from resonant tunnelling calculations assuming a uniform distribution of bias voltage through the structure, indicating a discrepancy between the predicted and measured Stark shifts using this method of estimating the field. A similar discrepancy was also observed in <u>all</u> the PLE peaks measured in ref.[2.16], although the correct qualitative behavior with applied bias was predicted in every case. This

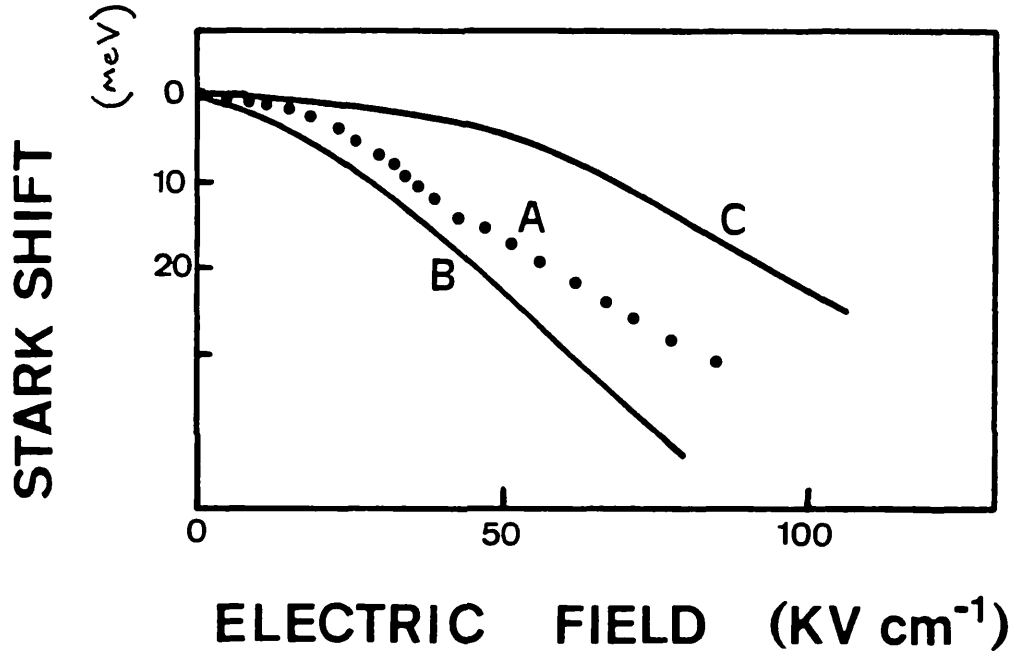


Figure 4.3 Curve A: Stark shift in the PL line position vs. electric field in the coupled quantum well at 4.2K. Curve B: calculated Stark shift for the CQW obtained from a resonant tunnelling calculation by distributing the electric field uniformly throughout the structure. Curve C: calculated Stark shift for a 100Å well illustrating the enhanced Stark shift in the coupled quantum well case.

is clear evidence of field non-uniformity through the sample, which is often observed in structures of this type. Field inhomogeneity has clear implications for successful modelling of the lifetime data, since if the Stark shifts predicted by the model using uniform field distribution do not agree with measurement, then calculation of envelope functions (and hence lifetimes) using the same field values will inevitably produce disagreement with experiment, irrespective of the quality of the envelope function calculation. However, the variation of Stark shift with electric field in quantum wells is now well understood, the accuracy of the resonant tunnelling method in calculating these shifts has been established by many studies, and the calculated Stark shift has been shown to be largely insensitive to the actual form of the free carrier envelope functions (see section 2.3). For these reasons and following Miller et al. [1.1], the measured Stark shift was used to calculate the true electric field across the well with no loss of accuracy. In what follows, this procedure has been adopted, including the small correction (≈5%) due to the variation in exciton binding energy with electric field which must be subtracted from the Stark shift in the subband energy. Also shown in fig. 4.3 for comparison is the calculated Stark shift as a function of electric field for a 100Å single quantum well, demonstrating the larger Stark shifts that may be obtained in a coupled quantum well (curve C).

Figure 4.4 shows the time resolved luminescence profiles

from the CQW at 1.05V (zero field) and at 0V (close to the maximum effective field used). The profiles were measured at 4.2K with an excitation density of $2x10^9$ excitons/cm^2 and an excitation wavelength of 735nm. The profiles are indicative of the exponential decays obtained throughout the measurement range. Throughout these studies, data quoted at 4.2K was taken with helium liquid condensed into the sample space in order to eliminate any local sample heating by the laser or hysteresis between the sample and sensor temperatures. The excitation density was measured by careful measurement of the area of the isotropically scattered light imaged onto the monochromator input slit and dividing by the square of the magnification of the collection optics (lenses L4 and L5: magnification 2.3). The input power was measured using a calibrated photodiode. The data was obtained from 4 coadded streak camera scans each of 1020 points taken at 10 points/sec using an amplifier time constant of 0.5s. A monochromator bandpass of 1.5nm (3meV) was selected in order to pass all the luminescence from the CQW and the streak camera resolution was set at 50ps. A zero field lifetime of 151ps was obtained by least square fitting ln(I(t)) to a straight line. At 0 Volts (53kV/cm), a lifetime of 1250ps was obtained, an enhancement in the lifetime of 8.3. The observation of an exponential decay demonstrates that (in the absence of non-radiative effects) the PL emission is excitonic in origin. The background carrier density in the (nominally undoped) region of the quantum wells is $\approx 1x10^8$ cm^{-2}, much less than the photocreated electron-hole density, so that majority carrier

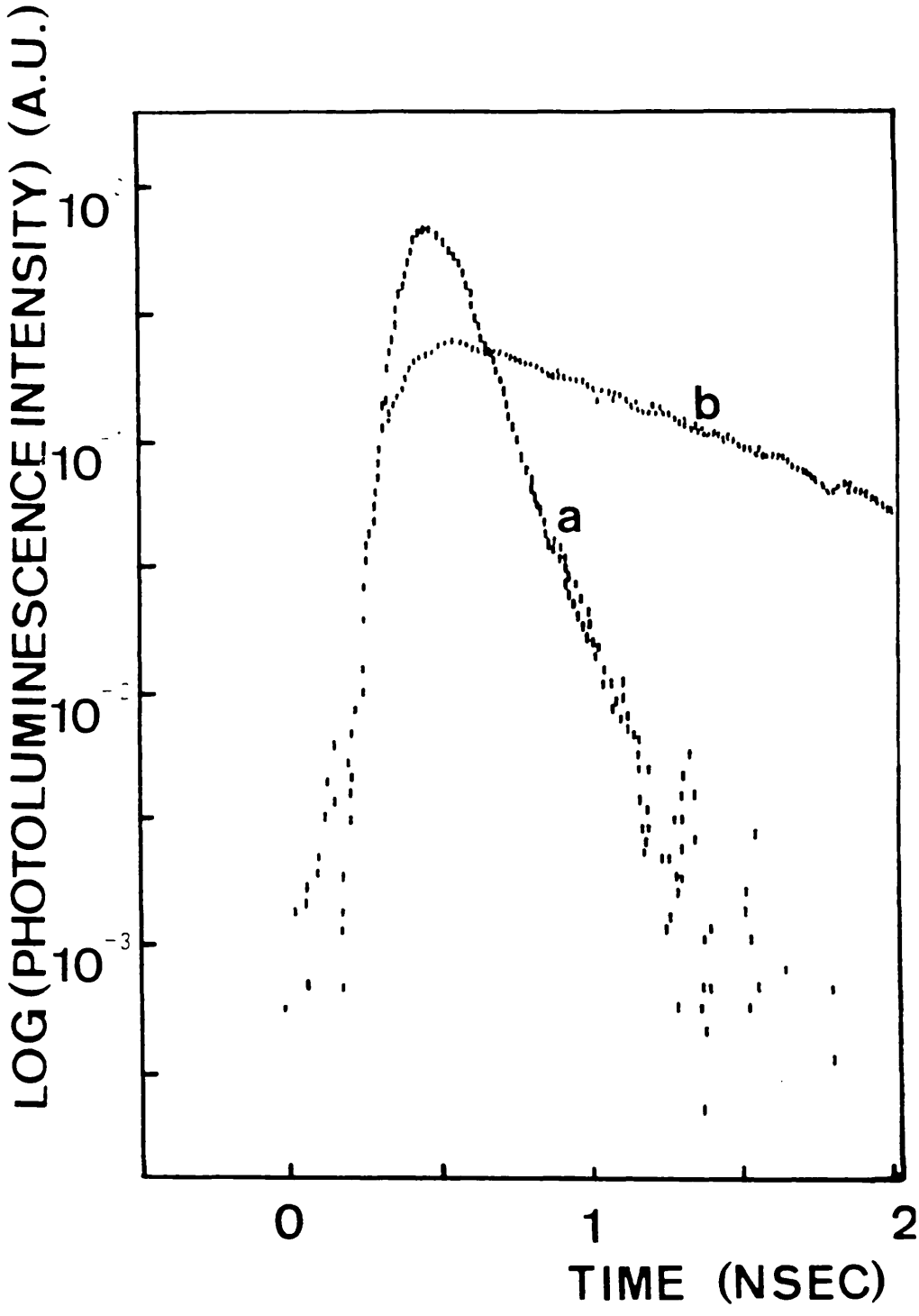


Figure 4.4 TRPL profiles from the CQW at a) zero field (τ=151ps) and b) 53kV/cm (τ=1250ps), corresponding to a lifetime enhancement of 8.3.

dominated bi-molecular recombination dynamics (see section 2.2), which would also result in an exponential decay, may be discounted.

The variation of PL lifetime with excitation density (figure 4.5) was investigated in order to check for the presence of hot carrier effects or for non-radiative traps. The presence of a significant non-raditive rate would have a major effect on the lifetime data (from eqn. 2.8) and would invalidate any determination of the dependence of radiative lifetime with field since the measured lifetime would become a combination of the true radiative lifetime and a non-radiative component (likely to contain its own field variation), making the true radiative lifetime impossible to extract reliably. Fig. 4.5 shows that the lifetime was constant to within 5% over a factor of 40 variation in excitation density around $2x10^9$ excitons/cm² at 735nm. The lifetime was also found to be unchanged by excitation at 755nm, as also indicated in fig. 4.5. Since the exciton radiative lifetime was also found to be a strong function of temperature above 4.2K (see sections 2.4, 4.5), this indicated that hot carrier effects were not present at 735nm at these excitation densities and that the photocreated exciton population had reached thermal equilibrium with the lattice. This conclusion is supported by the observation of exponential decay profiles: the observed variation of PL lifetime with sample temperature (see section 4.5) implies that a non exponential decay would be expected in the case where the exciton population was cooling on a timescale

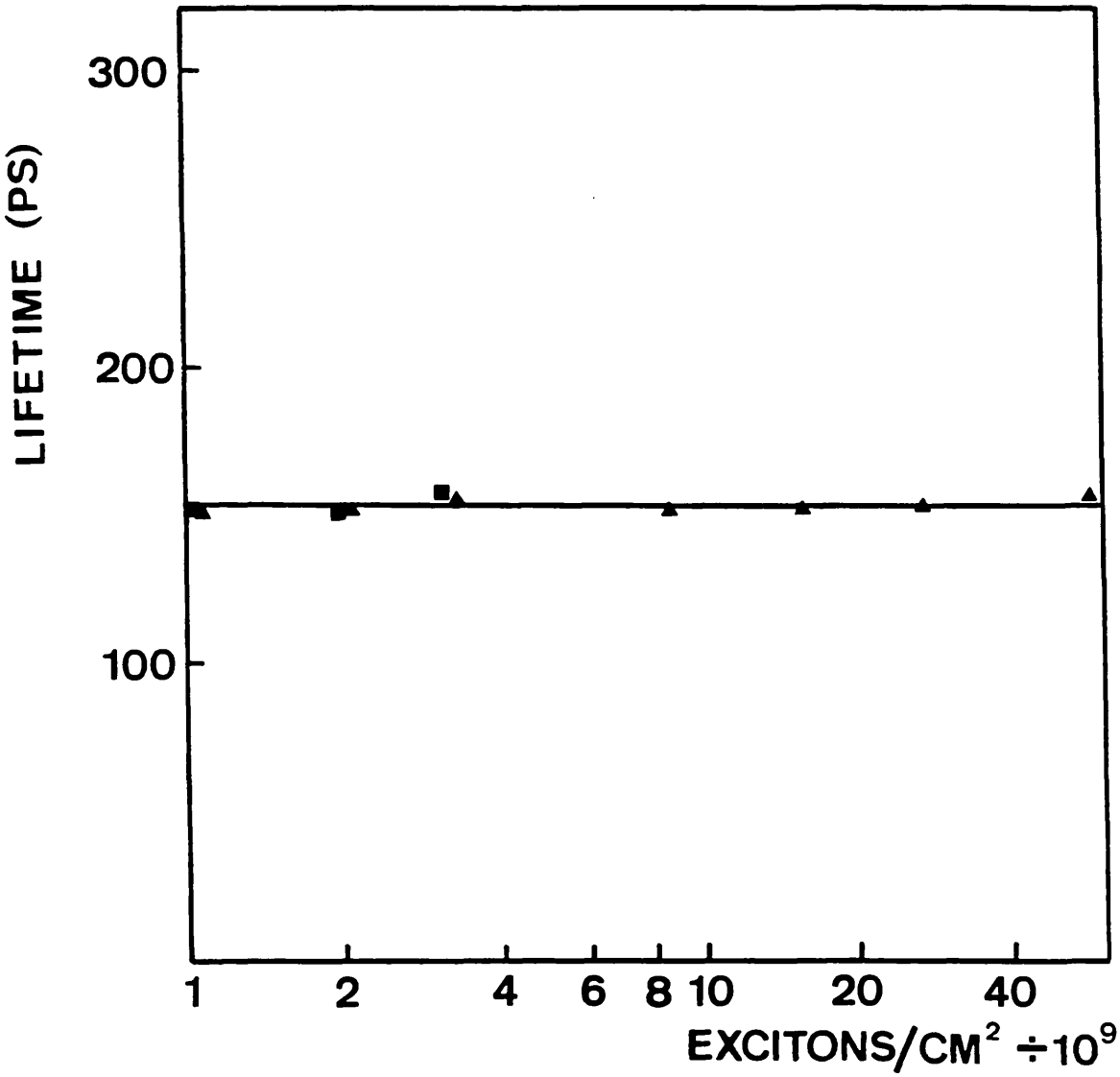


Figure 4.5 Zero field PL lifetime vs. excitation density in the CQW at 4.2K for excitation at 735nm (triangles) and 755nm (squares).

comparable with its radiative lifetime. Masumoto et al. [4.4] used a simple calculation to show that for a 76Å MQW and an excitation density of $2x10^{10}$ excitons/cm², the exciton population would reach thermal equilibrium with the lattice (at 4.2k) after 24ps by LA phonon emission. The absence of hot carrier effects in the CQW lifetime data tends to support the validity of this calculation at the excitation densities used here.

An exponential luminescence profile is not in itself evidence of pure radiative decay. Other workers [4.5] have observed increases in lifetime for higher excitation densities and attributed the constant lifetime at lower densities (comparable to those used here) to recombination at non-radiative traps which become saturated at higher excitation densities. In this work, however, the strong increase in PL decay time with electric field combined with luminescence efficiency measurements provides independent evidence that it is the true radiative decay time that is being measured in this sample.

Figure 4.6 shows the measured variation in PL lifetime as a function of electric field (as calculated from the Stark shift fitting procedure) at 4.2K for excitation at 735nm and at $2x10^{9}$ excitons/cm^2. The same variation was measured for other excitation densities and for excitation at 755nm (also shown). The data in fig. 4.6 has been expressed as a "lifetime enhancement factor", $\tau(E)/\tau(0)$, where $\tau(0)$=151ps, the measured lifetime at zero field bias. In this way, the

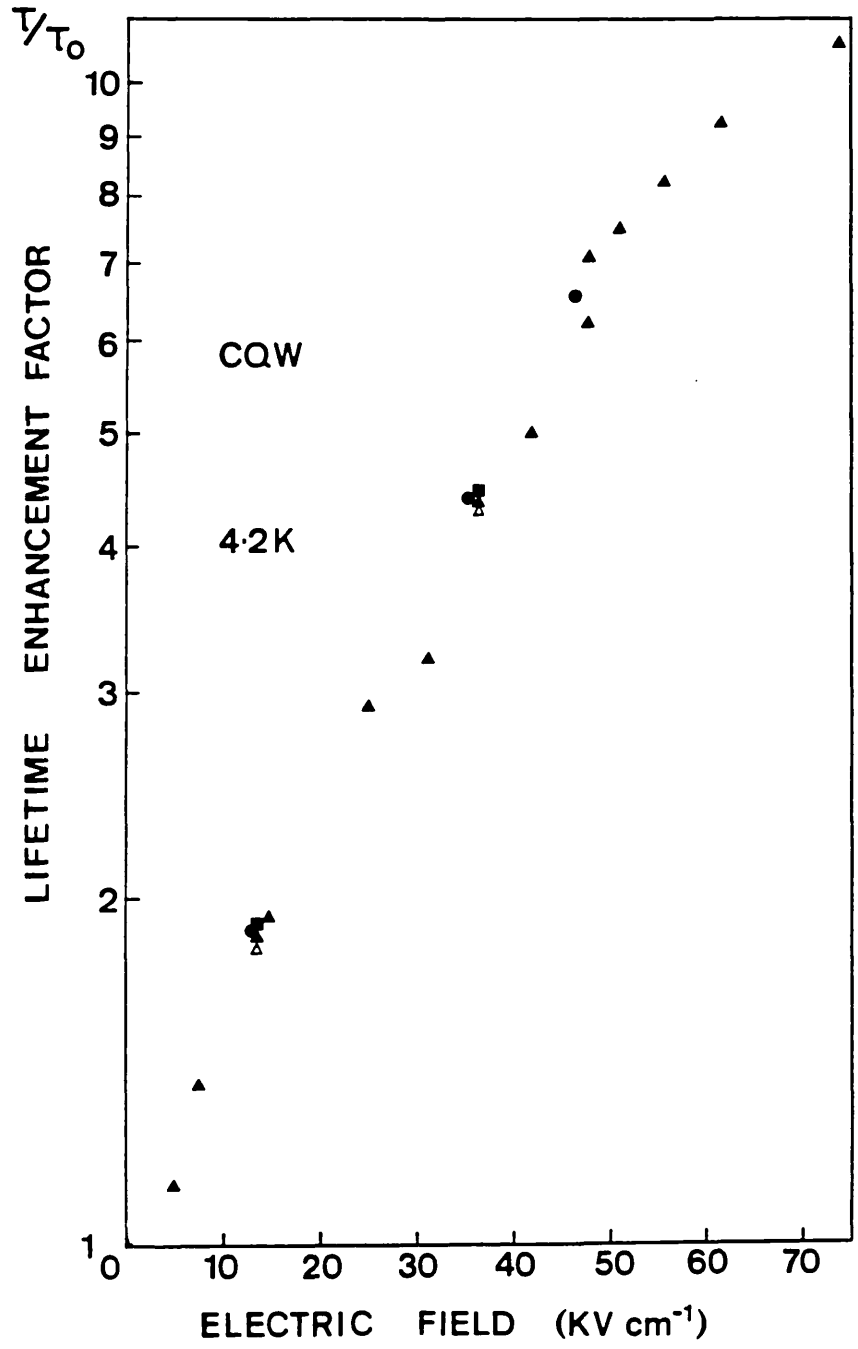


Figure 4.6 Variation in "lifetime enhancement factor", $\tau(E)/\tau(0)$, as a function of electric field at 4.2K for various excitation conditions. Triangles: 735nm and $2x10^9$ excitons/cm² (laser intensity I). Open triangles: 735nm and 2I. Squares: 735nm and I/2. Dots: 755nm and I.

variation in lifetime due to field dependent changes in the exciton wavefunction may be compared directly, ie. the contribution to the lifetime in eqn. (1.10) due to the bulk oscillator strength, f_o, cancels when the ratio $\tau(E)/\tau(0)$ is taken. If eqn. (1.10) holds, the lifetime enhancement factor is independent of the absolute value of the radiative lifetime at zero field.

4.4.2 Details of the lifetime modelling calculations

The theoretical calculations were performed within the effective mass and envelope function approximations using the Hamiltonian of (2.9b) and the variational exciton wavefunction of eqn. (2.9):

$$\Phi_{ex} = \varphi_e(z)\ \varphi_h(z)\ \exp(-p/a) \qquad \text{eqn. (4.3)}$$

assuming a 1s-like wavefunction for $\varphi_{eh}(p)$.

The theoretical lifetime enhancement factor was evaluated using the expression (from eqns. (1.10) and (1.11)):

$$\frac{\tau(E)}{\tau(0)} = \frac{a(E)^2}{a(0)^2}\ \frac{|\langle\varphi_e(z)|\varphi_h(z)\rangle|^2_{(E=0)}}{|\langle\varphi_e(z)|\varphi_h(z)\rangle|^2_{(E)}} \qquad \text{eqn. (4.1)}$$

where a 1s-like exciton envelope function has been assumed, and so $|\varphi_{eh}(0)|^2$ is proportional to $1/a^2$. Where a, the effective exciton radius, is a function of field. (The relationship $\tau\alpha|\varphi_{eh}(0)|^{-2}$ remains true even in the presence of an electric field [4.6])

The free carrier envelope functions in the z direction, $\varphi_e(z)$ and $\varphi_h(z)$, were calculated at a given field by numerical integration of the 1D Schroedinger equation (eqn 2.10) using an energy calculated using the resonant tunnelling method. The values of perpendicular effective mass were those used by Miller and Kleinmann [4.7]. The parameter, a, was calculated at a given field by variational minimisation of $\langle\Phi_{ex}|\underline{H}_{eh}|\Phi_{ex}\rangle$, using φ_e, φ_h calculated from the tunnelling resonance calculation at that field, where:

$$\underline{H}_{eh} = \frac{-\hbar^2}{2\mu}\left[\frac{d^2}{dr^2} + \frac{1}{r}\frac{d}{dr}\right] + \frac{e^2}{4\pi\varepsilon_o\varepsilon_r|\underline{r}_{eh}|} \qquad \text{eqn. (4.2)}$$

And:

$$r=\sqrt{[x_{eh}^2+y_{eh}^2]} \qquad \text{eqn. (4.4)}$$

$$r_{eh}=\sqrt{[r^2+z_{eh}^2]} \qquad \text{eqn. (4.5)}$$

as before in section 2.3; where x_{eh}, y_{eh}, z_{eh} are the relative separation of the electron and hole in the x, y, z directions. (Other terms in $\underline{H}$ (eqn.(2.9b) were included in the evaluation of φ_e and φ_h and so are omitted from $\underline{H}_{eh}$)

Two possible expressions for p have been considered, corresponding to the non-separable and separable cases discussed in section 2.3. For the separable case, where electron-hole separation in the z direction is determined only by the confinement potentials, with negligible contribution from coulomb attraction, $p=|r|$. For the non-separable case, coulombic binding is not negligible in the z direction: $p=|r_{eh}|$.

The following values were used in eqn. (4.2). ε_r=12.15, the geometrical average of the background dielectric constants in GaAs and $Al_xGa_{1-x}As$; x=0.3; and $\mu=0.046m_o$, the effective mass of the heavy hole exciton using Luttinger parameters γ_1=5.47, γ_2=1.26 and γ_3=0: the average values of those obtained by Plaut et al. [4.8] in magneto-reflectivity measurements in single quantum wells of widths 77Å ($\mu=0.049m_o$) and 112Å ($\mu=0.045m_o$). The calculations neglect the effect of light and heavy hole sub-band mixing [4.9], and the discontinuity of parallel effective mass at the heterojunctions [4.10].

4.4.3 Comparison between theory and experiment

Figure 4.7 shows the theoretical calculation (curve a) superimposed on the data of fig. 4.6 (triangles), showing that close quantitative agreement between the measured variation in PL lifetime and that calculated by a variational calculation including excitonic effects has been obtained for the first time in a quantum well. Also indicated for comparison (curve b) is the calculated enhancement due to separation of the electron and hole in the z direction alone, ie. due to the $|\langle\varphi_e|\varphi_h\rangle|^2$ factor only in eqn. (4.1). This demonstrates that the inclusion of the variation of excitonic binding in the plane of the well as a function of electric field is essential to accurately model the observed lifetime variation. The calculated curve is not strongly sensitive to different choices of μ, the in-plane

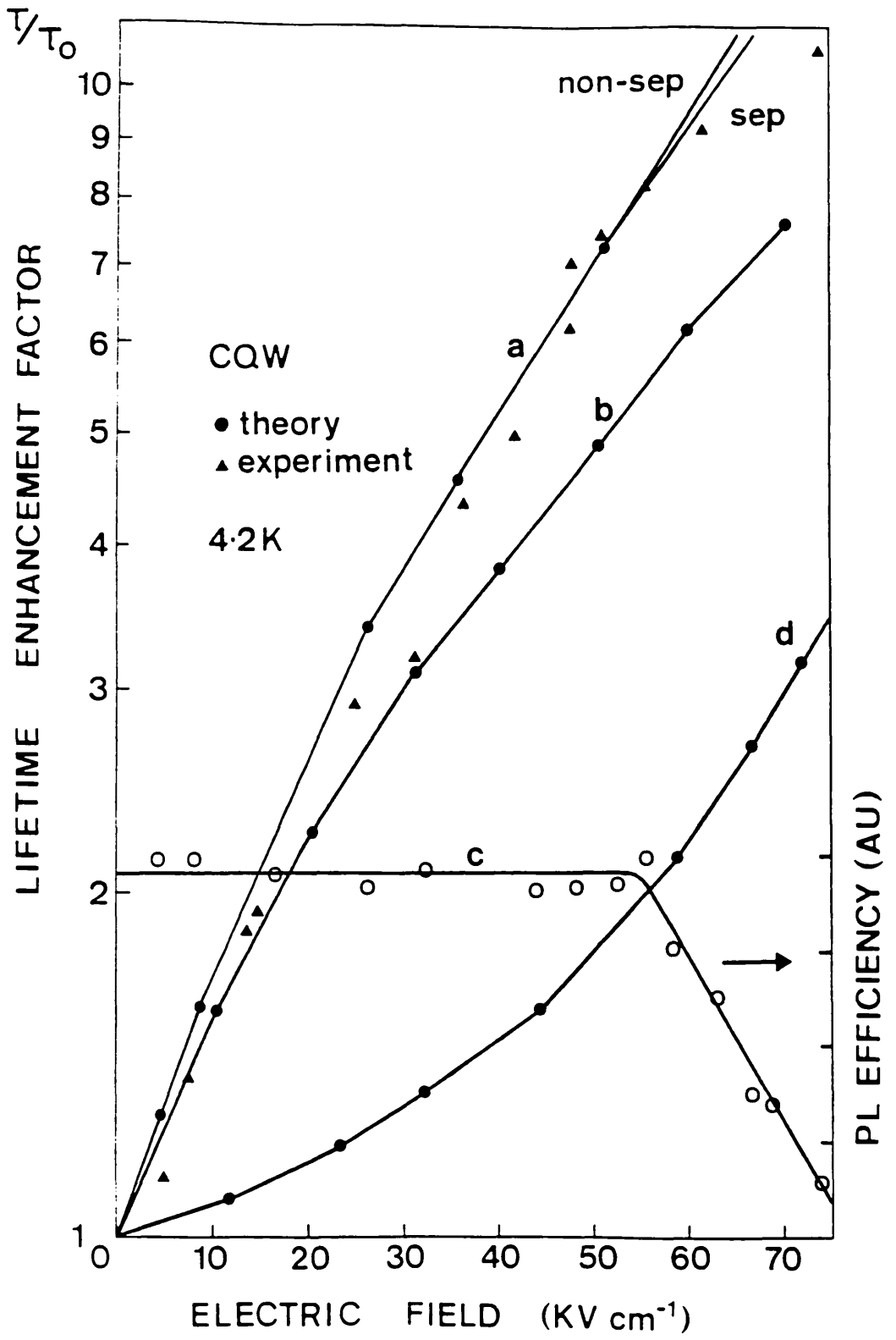


Figure 4.7 Lifetime enhancement factor (LEF), $\tau(E)/\tau(0)$, vs.electric field at 4.2K for excitation at 735nm at an excitation density of 2×10^9 excitons/cm² (triangles). Curve a: LEF calculated from theory described in text. Curve b: LEF calculated considering variation in $\langle\varphi_e(z)|\varphi_h(z)\rangle$ only. Curve c: PL efficiency as a function of electric field. Curve d: full LEF calculation for a 100Å well.

exciton reduced mass: using $\mu=0.049m_o$ generates only a 3% change in lifetime enhancement factor at a field of 100 KV/cm. Above 70KV/cm, the lifetime enhancement saturates, consistent with the onset of a significant non-radiative recombination component. This was confirmed by time-integrated PL efficiency measurements under the same experimental conditions (curve c in fig. 4.7) which showed a rapid fall in the PL efficiency beyond 70KV/cm. It was not possible to extend the field regime to observe the expected fall in the PL lifetime when the non-radiative rate becomes sufficiently large (after Kohler et al. [4.3]) because the quenching of the PL signal was too severe. The observed increase in PL lifetime as the field is increased, coupled with the integrated PL efficiency measurement which indicates constant luminescence efficiency for E<70KV/cm, is unambiguous evidence that the PL lifetime is equal to the true radiative lifetime in this field regime. For a zero field PL lifetime that was dominated by a large non-radiative decay component, an immediate increase in PL lifetime for fields greater than zero would not be expected, a constant or rapidly falling PL lifetime being more plausible. The rise in lifetime under such circumstances could only be explained by a highly non-uniform distribution of non-radiative centres, concentrated at the centre of the the GaAs well, in contrast to the common situation where the impurities are typically concentrated in the barrier. For impurities concentrated at the centre of the well, the non-radiative rate could fall as the field is applied as the exciton wavefunction is

displaced from the centre of the well and the measured PL lifetime would rise towards the true radiative lifetime. However, this (unlikely) explanation is ruled out by the constant PL efficiency measurement since a rise in PL efficiency with field would be expected under these conditions. Figure 4.7 therefore demonstrates clearly that true radiative decay times are being measured here and that the agreement between experiment and theory is indeed significant.

Figure 4.7 also indicates the divergence between the separable and non-separable solutions which only becomes significant at high fields where the field induced electron-hole penetration of the barriers is large. Unfortunately, it is not possible to observe any tendency towards the non-separable solution at high fields in the measured data due to the onset of the non-radiative component. If the non-radiative effect is attributable to quantum tunnelling, thicker barriers would be required to observe this effect. Nevertheless, the results demonstrate that in general the non-separable solution need only be considered for lifetime enhancement factors greater than 10. Also shown in figure 4.7 (curve d) is the calculated lifetime enhancement for a 100Å well, indicating that larger enhancements are obtained in a coupled quantum well structure than in a SQW of the same overall width, consistent with the larger Stark shifts observed in previous CW studies [2.15][2.16], and demonstrating that the behavior of the coupled quantum well is well understood. Since the lifetime enhancement is

essentially determined by the variation in exciton wavefunction, the close agreement between theory and experiment observed here means that the exciton wavefunction of eqn. (4.3) has been accurately characterised as a function of electric field in this sample. As discussed in section 1.3, the lifetime enhancement is strongly sensitive to the exciton wavefunction, so the good agreement between experiment and calculation here allows the exciton binding energy to be measured with greater accuracy than by other methods. Figures 4.8 shows the variation in exciton binding energy with electric field in the CQW, as calculated from the measured variation in lifetime, superimposed on the comparison of binding energy calculations published by Nojima [2.10], as discussed in section 2.3. Greater reductions in binding energy are observed in the coupled quantum well case than in the calculated values for single quantum wells of comparable widths, again consistent with the overall model of the structure. Figure 4.9 shows in more detail the reduction in binding energy and increase in the variational parameter a, the effective 2D exciton Bohr radius, as a function of electric field. It should be noted that the binding energy does not in fact fall as fast as the square of the exciton radius increases. This indicates that the ideal 2D exciton binding energy expression:

$$E_{be} \propto 1/a_{2D}^2 \qquad \text{eqn. (4.8)}$$

is not perfectly satisfied in this sample, demonstrating that the exciton does not quite approach the ideal 2D limit.

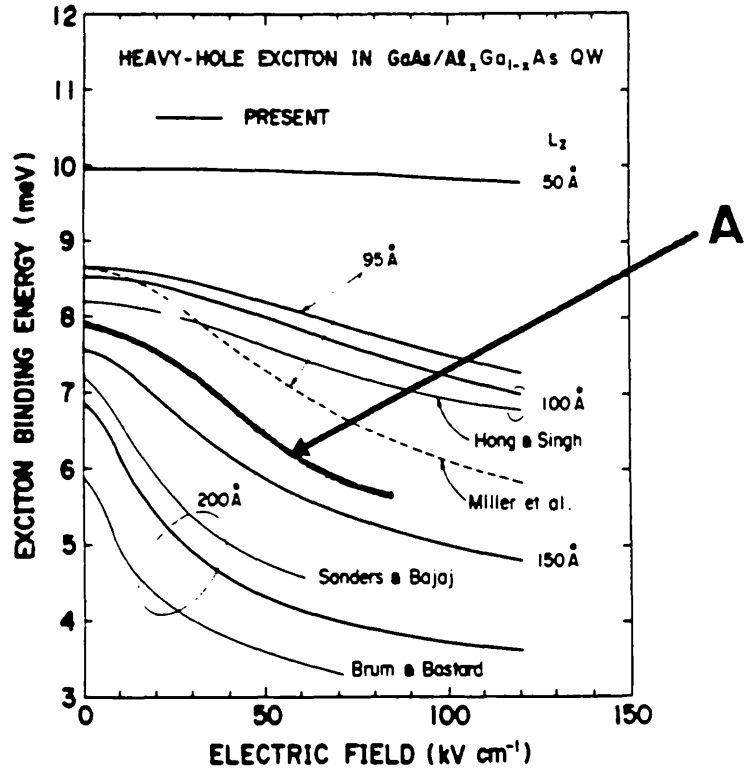


Figure 4.8 Exciton binding energy vs. electric field, as calculated by different workers and summarised by Nojima [2.10]. Curve A is the variation for the CQW calculated using the method described in the text, and demonstrating the larger reduction in binding energy obtained for a CQW compared to comparable SQW's.

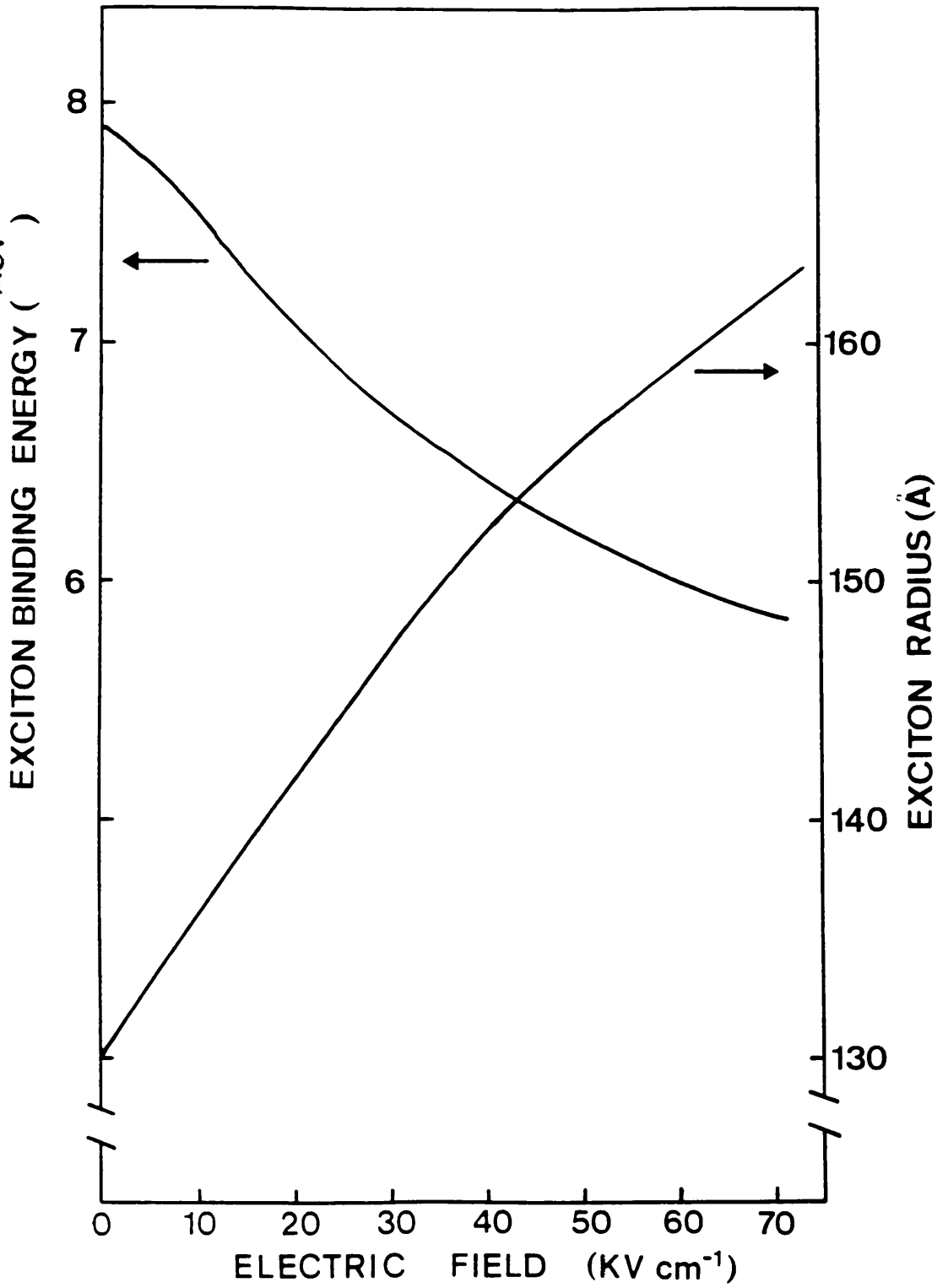


Figure 4.9 Calculated exciton binding energy and exciton radius, a, vs. electric field in the CQW, obtained using the exciton envelope function calculation described in the text.

4.5 TRPL measurements on the Coupled Quantum Well structure between 4.2K and 60K

4.5.1 Description and Interpretation of the Experimental Data

The TRPL measurements were also repeated at temperatures between 4.2K and 60K. Figure 4.10 shows the variation in PL lifetime at zero net electric field (+1.05V) in this temperature regime. The observed increase with temperature may be explained by the coherence area arguments developed by Feldmann et al., described in section 2.4. The variation in lifetime enhancement factor is shown in fig. 4.11 for T=12K, 18K and 27K. In each case, $\tau_o(T)$ is the zero field lifetime measured at that temperature. The solid curve is the same theoretical calculation used in the 4.2K data of fig. 4.7. The same close agreement with calculation shown in fig. 4.11, demonstrates that the electric field dependence of the radiative lifetime is not strongly affected by temperature up to at least 27K. The agreement with the variational calculation remains good despite a factor of 3 increase in zero field lifetime over the temperature range. This result is consistent with the coherence volume argument applied to the factorisable exciton envelope function (eqn. (2.9) with the centre of mass term, $\exp(-\underline{K}.\underline{R})$, not neglected), which separates the centre of mass motion of the exciton (responsible for the temperature dependence) from the relative separation of the electron and hole (responsible for the electric field dependence). It was not

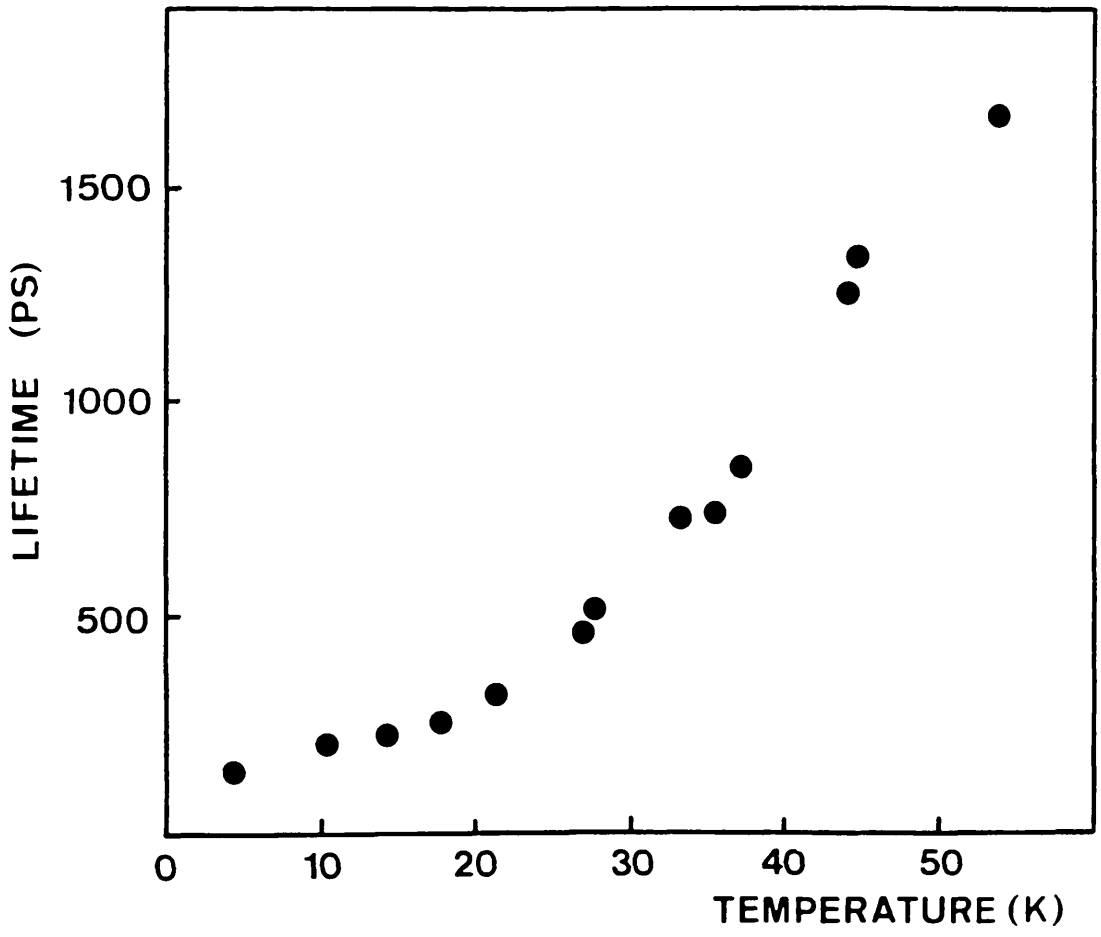


Figure 4.10 PL lifetime vs. temperature in the CQW at zero electric field.

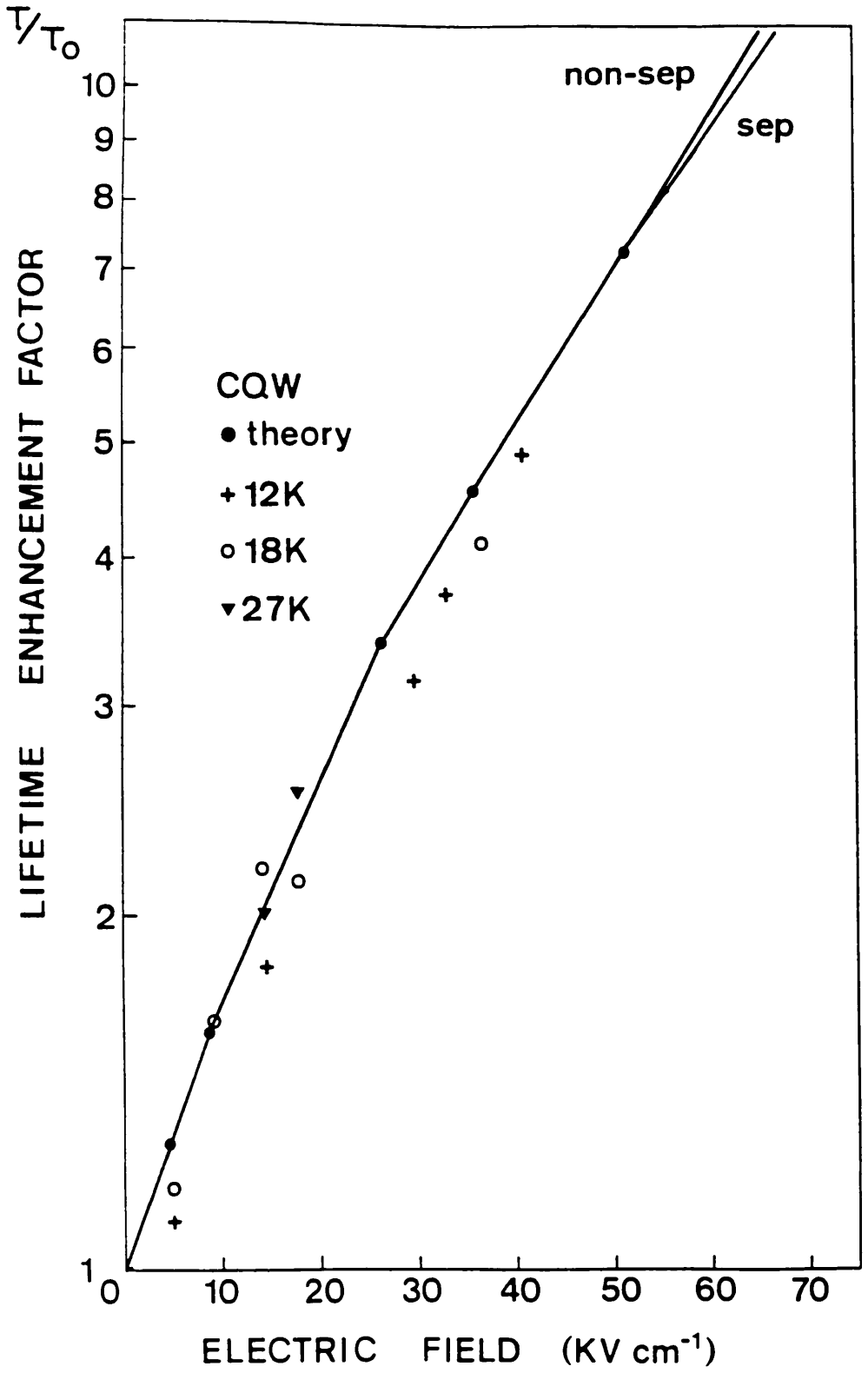


Figure 4.11 Lifetime enhancement factor vs. electric field at 12K, 18K and 27K; indicating close agreement with the envelope function calculation in this temperature regime.

possible to measure the PL lifetime over the entire range of fields and enhancement factors investigated in the 4.2K case because of the onset of the non-radiative component at lower fields and also because the lifetimes became comparable to, or longer than, the streak camera scan period so that streak wrap-around effects became significant. For the same reason it was not possible to measure the field dependence of the radiative lifetime beyond 27K. Nevertheless, over the range of temperatures and fields indicated by fig. 4.11, the agreement with the variational calculation remains close, indicating that true radiative lifetimes are still being measured and further demonstrating the absence of non-radiative effects in the sample.

The detailed form of the temperature dependence of the zero field lifetime, $\tau_o(T)$, differs from most of the data presented by Feldmann et al. [2.12] (fig. 4.12). In the coupled quantum well data, a linear dependence on temperature is only observed for the CQW above 30K. The sublinear dependence for T<30K is only similar to that reported in the 25Å SQW sample in ref [2.12]. This behavior was tentatively attributed to localisation of the exciton wavefunction in regions of wider well width (where the confinement energy is lower), imposing an upper limit on the allowed exciton coherence area and hence a lower limit on the radiative lifetime. It might be expected that the CQW would exhibit larger localisation effects than single quantum well structures of comparable width because the presence of the central dividing barrier effectively

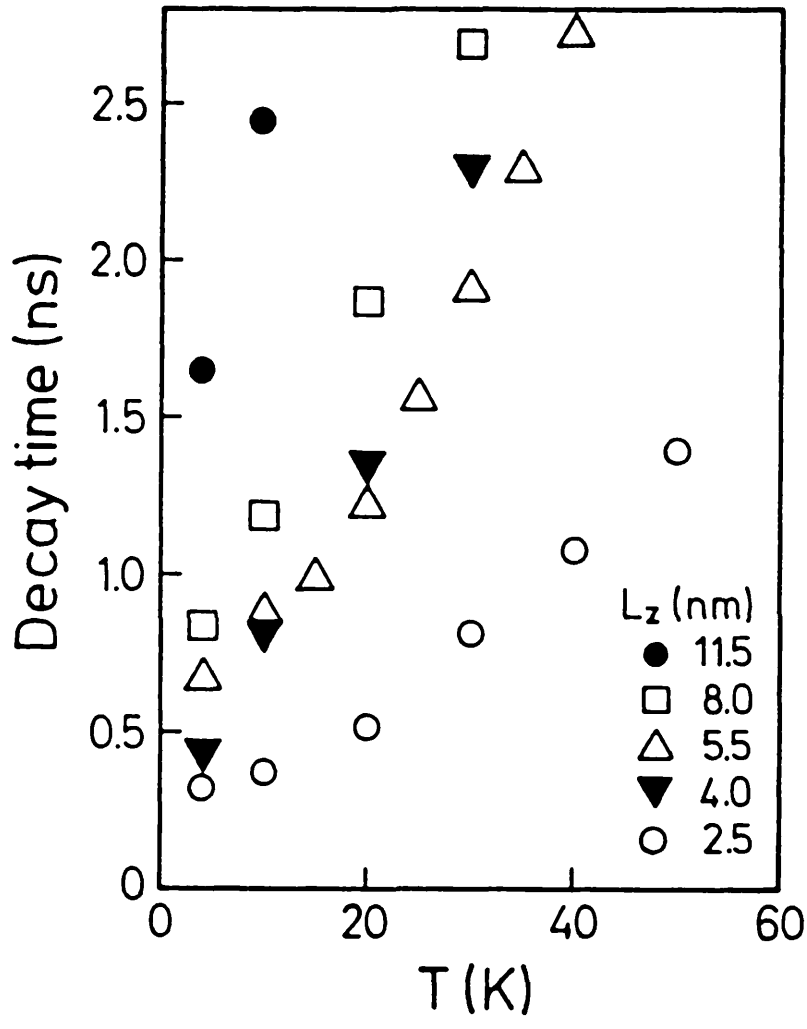


Figure 4.12 The PL lifetime vs. Temperature for MQWS of different well widths obtained by Feldmann et al. [2.12].

doubles the density of monolayer well width fluctuations compared to a SQW of comparable interface roughness. In this way, the similarity of the CQW data to the 25Å well rather than the 55Å or 80Å wells might be expected. The tentative assignment of the sub-linear behavior to localisation was supported by the prominence of the effect only in the narrower samples (the effect is also observable to a lesser extent in the 40Å and 55Å wells). This is because the probability of localisation is highest in narrower wells since a monolayer change in well width causes the largest percentage change in confinement energy when the well width is itself small, and the confinement energy is the strongest function of well width. However, in the absence of complementary homogeneous linewidth or luminescence efficiency measurements for the 25Å well, it is not possible to definitely exclude alternative explanations. In the case of a significant temperature dependent non-radiative rate which acts to shift the entire curve down at low temperature, coupled with a larger value of homogeneous linewidth in the narrower well, sublinear behavior of the form observed could be generated. The non-radiative rate would be expected to be largest in the narrower wells where the penetration of the wavefunction into the barrier is largest. Takagahara [4.10] has predicted theoretically that acoustic phonon scattering rates (which are the main intrinsic contribution to the homogeneous linewidth below 80K in the delocalised regime [2.13]) are a strong function of well width. In addition, a larger defect related scattering rate might also be expected, again due to barrier

penetration.

4.5.2 Theoretical modelling of $\tau(T)$

The current study offers an opportunity to investigate the temperature dependence of the exciton lifetime further. The electric field measurements have shown that in the case of the coupled quantum well sample, the PL lifetime is equal to the true radiative lifetime between 4.2K and 27K. PL efficiency measurements (to ±10%) have shown that this remains true at zero field up to 50K. The absence of non-radiative effects allows the absolute value of lifetime to be used to attempt a calculation of the homogeneous linewidth for the CQW sample. From eqns. (2.16) and (2.17), τ and Γ are related by:

$$\tau = \frac{2\pi\varepsilon_o m_o c^3}{ne^2w^2} \frac{1}{f_o} \frac{MA_x}{4\pi\hbar^2} \frac{\Gamma(T)}{r(T)} \qquad \text{eqn. (4.9)}$$

$$= \frac{\Gamma(T)/R(T)}{f_o KL}$$

with $K=ne^2w^2/2\pi\varepsilon_o m_o c^3$ and $L=4\pi\hbar^2/MA_x$

where M is the sum of the in-plane electron and hole effective masses.

Trial solutions of eqn. (4.9) reveal immediately that the observed sublinear behavior at low temperature in the CQW sample may not be explained by a particularly large value of Γ so that the $\tau\alpha\Gamma$ region of eqn. (4.9) persists to higher temperature before the onset of the more quickly varying $\tau\alpha kT$ region. This is indicated by the fact (illustrated in

fig. 4.13) that a tangent to the linear region of the curves, extrapolated back to zero lifetime, always intercepts the T axis at $T \leq 0$. It is not possible to generate a positive T intercept from eqn. (4.9) using any value of $\Gamma(T)$ since the calculated curves always asymptotically approach $\tau \alpha kT$ from above. Positive intercepts are obtained for both the coupled quantum well and for the 25Å and 40Å wells of [2.12], which indicates that some other effect not considered in eqn. (4.9) is influencing the PL lifetime. In fact, the positive intercept may be explained by modifying eqn (4.9) to include a homogeneous linewidth (and hence coherence area) associated with localisation. The total recombination rate at a given temperature, T, may be expressed as the sum of the rate for a localised exciton, $R_l(T)$, and a delocalised exciton, $R_d(T)$, weighted by the probability of localisation, $P_l(T)$, and delocalisation, $1-P_l(T)$, respectively.

$$\text{ie. } R_{total}(T)=R_l(T)P_l(T) + R_d(T)\{1-P_l(T)\} \quad \text{eqn. (4.10)}$$

The delocalised rate, $R_d(T)$, is given by the inverse of eqn. (4.9):

$$R_d(T)=KL\, f_o\, r_d(T)/\Gamma_d(T) \quad \text{eqn. (4.11)}$$

$$\text{with} \quad r_d(T)=1-\exp(-\Gamma_d(T)/kT)$$

In the case of the localised rate, the effective coherence area, A_{eff}, of the localised exciton is assumed to be given by the reciprocal sum of the localisation island

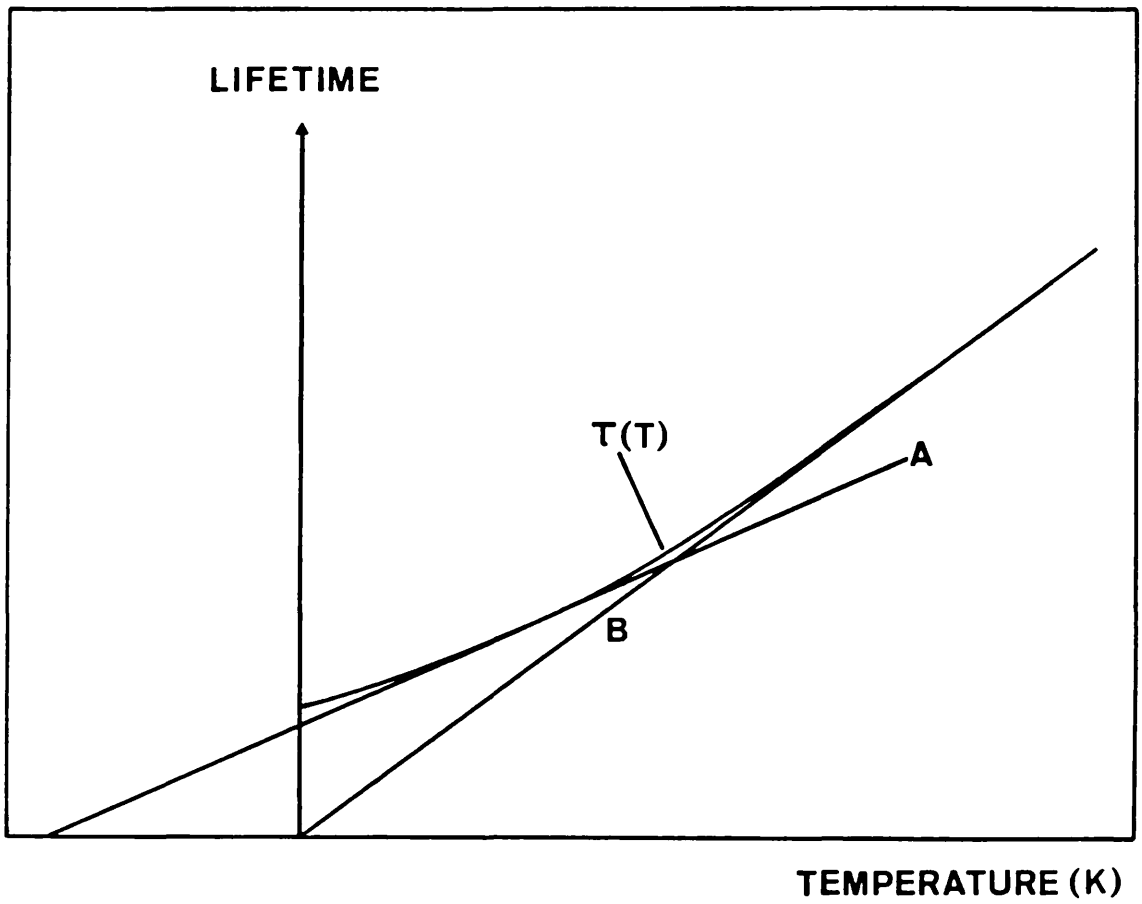


Figure 4.13 Using eqn. (4.9) (for delocalised excitons), any lines (eg. A and B) tangential to $\tau(T)$, always intercept the T axis at $T \leq 0$ when extrapolated back to $\tau=0$.

size, A_{loc}, and the coherence area determined by scattering, as in the delocalised case, A_c. In this way, A_{eff} is determined by the smaller of A_{loc} and A_c, as required.

$$\text{ie. } 1/A_{eff}=1/A_{loc}+1/A_c \qquad \text{eqn. (4.12)}$$

Since $A_c \alpha 1/\Gamma$, an effective linewidth associated with A_{eff} and A_{loc} may be defined, so that eqn. (4.12) implies: $\Gamma_{eff}=\Gamma_{loc}+\Gamma_l(T)$. By analogy with eqn. (4.10), $R_l(T)$ may then be expressed as:

$$R_l(T)=KL\ f_o\ 1/[\Gamma_{loc}+\Gamma_l(T)/r_l(T)] \qquad \text{eqn. (4.13)}$$

where the rate due to Γ_{loc} is independent of temperature, as expected for $A_{loc}<<A_c$, but:

$$r_l(T)=1-\exp(-\Gamma_{eff}(T)/kT)$$

In this way, eqns. (4.10)-(4.13) allow for different values of homogeneous linewidth (and hence r(T)) in the localised and delocalised regimes. Assuming $\Gamma=\alpha+\beta T$ (see section 2.4), at least some of the temperature independent component of the linewidth, α, may be attributed to scattering at alloy fluctuations, which in the localised case effectively becomes counted in the Γ_{loc} component. Consequently a lower value of α is expected in $\Gamma_l(T)$ than in $\Gamma_d(T)$. The same value of β is expected throughout, except if the localisation area size is such that a restriction becomes imposed on the maximum LA phonon wave vector allowed for LA phonon-exciton scattering [4.4]. In this calculation, a value of $\beta=5\mu eV/K$ is adopted, equal to that measured for the heavy hole exciton in a 113Å single quantum well, and in

the delocalised regime α=o.5meV is used [2.16].

$P_l(T)$ may be obtained by calculating the occupation probability for a 2D exciton density of states function including localisation, as indicated in fig. 4.14. The Stokes shift, E_S, between the PLE and PL peak energies is taken to indicate the energy mismatch between the localisation island and the surrounding well. The probability of finding an exciton in the localised region is then given by:

$$P_{loc} = \frac{D/N \int_0^{E_S} \exp(-E/kT)\, dE}{D/N \int_0^{\infty} \exp(-E/kT)\, dE + D \int_{E_S}^{\infty} \exp(-E/kT)\, dE}$$

$$= \frac{\exp-(E_S/kT)-1}{-1-N\exp-(E_S/kT)} \qquad \text{eqn. (4.14)}$$

where D is the value of the constant 2D density of states, and N=B/A, the ratio of the area of quantum well where excitons are only delocalised to the area in which localisation islands exist (see fig. 4.14). A Stokes shift of 3meV was measured in the CQW.

Using eqns. (4.10)-(4.14) and $\tau(T)=1/R_{total}$, it is possible to generate $\tau(T)$ curves of the shape observed in the 0-50K region. Physically what is required is effective

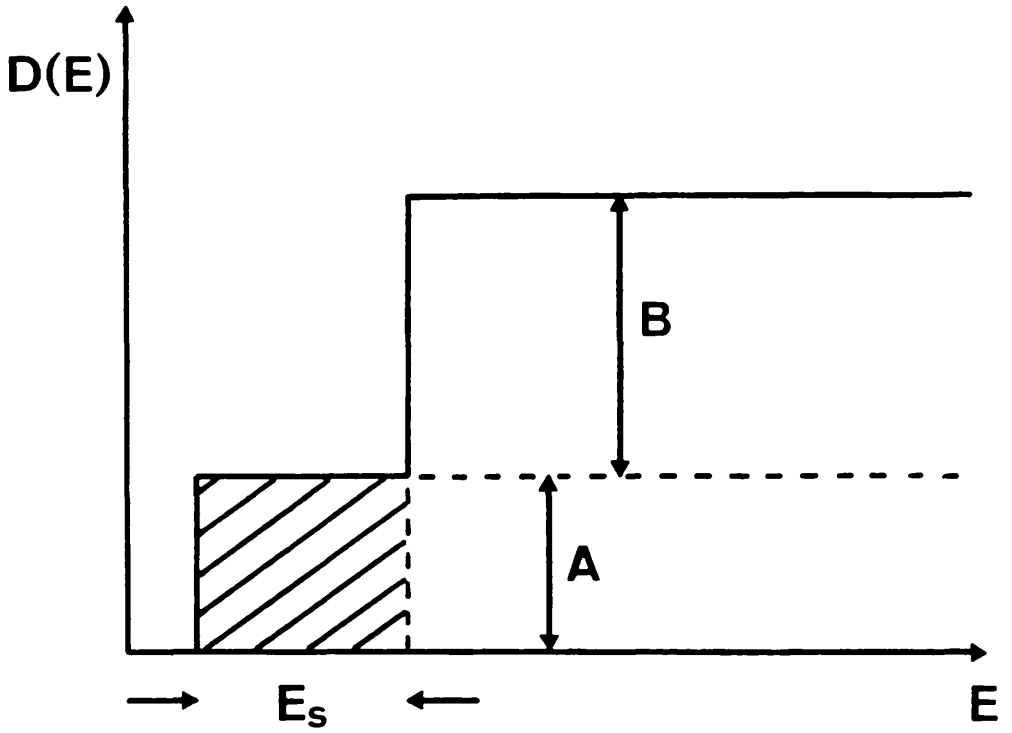


Figure 4.14 The method of calculating the localisation probability in a quantum well containing "islands" of wider well width. The figure shows the 2D exciton density of states, comprising a proportion of states corresponding to the area where no islands are present, and a proportion corresponding to the area where islands are present which extends to a lower energy given by the value of the Stokes shift. The probability of localisation is equal to the probability of an exciton being in the shaded region, equivalent to those extra energy states introduced by the localisation islands.

localisation linewidth which is substantially larger than the delocalised homogeneous linewidth. In this case as the localisation probability falls with increasing temperature, the reduction in lifetime caused by delocalisation compensates for the increase in the delocalisation linewidth with temperature either in the $\tau\alpha\Gamma_h$ or $\tau\alpha kT$ regimes. Ultimately, the lifetime must become proportional to kT for any values of Γ_l and Γ_d if the temperature is sufficiently high and a point of inflection should be observed in the $\tau(T)$ curve as it tends asymptotically towards $\tau\alpha kT$ from below. This point of inflection is not observed in the CQW data. However, by using accepted values of the various parameters it is possible to successfully fit the theory to the measured data and thereby show that this point of inflection lies beyond 60K.

The oscillator strength, f_o, connecting Bloch states in the conduction and valence bands may be calculated from GaAs quantum well absorption coefficient measurements away from the bandedge. Although a calculation of f_o could also be made from bulk GaAs values, a measurement from a quantum well is preferred in order to account for any change in f_o due to modification of the valence band structure between the bulk and the quantum well. The absorption coefficient per unit area per unit cell layer (α') in the continuum of a 2D system may be related to the effective oscillator strength (f') per unit area per unit layer of a 1s 2D exciton using the expressions of Shinada and Sugano [1.8]. By eliminating $|\langle u_c|p|u_v\rangle|^2$, α'becomes:

$$\alpha' = \frac{\varepsilon_r \pi a h f'}{4 m_o c n a} \quad E \qquad \text{eqn. (4.14)}$$

where a is the 2D 1s exciton radius. The factor E is the enhancement in absorption away from the bandedge due to unbound exciton correlation effects, given for a 2D system by:

$$E=\exp(\pi\alpha)/\cosh(\pi\alpha) \quad \text{with } \alpha=\sqrt{(R^*/\delta E)} \qquad \text{eqn. (4.15)}$$

where R^* is the effective Rydberg and δE is the excess photon energy above the bandedge.

Taking $\alpha=1.1\times10^6 m^{-1}$ in the 2D continuum of a 96Å quantum well at an energy 25meV above the bandedge [1.2]; $R^*=8$meV and $a_{2D}=130$Å, the values determined from the variational calculation and verified experimentally from the $\tau(E)/\tau(0)$ measurements; and taking the unit cell volume $\Omega=(5.6Å)^3$; a value of effective oscillator strength f_{eff} per unit cell per unit layer is obtained from eqns (4.10)-(4.13). In [2.12], f_{eff} and f_o are related by:

$$f_{eff}=\Omega/L_z \; f_o . \; |\varphi_{eh}(0)|^2 \qquad \text{eqn. (4.16)}$$

Setting $L_z=5.6$Å for a unit layer, a value of 0.802 is obtained for f_o.

The total exciton mass, M, is determined from the reduced in-plane effective mass value $\mu=0.046m_o$ used in the envelope function calculation of section ~~4.3,~~ 4.4.2 giving $M=0.213m_o$

assuming $m_e=0.067m_o$: similar to the values adopted by other workers. The current calculation is unusual in that the total exciton mass is rarely required in the calculation of exciton properties: the exciton binding energy or Stark shift for example only depend on μ. Consequently, the value of the in-plane effective hole mass which only weakly affects μ, but strongly affects M, is not well known. The calculation of $\tau(E)/\tau(0)$ showed that using $\mu=0.049m_o$ did not significantly affect the agreement with experiment. However, this value implies $M=0.250m_o$, indicating that adjustments of M within this range are justified if necessary to fit eqn. (4.10) to the measured lifetime variation with temperature. Finally, it should be noted that the A_x term was collected together with other constants by Feldmann et al. and replaced by the ideal 2D exciton binding energy. However, as demonstrated in section 4.5, the exciton is not perfectly two dimensional in this sample. Since it is the coherence area that is crucial here, the A_x term is included explicitly. Consequently, the calculation takes partial account of the fact that the exciton is not quite two dimensional.

Using the above values to evaluate the total recombination rate, for the zero field lifetime at 4.2K of 151ps, in the localised regime a value of $\Gamma_{eff}(T)=0.40$meV is predicted. The only unknown parameters in the fit are the percentage distribution of Γ_{eff} between Γ_{loc} and $\Gamma_l(T)/r_l(T)$ and the density of localisation islands, N, all other

parameters being determined from other measurements. If Γ_{loc} is neglected, $\Gamma_1(T)=0.071meV$ is obtained. This value is unreasonably small compared to the value of 0.5meV obtained by Schultheis et al. from phase coherence time measurements [2.16], indicating again that the value of Γ_{loc} must be significant. The best fit to the data is obtained by attributing the largest possible proportion of Γeff to Γ_{loc}: $\Gamma_{loc}=0.38$, $\Gamma_1(T)=0.02$. That is, by assuming that all the temperature independent component of the homogeneous linewidth, α, is included in Γ_{loc}, so that $\Gamma_1(T)=\beta T$ only. The best fit is obtained using N=1 for the ratio of localisation island area to pure delocalised area, so that (including all four interfaces) on average 50% of the sample area is occupied by localisation islands. The fitted data (curve A) is shown in figure 4.15 which also shows an improved fit (curve B) taking $M=0.250m_o$, as discussed previously. The fit is insensitive to the value of α chosen within the homogeneous linewidth expression in the delocalised regime since $\tau\alpha kT$ behavior starts to dominate in this region. Consequently, the assumed value of 0.5meV (from ref. [2.16]) introduces no significant error here. The low temperature value of Γ_{loc} may be used to calculate the value of the average radius of the localisation islands. Using $A_{loc}=L/\Gamma_{loc}$, an average localisation radius of 436Å is obtained. This value restricts LA phonon-exciton scattering only to phonon energies less than 2.8meV [4.4], so that such a restriction may be neglected at low temperature where the localisation probability is high since only a small number of phonons of energy greater than 2.8meV will be excited.

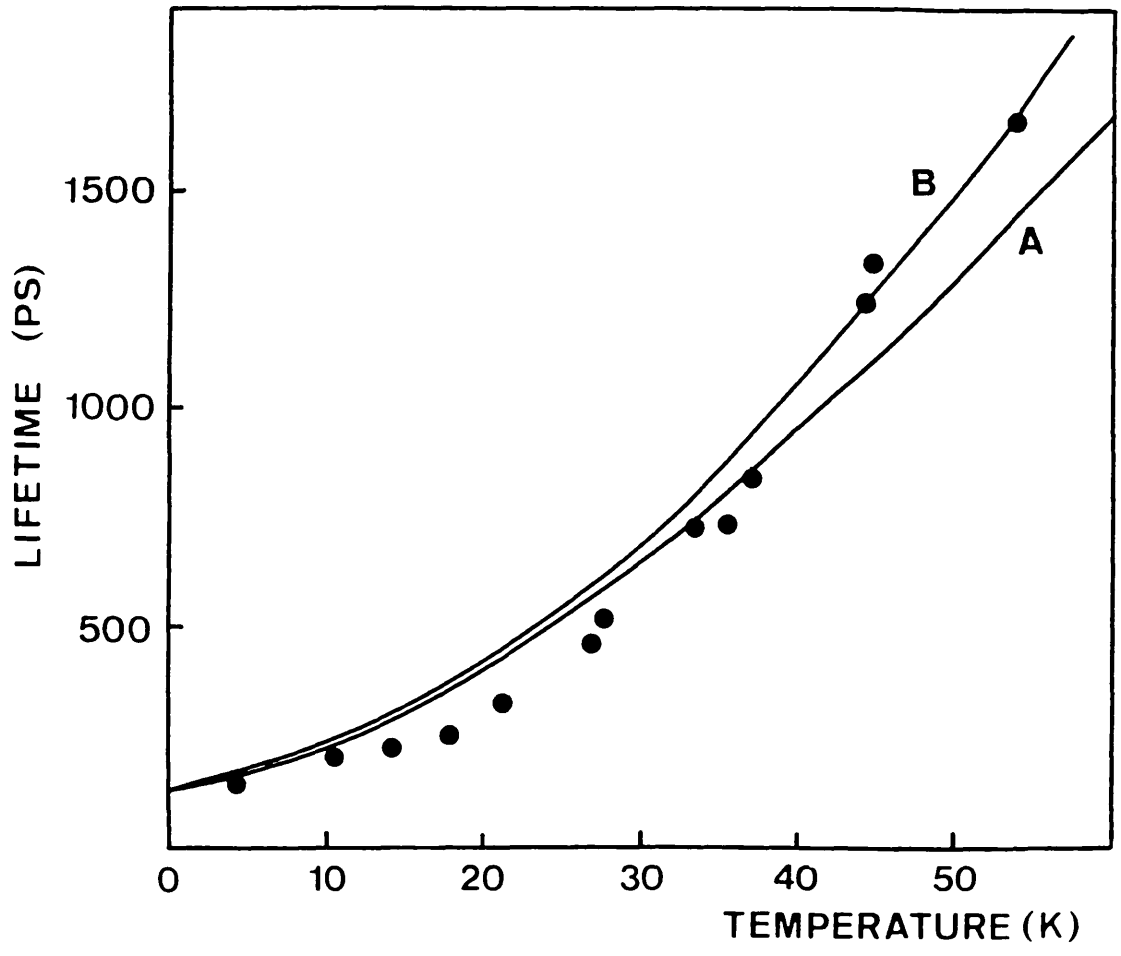


Figure 4.15 The measured variation of PL lifetime with temperature at zero field in the CQW. Curve A is the theoretical fit using $M=0.213m_o$. Curve B is the fit using $M=0.250m_o$.

Consequently, the use of the same value of the coefficient for the increase in homogeneous linewidth with temperature due to LA phonons (β) in both the localised and delocalised regimes, is shown to be correct.

4.6 Conclusions

A study has been made of the variation of PL lifetime with perpendicular electric field in a coupled quantum well. Lifetime enhancements with field a factor of 3 greater than expected for a single quantum well of the same overall width have been observed, consistent with the larger Stark shifts observed in previous studies and demonstrating that the behavior of the coupled quantum well system is well understood. Close agreement has been obtained for the first time in a quantum well between the measured lifetime enhancement with field and a theoretical variational calculation within the effective mass approximation (ie. excluding valence subband mixing) for fields up to 70kV/cm. The validity of the simple variational approach using a 2D separable exciton wavefunction is therefore confirmed in this system. The lifetime enhancement was found to be independent of temperature between 4.2K and 27K, indicating that the exciton wavefunction is not strongly affected by localisation, and confirming the validity of the assumption of separating the centre of mass and relative electron-hole motion. The variation of lifetime with temperature has been measured between 4.2K and 52K and the dependence has been explained in terms of coherence volume arguments including

localisation at monolayer well width fluctuations. A quantitative fit to the data has been obtained for the first time from this theory with all but two parameters obtained from experimental measurements, allowing the average localisation area to be determined.

CHAPTER 5 TIME RESOLVED PHOTOLUMINESCENCE STUDIES IN QUANTUM WELLS CONTAINING A SIGNIFICANT FREE CARRIER DENSITY

5.1 Introduction

In this chapter, TRPL measurements are described on a quantum well structure consisting of a number of single quantum wells with "leaky" barriers and trapping times such that a significant population of free carriers is injected into the wells on the application of an electric field. This work is in contrast to the results presented in chapter 4, where the coupled quantum well could be considered perfectly isolated from the surrounding structure. The current study demonstrates the way in which free carrier trapping and perpendicular transport can modify the ideal TRPL behavior in quantum wells and investigates the extent to which infomation about these effects may be extracted from the measured lifetime data. Few studies of these types of effects in TRPL currently exist in the literature. Matsusue and Sakaki [2.2] have measured the PL lifetime as a function of temperature from 4.2K to 300K at zero field in a modulation doped multiquantum well with a doped degenerate free electron population of constant density $1x10^{12}$ cm^{-2}, and showed that the measured lifetime could be modelled quantitatively from the variation in the Fermi-Dirac and Maxwell-Boltzmann distributions for the degenerate electrons and non-degenerate hole populations respectively. As discussed in

section 2.2, at low temperatures when the electron population is degenerate, the lifetime is independent of the majority free carrier density since all states for recombination are filled (fig. 5.1). For the same reason, the lifetime is also independent of temperature as long as the free carriers remain degenerate. As the temperature is increased, the electron population eventually becomes non-degenerate and the lifetime becomes proportional to temperature and to the inverse of the majority free carrier density. Very recently a conference report [5.1] has appeared describing measurements at 1.8K of the variation in PL lifetime as a function of electron density injected into a single quantum well by a perpendicular electric field. In this case, a fall in PL lifetime with increasing carrier density was observed, but by an analysis of the accompanied fall in PL efficiency, it was claimed that the radiative lifetime was in fact rising. However, no complementary analysis of the lifetime enhancement as a function of field was presented, so it is not possible to determine whether the increase in the radiative lifetime was due to the usual field induced electron-hole separation or to any lifetime increase inherent to the presence of the free electron density, eg. screening of the excitonic Coulomb interaction. In this work, similar PL measurements are made in 100Å and 200Å single quantum wells as a function of electric field injected free carrier density for both electrons and holes and correlated with the lifetime variation as a function of temperature to obtain a unified picture of the observed behavior. In addition, the lifetime measurements have been

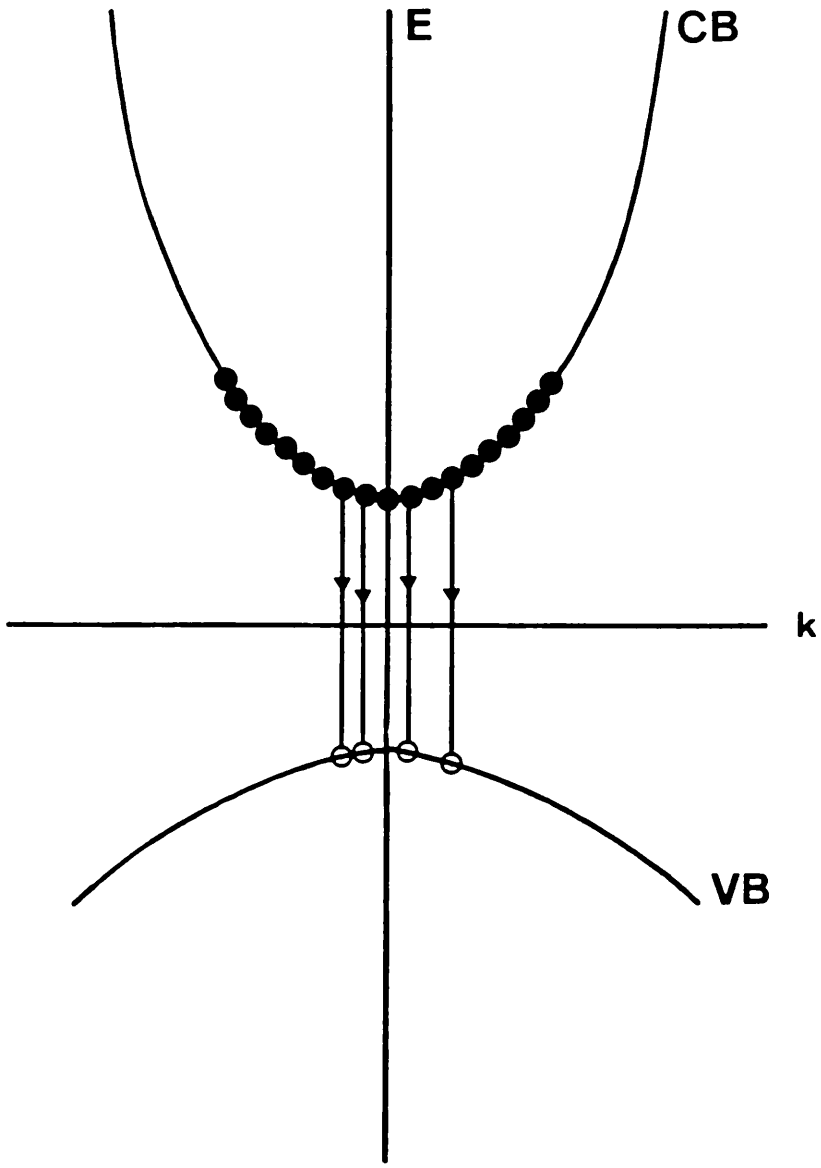


Figure 5.1 Schematic E(k) diagram illustrating the occupancy of states for a degenerate electron gas and photocreated non-degenerate holes. Every hole state has an electron available for recombination in a momentum conserving (vertical) transition. The recombination probability is then unaffected by further increases in the degenerate electron density.

used to complement Hanle photoluminescence measurements performed by other workers to determine the effective g-factor for electrons as a function of quantum well width in this sample.

5.2 Description of the Sample and Discussion of the CW PLE data

The sample used in this work is shown schematically in fig. 5.2, and consisted of 4 single quantum wells of widths 50Å, 100Å, 200Å and 800Å grown on an undoped 0.5 μm GaAs buffer layer and an n+ GaAs (100) substrate. The sample was contacted using the same ITO Schottky barrier technique described in chapter 4, the diameter of the contact being 2 mm in this case. The sample has been studied extensively in CW PL, PLE and Hanle PL by other workers [5.2] and the initial motivation of the work was to determine the radiative lifetime in each of the wells as a function of applied field to complement the Hanle photoluminescence studies in order to determine the g-factor for electrons as a function of well width. This work is described in section 5.5. The sample was unusual in that upon the application of a perpendicular electric field, a degenerate free carrier density was observed in the 100Å and 200Å wells. The presence of the degenerate free carriers was indicated by complementary PL and PLE measurements [5.2] which showed a variation in the "Stokes shift" (the difference between the PL and PLE peak positions) with applied bias due to a Moss-Burstein shift in the PLE peak position to higher energy due

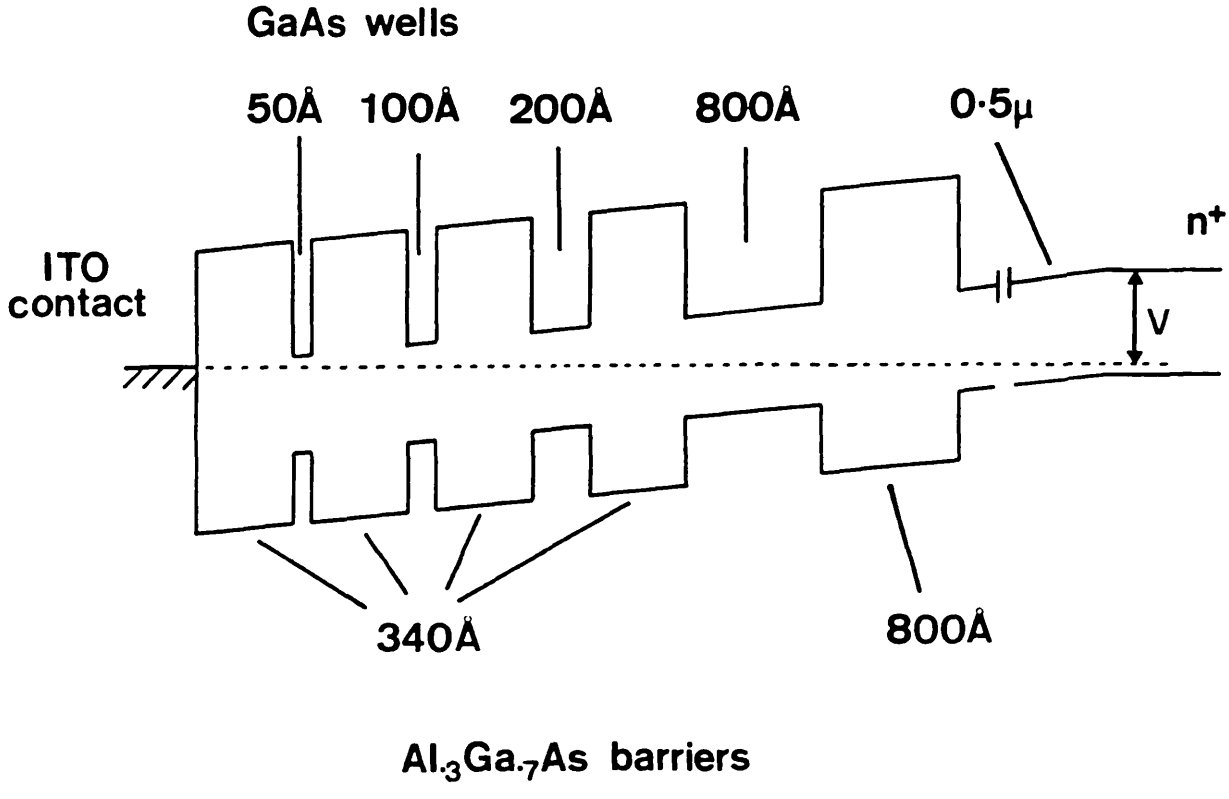


Figure 5.2 Diagram of the quantum well structure used in the work described in this chapter.

to blocking of the states at the bottom of the band by the free carriers. Assuming parabolic bands, if all hole k-states are filled up to a quasi Fermi level E_f, the Moss-Burstein shift, E_{mb} , is given by:

$$E_{mb} = E_f \ (1+m_{exy}/m_{hxy}) \qquad \text{eqn. (5.1)}$$

For two dimensional degenerate carriers of effective mass, m^*, the density of degenerate carriers, N, is given by the product of the two dimensional density of states and the quasi Fermi level, E_f:

$$\text{ie.} \qquad N = \frac{dN}{dE} E_f = \frac{m^*}{\pi\hbar^2} E_f \qquad \text{eqn. (5.2)}$$

Using eqns. (5.1) and (5.2), N may be calculated from the measured Moss-Burstein shift. The values for in-plane effective mass adopted in this work are those used successfully in the envelope function calculations of chapter 4: $m_{exy}=0.067m_o$ and $m_{hxy}=0.146m_o$. Figure 5.3 illustrates a typical Stokes shift curve, (of similar form for all wells), showing the increase in Stokes shift with field up to a maximum value, after which the shift reduces as the carriers are swept out of the well by very high field. The maximum Stokes shifts corresponded to peak free carrier densities of $1x10^{11}$ cm^{-2} for both electrons and holes. These values imply (from eqn.(5.2)) that the condition for degenerate free carriers $E_f \geq 4kT$ [1.6] is indeed satisfied at 4.2K, the cross over temperature between degenerate and non-degenerate statistics, $T=E_f/k$, occuring at 45K and 21K for electrons and holes

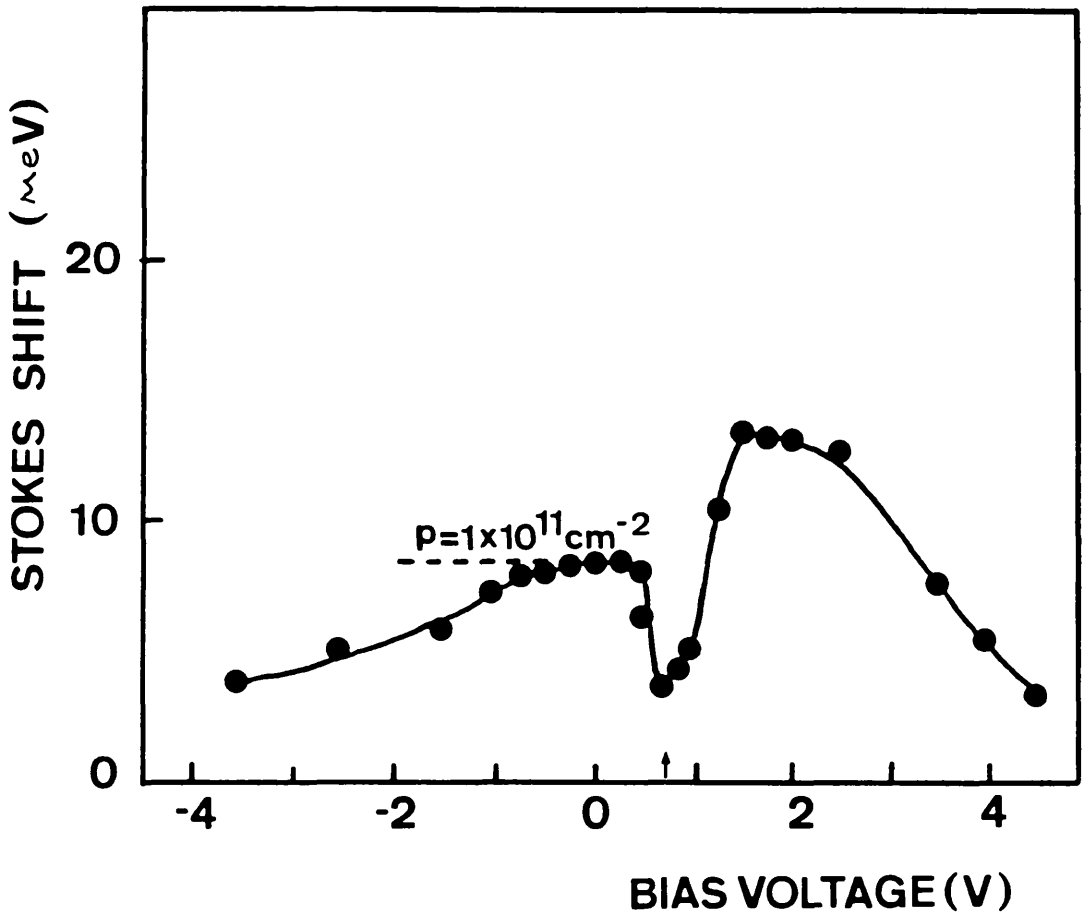


Figure 5.3 Stokes shift vs. Bias voltage for the 50Å well at 4.2K [5.2]. The arrow indicates the bias voltage at which the net field across the well is zero. For positive bias with respect to this value, the well fills with electrons and for negative bias the well fills with holes: thereby generating the increased Stokes shifts, as indicated.

respectively. The details of the mechanism for the capture of the free carriers are unknown, but it is presumed to be due to some impurity assisted tunnelling process in the AlGaAs barriers which allows perpendicular transport of the carriers through the structure. Carriers may then become trapped within the GaAs wells and a large free carrier density may be established in steady state if the trapping and de-trapping times lie within a certain regime. The barriers are too wide for significant quantum tunnelling to occur at the fields in question, and the temperature is too low for thermally activated transport over the barriers.

The peak free carrier density is such that at least two extra carriers would be present per "intrinsic" (ie. in the absence of free carriers) exciton volume. In this case, the Coulomb potentials due to the free carriers could be expected to screen out the exciton interaction. However, PLE spectra from the wells indicate the presence of clear exciton-like resonances (fig. 5.4). This is in agreement with other PLE studies of quantum wells in the presence of similar free carrier densities [5.3], and indicates the presence of significant electron-hole correlation even in the presence of a large free carrier density. It has been shown theoretically [5.4] that Coulomb screening is much less effective in two dimensions than in three. In 3D, the screening of a Coulomb potential by a free charge density generates an effective potential of the form:

$$\varphi(r) = \frac{e^2}{4\pi\varepsilon_o\varepsilon_r r} \exp(-r/\Omega_d) \qquad \text{eqn. (5.3)}$$

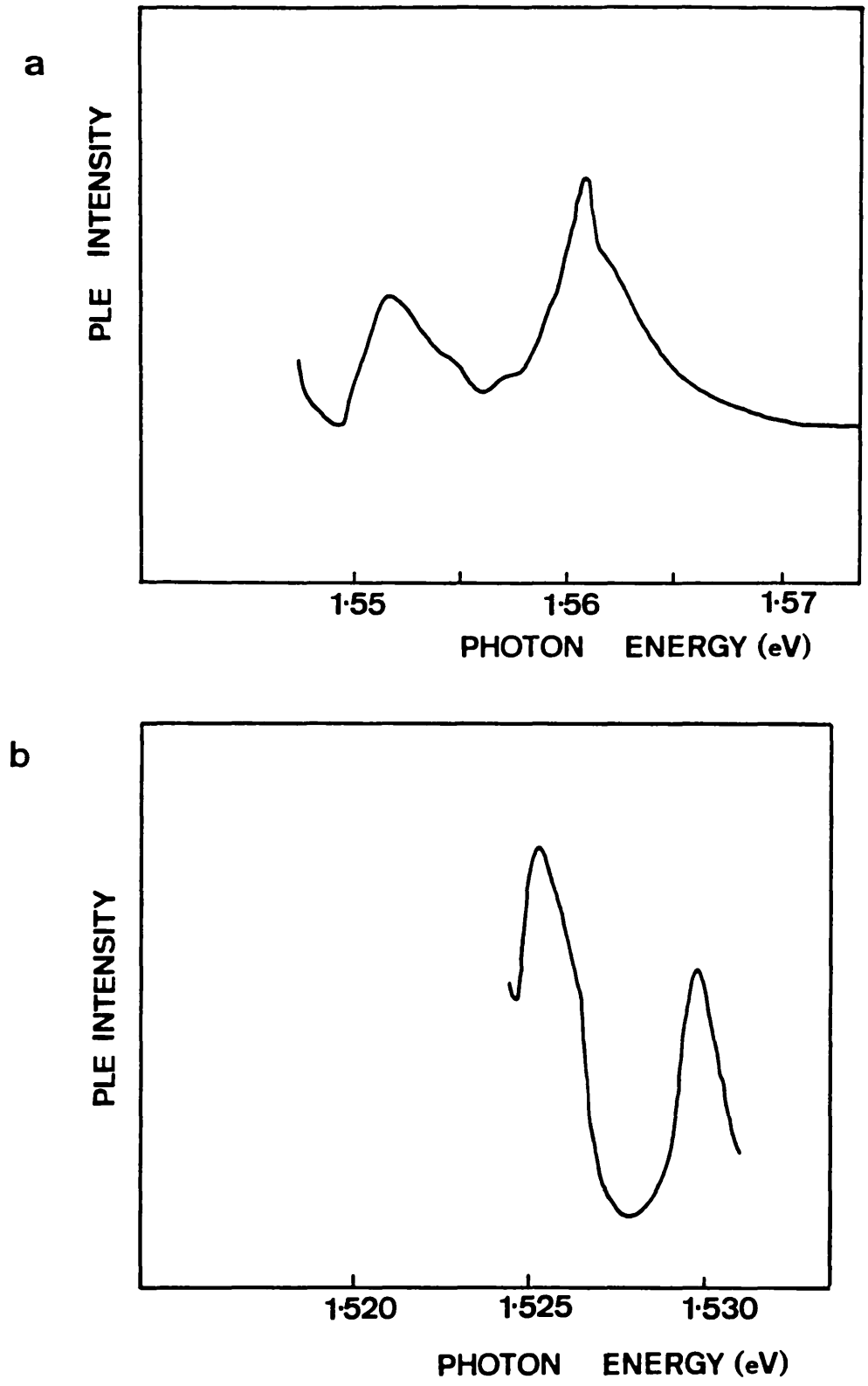


Figure 5.4 PLE Spectra from (a) the 100Å well, (b) the 200Å well, indicating clear n=1 light and heavy hole "exciton" peaks. Both spectra were taken at a zero bias, ie. close to the maximum value of injected hole density [5.2].

where $\cap_d$ is the screening length. The problem of screening in a 2D multi-layer system has been treated by Fetter [5.5], who shows that at long distance the screened potential adopts the same Yukawa form of eqn. (5.3). However, $\cap_d$ becomes [5.5]:

$$\cap_d = \sqrt{(\varepsilon_o L_b h^2/8m^* e^2)} \qquad \text{eqn. (5.4)}$$

where m^* is the majority free carrier effective mass and L_b is the barrier thickness between the layers. In the current sample, for free hole screening and a barrier thickness of 340Å, this implies a screening length of 47Å, around 70% of the charge density radius (a/2) of a 2D exciton in a quantum well. However, the effect of free carrier screening on the exciton binding energy in a quantum well has been treated theoretically by Kleinmann [5.6], who showed that the binding energy in the presence of free holes at $1x10^{11}$ cm^{-2} is reduced by a factor of 200 over the intrinsic value, and that the exciton oscillator strength for a perfectly coherent exciton ($\alpha 1/a^2$) is reduced by a factor of 10. This reduction in oscillator strength greatly exceeds that evident from an estimation of the variation in the integrated PLE exciton peak area with bias in the current sample, which suggests an oscillator strength of similar order to the intrinsic value. If the theory of Kleinmann is correct, the clear PLE peaks imply that single particle exciton binding must be replaced by a many body correlation, whereby the electron is correlated with many nearby holes. In this case, a clear PLE peak may be observed

even though the single particle exciton binding energy is effectively zero. Such a mechanism has been proposed by Saker et al. [5.3] to explain the clear PLE peaks observed in InP-InGaAs quantum wells in the presence of degenerate electrons.

5.3 The PL Lifetime measurements as a function of Bias Voltage and Temperature

The experimental procedures in this TRPL study were identical to those described in chapter 4. Figure 5.5 shows the measured Stark shifts as a function of applied bias in the 100Å and 200Å wells. Zero field in the 100Å well corresponded to a bias of +1.0 V, determined from the minimum Stark shift in the 100Å well as shown in fig. 5.5. The minimum Stark shift in the 200Å well occured at a lower applied bias (≈0.8V) and at some values of bias the Stark shift in the 100Å well exceeded that of the 200Å well, indicating substantial field non-uniformity through the sample. Following the approach of chapter 4, the field across a given well may be determined accurately from the measured Stark shift where quantitative measurement is required. This study concentrates on the lifetime variation in reverse bias (voltage negative with respect to the zero field voltage, degenerate free holes injected into the wells), where (unlike forward bias) the PL efficiency was found to be constant over a substantial portion of the field regime and quantitative calculations are therefore possible. The same qualitative variation in lifetime is however

The assignment of the shift in luminescence line position to a Quantum Confined Stark shift is made uncertain in this sample by the possibility of bandgap renormalisation (BGR) due to correlation within the injected hole sea. Delalande et al. (Solid State Comm. 59 (1986) 613)) have observed renormalisation shifts to lower energy of ≈10meV for an electron density of $1x10^{11}cm^{-2}$ in a 150Å modulation doped quantum well, and have shown this result to be in close agreement with the BGR predicted by several theoretical treatments. The values of free carrier density and PL line shift quoted above are comparable to those measured in the current sample (except for very large applied bias in the 200Å well). Consequently, some, if not all, of the "Stark shift" observed in the data of fig. 5.5 may be alternatively attributed to BGR, so that the (correspondingly reduced) electric field across the wells may no longer be inferred directly from the measured shift in PL line position in the field regimes where the Stokes shift indicates a significant carrier concentration in the wells. The "Stark shift" axes of figs. 5.8 and 5.9 should therefore be strictly considered only as "PL line shifts", and the significance of any consistency between the lifetime enhancement calculation and the observed variation in lifetime is reduced. The increase in PL lifetime in the 100Å well beyond a shift of 4meV may also be (either wholly or in part) due the reduction of the free carrier density at larger reverse bias. However, the main conclusions of this work, namely that: (a) a reduction in PL lifetime may be observed on the introduction of degenerate free carriers into a quantum well; and (b) the transition from excitonic recombination to degenerate free carrier recombination may be observed in the temperature dependence of the PL lifetime; are unaffected by the presence of bandgap renormalisation.

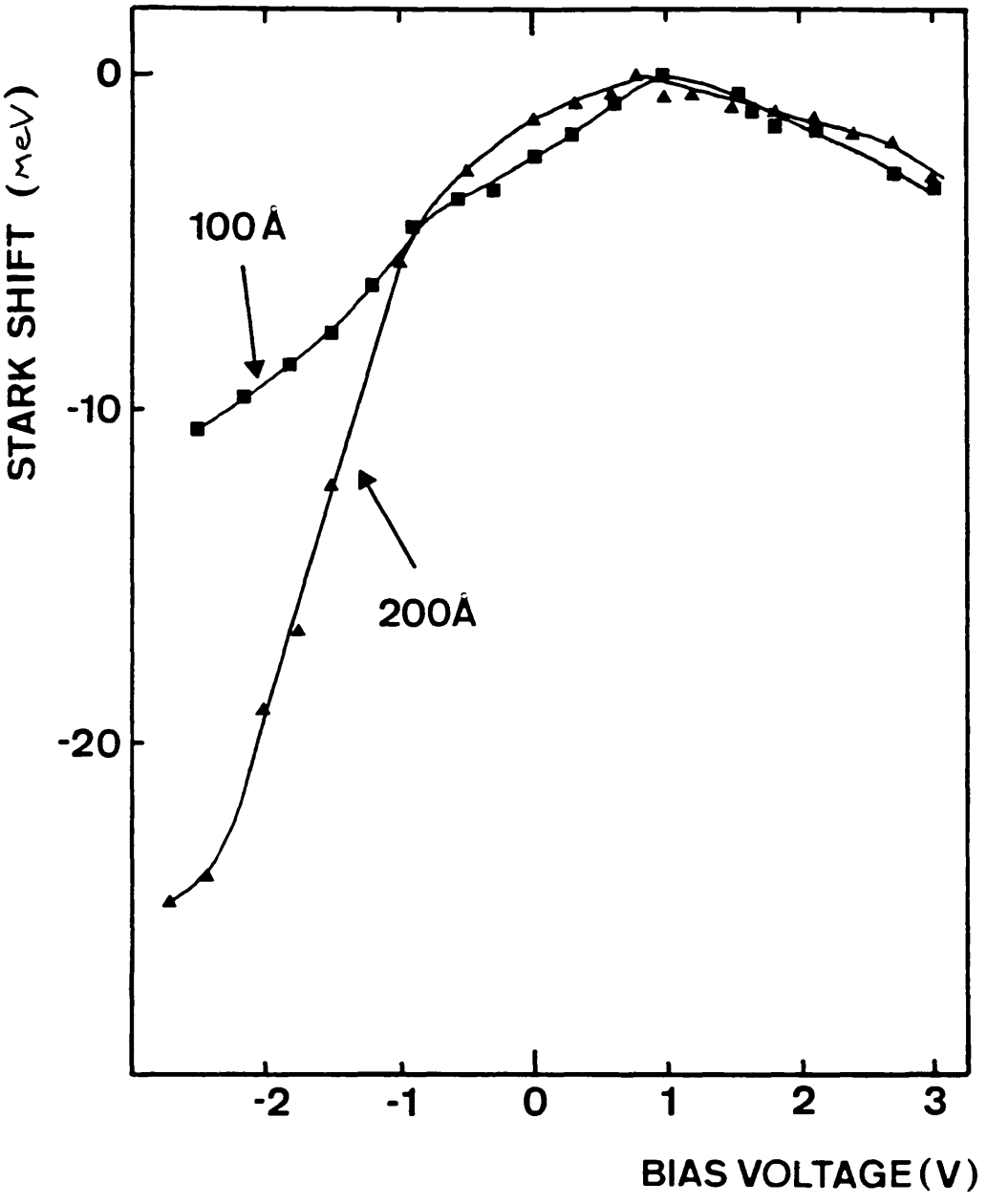


Figure 5.5 Stark shift vs. Bias voltage for the 100Å and 200Å wells at 4.2K.

observed for forward bias.

Figures 5.6 and 5.7 show the variation of PL lifetime and PL efficiency with applied bias in the 100Å and 200Å wells respectively. A reduction in the PL lifetime was observed for both polarities, inconsistent with the lifetime enhancement with field expected from electron-hole separation as described in chapter 4. In reverse bias, the integrated PL efficiency remained constant in the 200Å well up to -2.5V. In the 100Å well, the PL efficiency was constant until -0.5V but fell slightly after that. Both wells showed an immediate reduction in PL efficiency for forward bias. The constant PL efficiency in reverse bias over the regime where the lifetime decreases demonstrates that the reduction in PL lifetime must be due to the effect of the free carriers and cannot be attributed to an enhanced non-radiative rate. Indeed, an increase in lifetime was observed at higher reverse bias, presumably due to the usual lifetime enhancement with field associated with the QCSE.

Figure 5.4 and 5.5 show the measured variation in PL lifetime vs. Stark shift for the 100Å and 200Å wells respectively, and also the lifetime enhancement from the zero field value expected for free carriers assuming no variation in PL efficiency and using the calculation method described in chapter 4. In each case, the calculated enhancement in lifetime is small over the regime of Stark shift where the lifetime reduction is observed. In the case of the 100Å well, the increase in lifetime measured for

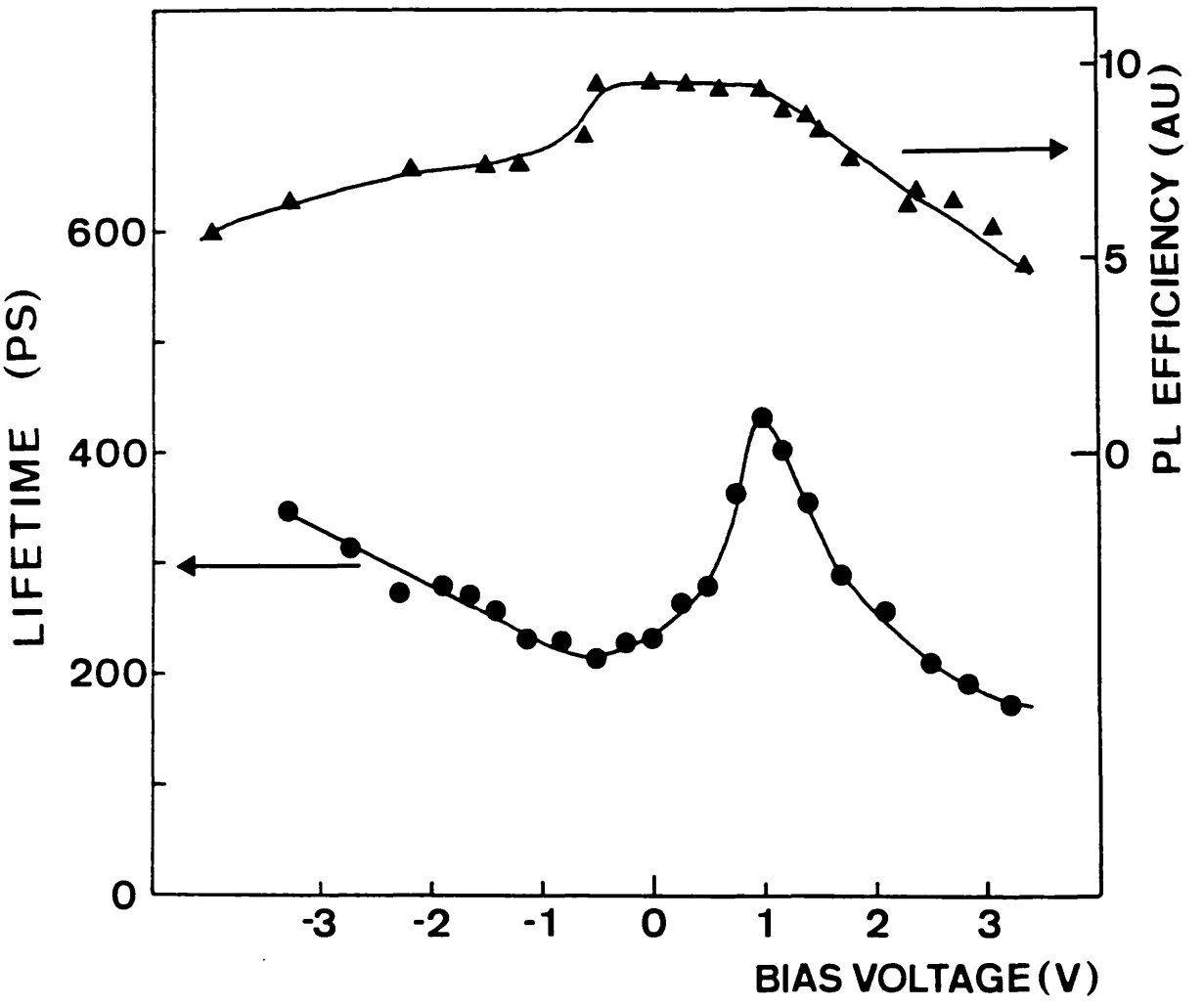


Figure 5.6 PL lifetime and PL efficiency vs. Bias voltage for the 100Å well at 4.2K.

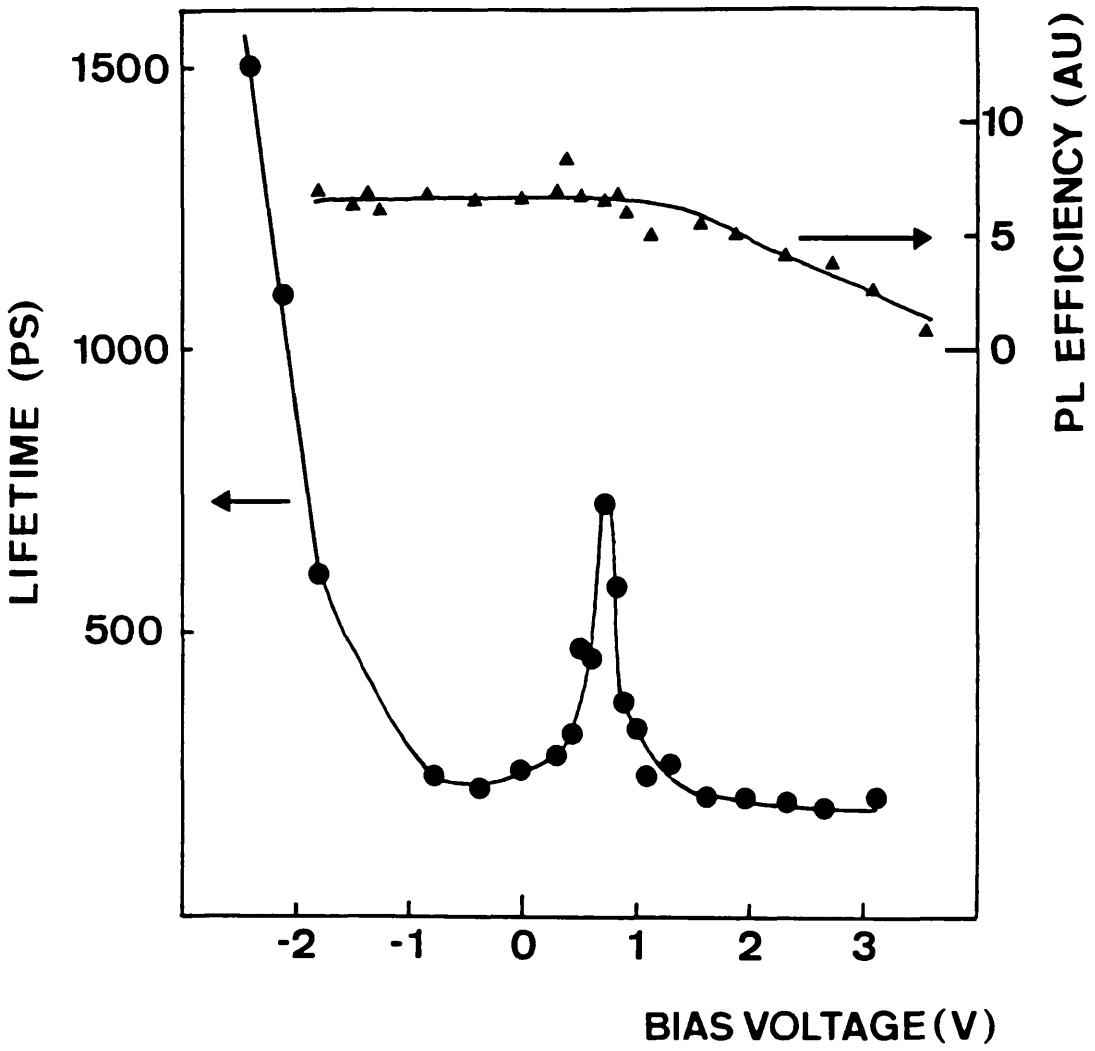


Figure 5.7 PL lifetime and PL efficiency vs. Bias voltage for the 200Å well at 4.2K.

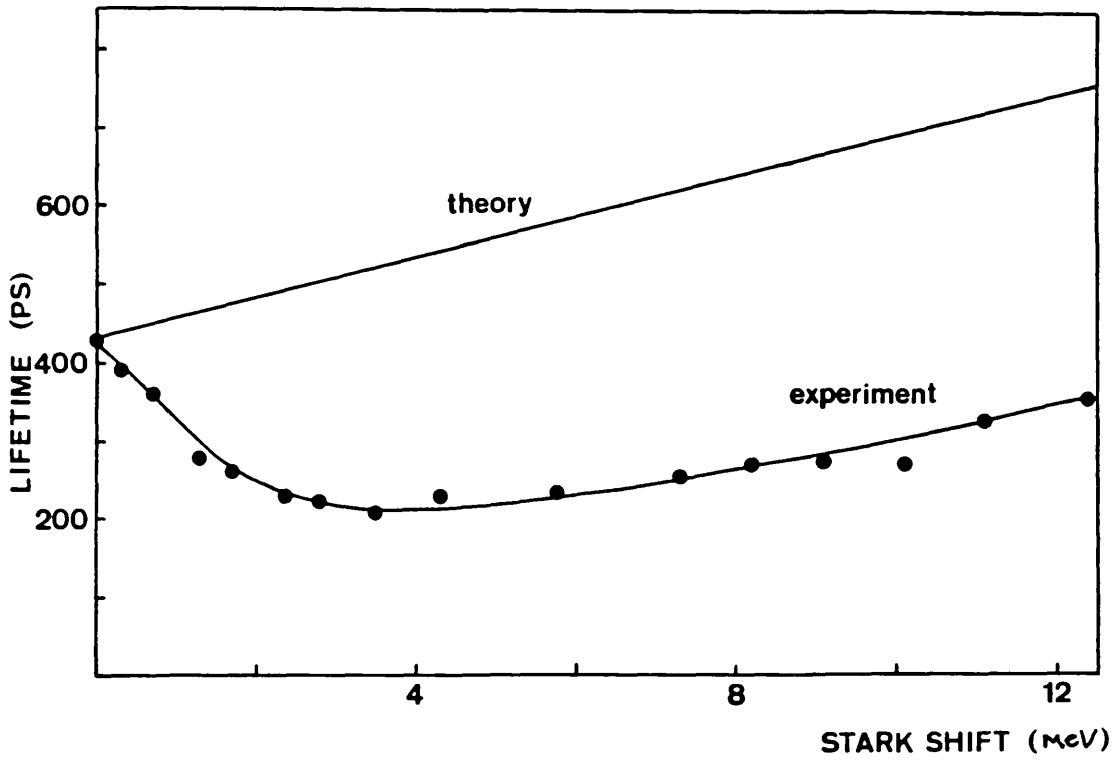


Figure 5.8 PL lifetime vs. Stark shift for the 100Å well at 4.2K.

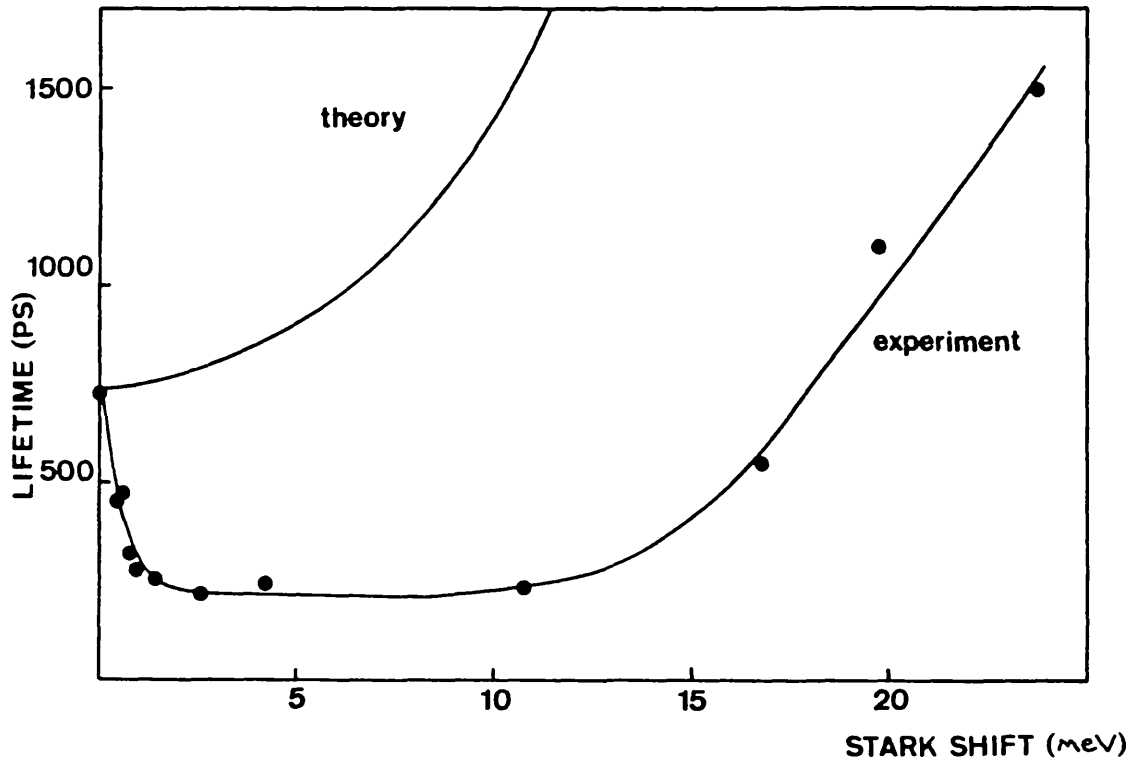


Figure 5.9 PL lifetime vs. Stark shift for the 200Å well at 4.2K.

higher values of Stark shift is similar to that expected from calculation. In the 200Å well, a large increase in the lifetime is observed for large reverse bias, consistent with the trapped free carrier density eventually leaving the well (as indicated by the Stokes shift measurements) and the lifetime returning to the large enhanced value determined by the variation in the intrinsic exciton envelope functions. However, the calculated enhancement is too large compared to that observed, which implies a substantially larger reduction in lifetime due to free carrier effects in the 200Å well compared to the 100Å well since the minimum lifetimes are similar. This discrepancy may be attributed to the effect of the 800Å well which becomes coincident in energy with the 200Å well for negative values of bias voltage. In this case, it is impossible to determine from which well the PL originates and the discrepancy with theory suggests that it is the 800Å well that is in fact being measured for large reverse bias. The initial reduction in PL lifetime however remains unambiguously attributed to the 200Å well because this effect occurs while the 200Å and 800Å well peaks are still well separated.

The validity of the explanation of the lifetime data in terms of free carrier effects is reinforced by a study of the PL lifetime in the 100Å well as a function of temperature at different fields in reverse bias, ie. at different values of free hole density (fig. 5.10). The small amount of data available for the 200Å well confirms the same trend. The expected increase in lifetime with

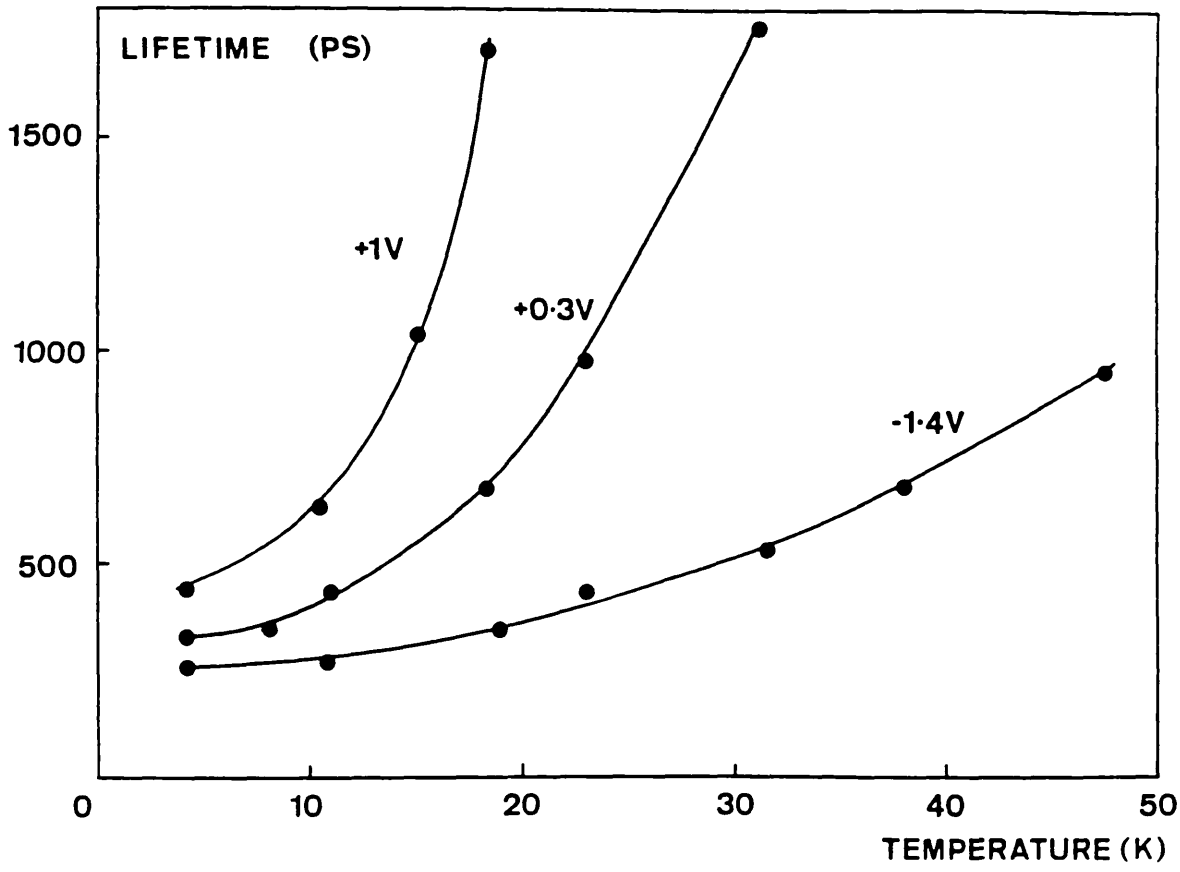


Figure 5.10 PL lifetime vs. Temperature for the 100Å well at different bias voltages.

temperature is observed in each case, however the rate of increase is reduced for finite fields compared to the zero field behavior. This is illustated more clearly in fig. 5.11, which shows the variation of "temperature lifetime enhancement factor" [defined as $\tau(T)/\tau(4.2)$] with temperature, T. The reduced enhancement with increasing bias is consistent with the lifetime being determined by a degenerate free hole population, in contrast to zero field, where $\tau(T)$ is determined by the coherence area effects outlined in section 2.4 and 4.5. At low temperatures (<20K) when the hole population becomes degenerate at the top of the valence band, the lifetime is expected to become temperature independent since all available hole k-states for electron recombination are filled. This trend toward weaker temperature dependence at larger reverse bias is indeed observed. As the temperature increases, the hole population becomes less degenerate and the radiative lifetime increases with a gradient proportional to the inverse of the hole density.

5.4 Explanation of the observed reduction in PL Lifetime with increasing free carrier density

Is a reduction in radiative lifetime due to the introduction of a large free carrier density into a quantum well reasonable? The peak free hole density corresponds to ≈2 free holes per intrinsic 2D exciton area (assuming 130Å for the 2D exciton radius). However, the holes must be in the correct k-states for recombination to be allowed. As

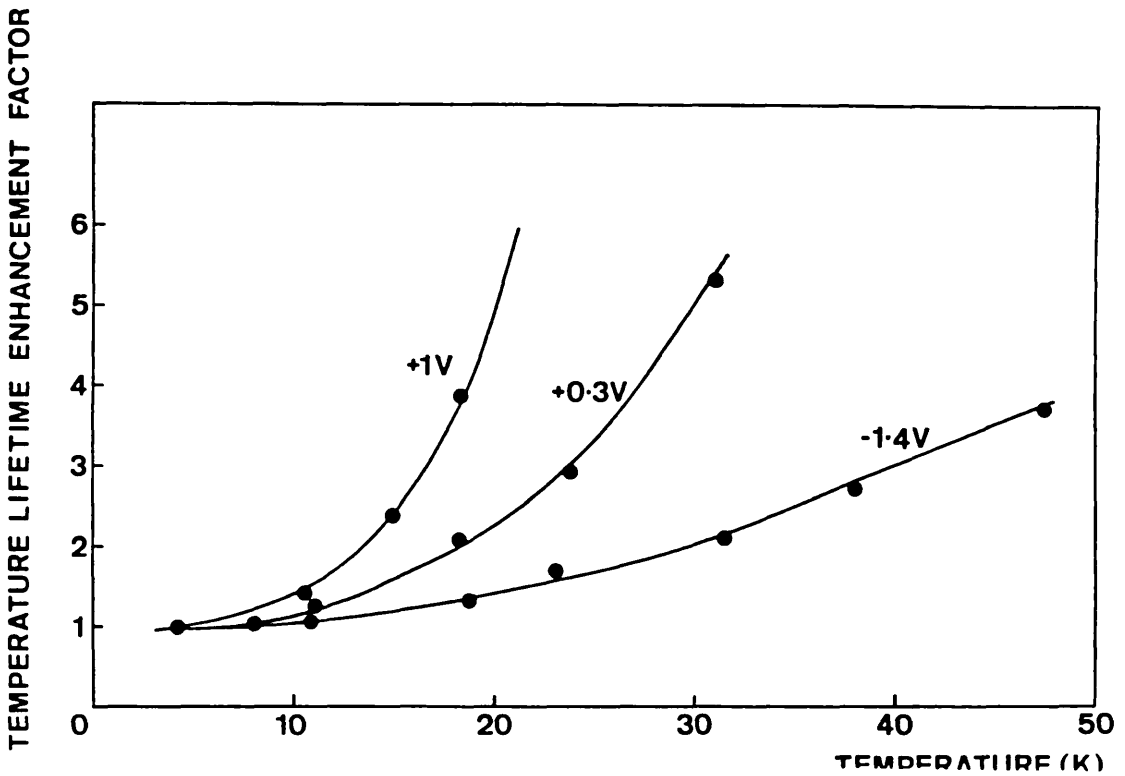


Figure 5.11 "Temperature lifetime enhancement factor", $\tau(T)/\tau(4.2)$, vs. Temperature for the 100Å well.

discussed in section 2.2 and illustrated in fig. 5.1, in the presence of degenerate free carriers, the radiative lifetime of a photocreated electron-hole pair tends to a constant value independent of free carrier density, temperature or whether the degenerate free carriers are electrons or holes. In this regime, Matsusue and Sakaki [2.2] calculated a radiative lifetime of 560ps for majority degenerate free carrier recombination in a Gallium Arsenide quantum well using k.p theory, assuming spherical bands and neglecting any electron-hole correlation. This calculated value was in reasonable agreement with their measured lifetime of 440ps at 10K in a 96Å multi-quantum well modulation doped to achieve a free electron density of 10^{12} cm^{-2} (fig 5.12b). No exciton resonance was observed at the bandedge in PLE (fig. 5.12a), so it may be assumed that any electron-hole correlation was screened out in this case. Some residual correlation short of true binding may explain the smaller measured lifetime in comparison to the calculated value.

Since the calculated radiative lifetime in the degenerate limit is independent of degenerate free carrier density or degenerate carrier type, it may be equally applied to the current case of degenerate free holes at a density of $1x10^{11}$ cm^{-2} at 4.2K. The value of 560ps from [2.2] is however insufficiently short to explain the observed reduction in lifetime in the current sample. However, the calculation neglects any electron-hole correlation which is clearly substantial in this instance since clear exciton resonances are observed in PLE. Such correlation would enhance the

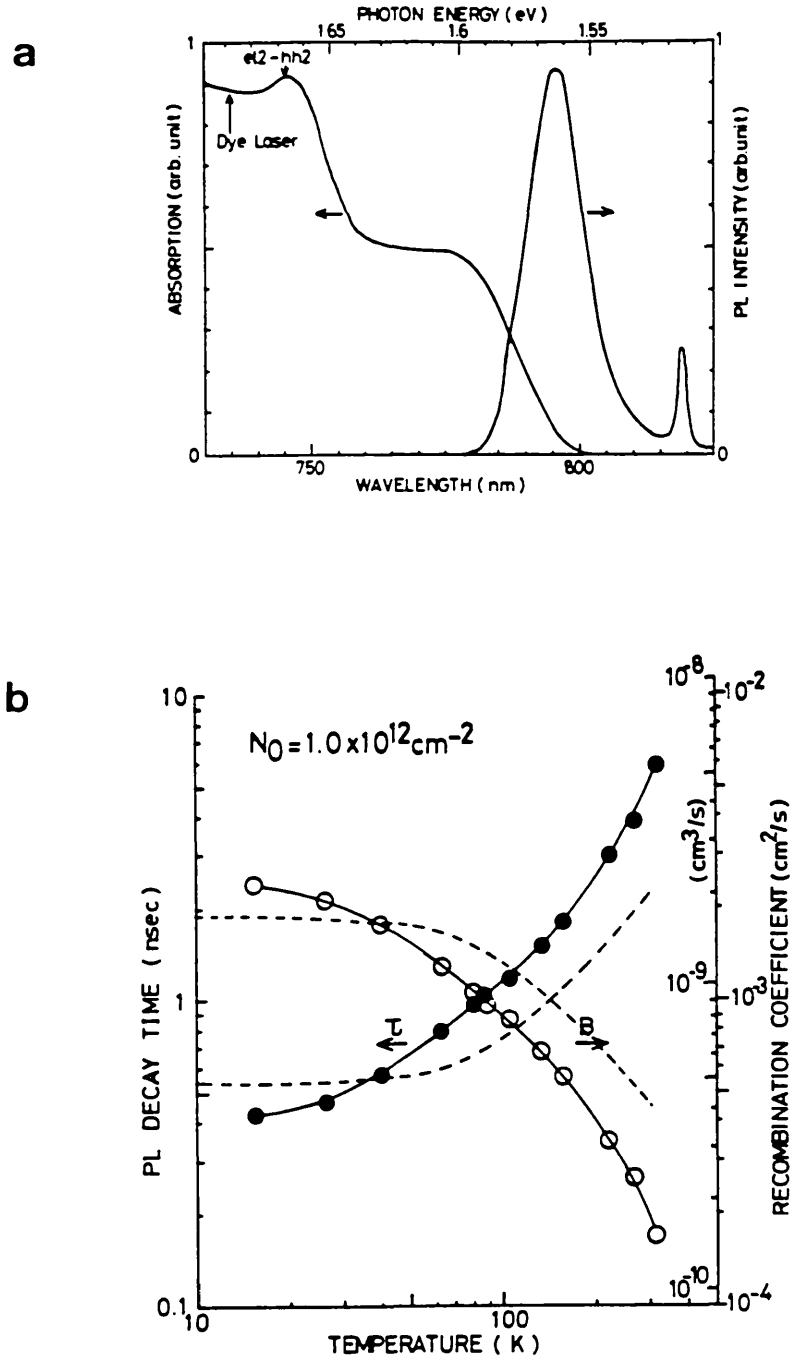


Figure 5.12 a) PLE spectrum from the modulation doped 96Å well containing $1x10^{12}$ electrons/cm^2 investigated by Matsusue and Sakaki [2.2]. b) Variation of PL lifetime with temperature (dots) measured in the above sample. The dashed line indicates the theoretical fit. The predicted lifetime tends to a constant value of 560ps at low temperature when the electrons become degenerate.

probability of finding an electron and hole in the same unit cell, and increase the radiative recombination rate. In this way, a lifetime shorter than 560ps would be expected, and an electric field dependence of radiative lifetime qualitatively similar to that observed could be obtained.

The expected lifetime including correlation may be calculated most simply by treating the recombination rate due to the free hole population and due to electron-hole correlation as separate processes, so that the total rate is the sum of the two. The maximum contribution due to electron-hole correlation may be assumed to be given by the intrinsic exciton lifetime (assuming for the moment that the same coherence area effects pertain). The lifetime enhancement factor calculations (fig. 5.8 and 5.9) show that the intrinsic exciton lifetime would not be strongly enhanced over the zero field value in the field regime where the free carriers enter the wells, so the zero field lifetimes may be adopted here. Lifetimes of this order may be added to the calculated value of 560ps for no e-h correlation by the reciprocal sum rule of eqn. (2.8) to generate clear reductions in PL lifetime with field as observed. In the case where all the electron-hole correlation is maintained, this simple model predicts lifetimes of 246ps and 311ps for the 100Å and 200Å wells respectively, in reasonable agreement with the measured values of 220ps and 240ps. The reduced difference predicted by the model between the lifetimes in the 100Å and 200Å wells in the presence of free carriers, compared to the

intrinsic exciton values (440ps and 710ps), is in particular agreement with the observed behavior. In this way, the observed reduction in radiative lifetime in the presence of degenerate free carriers may be explained by the effect of electron-hole correlation between the photocreated minority carriers and the degenerate free carrier population.

It should be noted that this reduction in lifetime would not necessarily be observed in all quantum wells, but depends on the value of the intrinsic exciton lifetime. As discussed in chapter 4, this quantity is determined by sample dependent scattering processes at low temperature from coherence area arguments. In the case of a shorter intrinsic lifetime, it could be that the loss of electron hole correlation would be sufficient to generate a net increase in PL lifetime. Furthermore, in the case of many body correlation, the coherence area arguments may no longer apply. In particular, as the temperature is raised, the electron may move to higher k-states. For an intrinsic exciton moving to higher K-states, recombination is no longer allowed when K lies outside the range of K corresponding to the homogeneous linewidth (fig. 2.2) and the radiative lifetime increases. However, for many-body correlation no such effect is expected since the electron merely becomes correlated with different holes lying at higher k-states in the hole sea. Recombination is just as likely as for lower lying hole states, as long as the holes remain degenerate. This argument allows the weaker lifetime variation with temperature to be explained for a degenerate

hole sea even in the presence of correlation. The residual effect of the absence of a Maxwell-Boltzmann term in the coherence area argument may explain the smaller lifetimes measured at 4.2K compared to those calculated.

In summary, a reduction in radiative lifetime has been observed in two single quantum wells on the introduction of free holes into the wells. The reduction has been explained by significant electron-hole correlation despite the presence of the degenerate hole sea.

5.5 Determination of the effective in-plane g-factor for electrons in a quantum well using TRPL data to complement Hanle photoluminescence studies

The initial motivation for this study was to measure the recombination lifetime in the structure as a function of electric field, to complement Hanle Photoluminescence measurements [5.7]. This magneto-optical technique allows the determination of the product of the electron g-factor and the recombination lifetime for electron-hole pairs. The g-factor for electrons in semiconductors is different from the free electron Lande g-factor and is determined by the effective mass of the electron from the band structure of the semiconductor [1.6]. Circularly polarised light is used to excite a spin polarised population of electron-hole pairs. The hole spin randomises very rapidly due to strong spin-orbit coupling within the valence band, which is p-like in character. This effect may be neglected in the s-like

conduction band. The proportion of the emitted luminescence which maintains the same circular polarisation as the excitation beam is then related to a combination of the electron spin relaxation time (T_S) and recombination lifetime (τ) in the sample. By applying a magnetic field the degree of spin polarisation and hence circular polarisation of the luminescence is reduced by Larmor precession. The variation of polarisation, P, with magnetic field, B, is given by:

$$P(B)= \frac{P(0)}{1+\Omega^2 T_T^2} \quad \text{with} \quad \Omega= \frac{g^*\mu_b B}{\hbar} \qquad \text{eqn. (5.5)}$$

where Ω is the Larmor frequency, g^* is the effective electron g-factor and μ_b is the Bohr magneton, and:

$$1/T_T = 1/\tau + 1/T_S$$

where T_S is the spin relaxation time.

If close to 100% polarisation can be achieved at B=0, ie. $\tau << T_S$, then $T_T \approx \tau P(0)$. In this case, the half width of the depolarisation curve P(B), $\delta B_{\frac{1}{2}}$, may be used to determine the product $g^*\tau$, and an independent measure of the lifetime by TRPL may therefore be used to extract the g-factor explicitly. Using eqn. (5.5):

$$g^* = \frac{\hbar}{\delta B_{\frac{1}{2}} \mu_b} \tau P(0) \qquad \text{eqn. (5.6)}$$

The theoretical value for the electron g-factor in bulk GaAs is -0.44 and +0.4 for $Al_{0.3}Ga_{0.7}As$ [5.8] . Herman and Weisbuch [5.9] have calculated the effect of band non-parabolicity on g values. Non-parabolicity significantly

affects the g-factor for narrow wells when the confinement energy is large. This treatment has been modified by Plaut [5.10] to include the effect of barrier penetration by defining an effective g-factor in the plane of the quantum well determined from the bulk values in the barrier and well materials weighted by the probabilities of finding the electron in the barrier and the well. The values generated from the combination of barrier penetration and non-parabolicity, and from non-parabolicity alone are indicated in figure 5.13, the experimental values are discussed below.

The Hanle measurements were performed at Southampton University by Harley et al. [5.2]. The sample was reverse biased so that the probability of electon recombination with a polarised photocreated hole was greatly exceeded by the probability of recombination with an unpolarised injected hole. In this way, any effect due to finite hole depolarisation time could be eliminated. The maximum Hanle depolarisation half width occured at a magnetic field of 6kG, corresponding to a cyclotron energy of one order of magnitude less than the exciton binding energy. In this case the effect of the magnetic field on the exciton wavefunction may be neglected and the lifetime values measured at zero magnetic field by TRPL are the same as those effective throughout the entire measurement regime of the Hanle PL.

Figure 5.13 also shows the g-factor values for the 100Å and 200Å wells superimposed on the theoretical curve. The uncertainty in the data originated principally from the

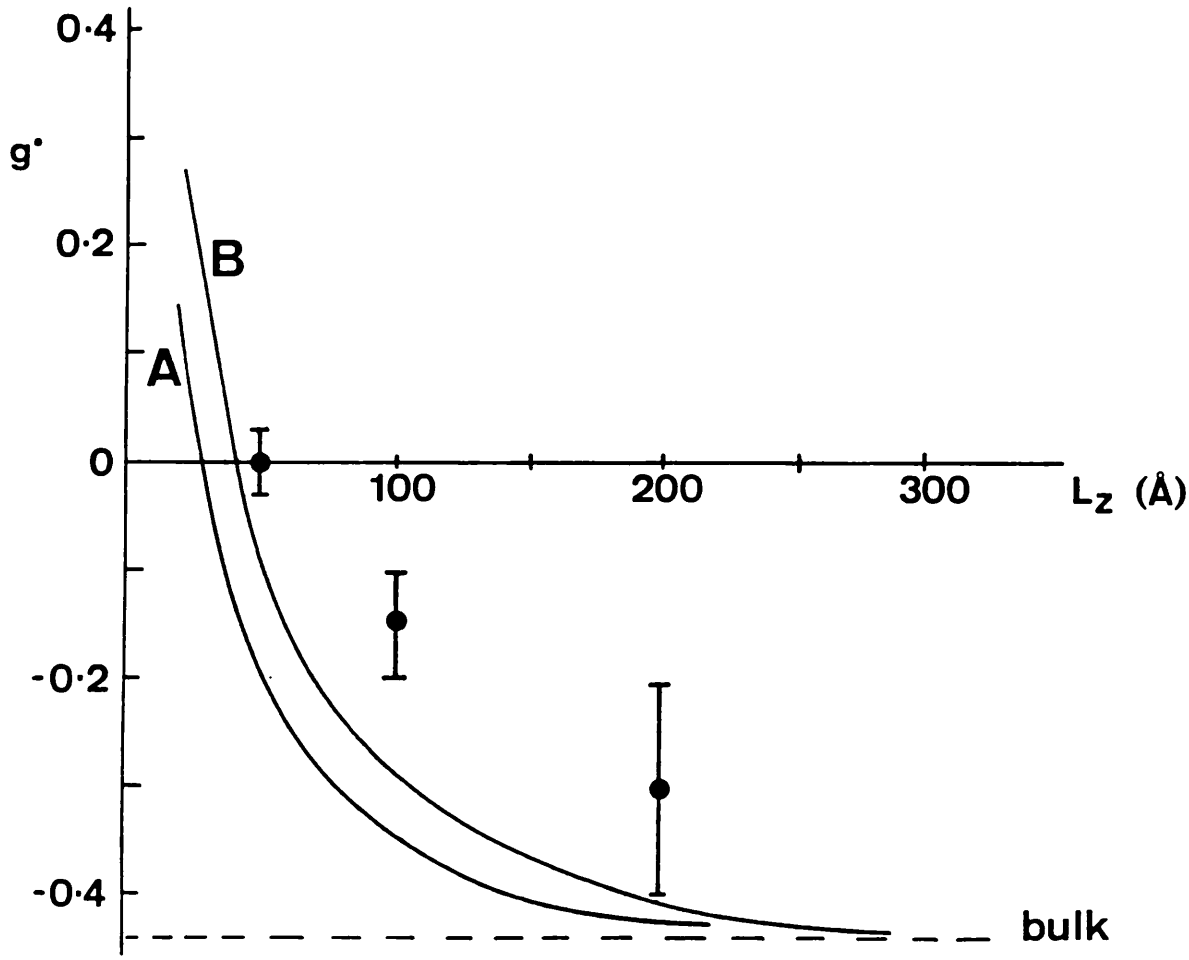


Figure 5.13 Measured values of g^* for electrons in the plane of a quantum well, as a function of well width. Curve A is the theoretical curve for free electrons in a quantum well with infinite barriers considering non-parabolicity alone. Curve B includes non-parabolicity and barrier penetration.

scatter in the Hanle measurements. The error bars indicate the total scatter in g-factor obtained from measurements at ten values of reverse bias. A statistical treatment of the data would therefore reduce the overall uncertainty in the value of g^*. No significant depolarisation was observed for the 50Å well for magnetic fields of up to 3T. The error bar in this case represents an upper limit on the value of g^*, using the maximum measured value of lifetime in reverse bias, 170ps. The 50Å data in the sample did not exhibit pronounced variations in lifetime due to free carrier behavior, possibly due to the smaller intrinsic exciton lifetime, as discussed earlier. In addition, the small Stark shifts made the value of the effective field across the well difficult to determine accurately. Consequently, the results from this well were neglected from the discussion of sections 5.2 and 5.3. Although the error bars in the measured g-factors are rather large, the expected variation in g-factor with well width is clearly established. It is noticeable that the values fall on the high side of the theoretical curve. Group theory calculations [5.2] suggest that for a single particle exciton the in-plane g-factor should be zero. The deviation of the data towards $g^*=0$ in comparison to the predicted values for free electrons is then further evidence of electron-hole correlation within the hole sea.

5.6 Conclusions

A study of the effect of the injection of free carriers into a quantum well structure as a function of electric field has been undertaken. Pronounced reductions in radiative lifetime have been observed in 100Å and 200Å single quantum wells in the presence of the free carriers. The reduction in lifetime is explained in terms of the presence of both the degenerate free carriers and significant electron-hole correlation. This interpretaion is shown to be consistent with the observed variation of PL lifetime with temperature. The weaker temperature dependence in the presence of free carriers, coupled with the observation of clear exciton resonances in PLE, is evidence for the many body nature of the electron-hole correlation.

The measured lifetimes have been used to complement Hanle PL measurements to determine the in-plane electron g-factor as a function of quantum well width. The results are in reasonable agreement with the variation with well width expected by a theory including band non-parabolicity and weighting the bulk g-factors for the well and barrier material by the probability of finding the electron in each region. The deviation of the measured values from the theory towards $g^*=0$, constitutes further evidence of electron-hole correlation in the presence of the free carriers.

CHAPTER 6 THE USE OF PHOTOLUMINESCENCE AND COMPLEMENTARY TEM MEASUREMENTS TO STUDY THE EFFECT OF ION IMPLANTATION AND RAPID THERMAL ANNEALLING TREATMENT ON A GAAS/ALGAAS MULTI QUANTUM WELL [6.1]

6.1 Introduction and Description of Sample Processing

In this chapter, CW PL studies of the effect of ion implantation and rapid thermal annealling on quantum well structures are described. The purpose was to determine the applicability of these processing techniques to quantum wells with a view to their potential incorporation in integrated optical and opto-electronic devices. Ion implantation is used as a method of applying contacts to integrated structures and rapid thermal annealling is used to remove damage induced during the implantation process. Several TEM studies of the qualitative effect of these techniques on GaAs/AlGaAs quantum wells exist in the literature [6.2][6.3][6.4]. The purpose of this study was to try to correlate quantitatively the effect of the processing on the resultant properties of the material as determined by CW PL measurements and by complementary transmission electron microscopy (TEM) data.

The sample used in this study was a nominally undoped 50 period 220Å GaAs multi-quantum well with 160Å $Al_{0.35}Ga_{0.65}As$ barriers (size 2cmx2cm square), grown on a semi-insulating GaAs substrate. CW PL measurements were made throughout this study using the Styryl-8 laser at 735nm running in CW mode

using the same optical arrangement described in section 4.3, with the exception that the luminescence was detected directly at the output of the monochromator using the cooled PMT. The wafer was divided into 6mmx3mm samples using a Unipress wire saw. The "as-grown" PL spectrum was measured from the 8 samples used in this study (denoted 7a, 7b, 6a, 6b, 2a, 2b, 3a and 3b), and in 3 locations on each sample. No significant variation in the PL spectra was found between different samples or for different locations within a given sample. The PL peak position was found to be at 815.3nm±0.1nm, with a PL linewidth of 1.90nm±0.1nm. A typical trace is shown in curve (a) of fig. 6.1 . The "a" slices were then subject to Selenium ion implantation and then rapid thermal annealled for different times at different temperatures. The "b" slices were not implanted, but annealled under the same conditions as the corresponding "a" slice in order to separate the effect of the two processes. The implantation and annealling was performed by co-workers at Surrey University. The Selenium implantation was performed at an energy of 400KeV with the samples held at a temperature of 250°C, achieving a dose of $1x10^{13}$ cm^{-2}. After implantation but prior to annealling, a 100nm thick silicon nitride (Si_3N_4) capping layer was deposited on all the samples using plasma deposition. This was done in order to prevent dissociation of the GaAs during the annealling process where the sample temperature is raised substantially above the original growth temperature of the structure. The Si_3N_4 deposition temperature was 635°C and the deposition time was 20 secs. Rapid thermal annealling was then

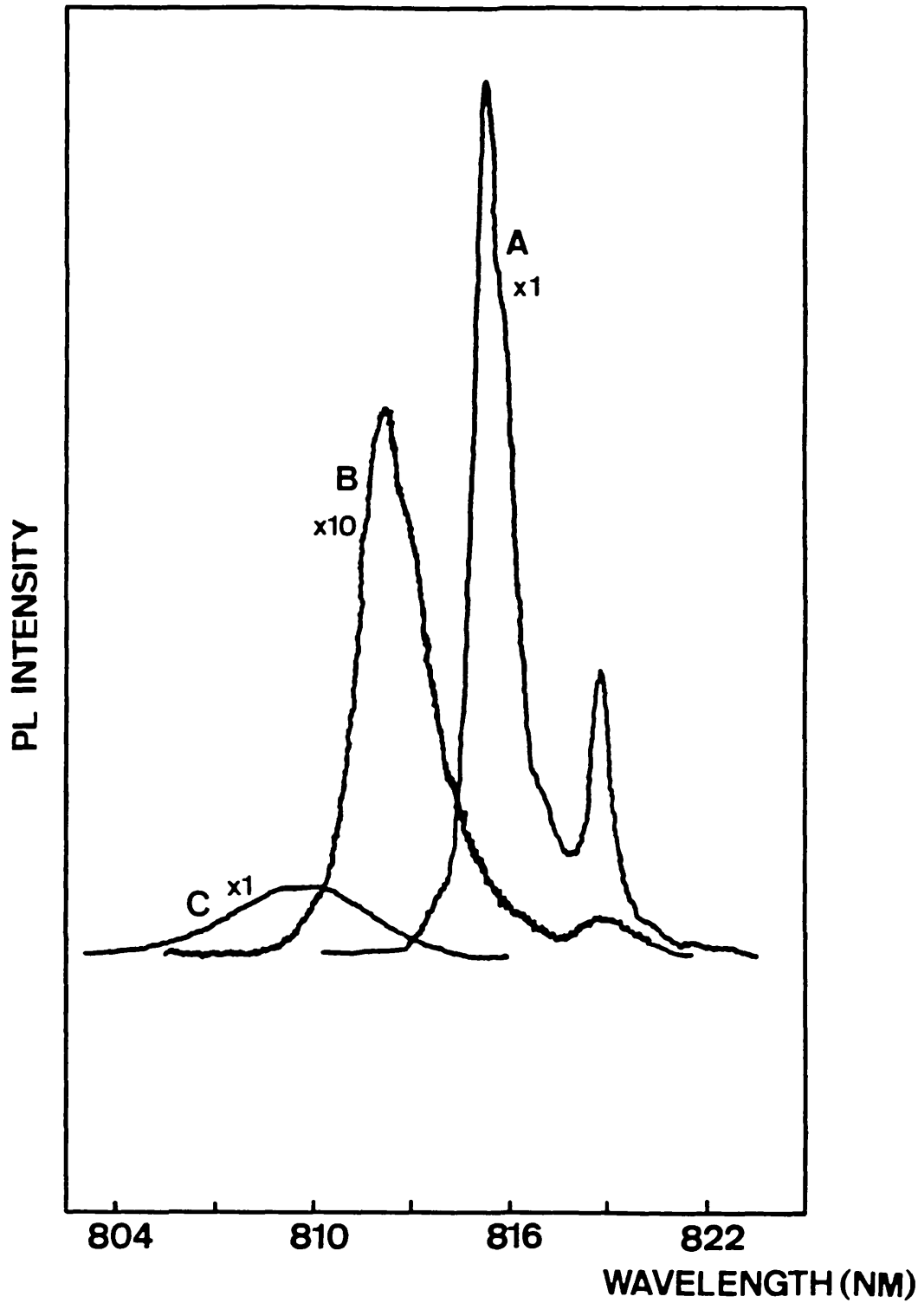


Figure 6.1 Curve a: PL spectrum obtained from the sample prior to processing. Curves b and c: Two examples of PL spectra obtained from the annealed samples: b) 3b c) 6b. Curves b and c illustrate the blue shifts in peak postion, increases in PL linewidth and reductions in luminescence efficiency obtained after processing. Temperature 4.2K.

performed using a double graphite strip heater [6.5] with a ramp time of 5 secs. The annealing treatments of the different slices are summarised as follows:

Sample	Anneal Temperature	Anneal Time
2a/2b	900°C	30sec
3a/3b	950°C	30sec
6a/6b	1000°C	30sec
7a/7b	900°C	300sec

6.2 Results of PL measurements after implantation and rapid thermal annealling treatment

Figure 6.2 summarises schematically the PL peak positions and linewidths obtained after processing. Each point represents the values obtained for excitation at a given region of the sample. The excitation spot dimensions were 100μmx650μm. The quoted linewidths exclude the instrumental resolution which has been deconvolved from the measured results assuming gaussian profiles. The percentages indicate the integrated luminescence efficiencies with respect to a piece of unprocessed wafer. The efficiency measurements were obtained by mounting each sample successively on the same part of the cold finger in order to reproduce the same PL collection efficiency from the cryostat collection optics, and by carefully maximising the signal on each occasion. The spectra were numerically integrated by computer. The results proved reproducible over 4 separate cycles of the samples to

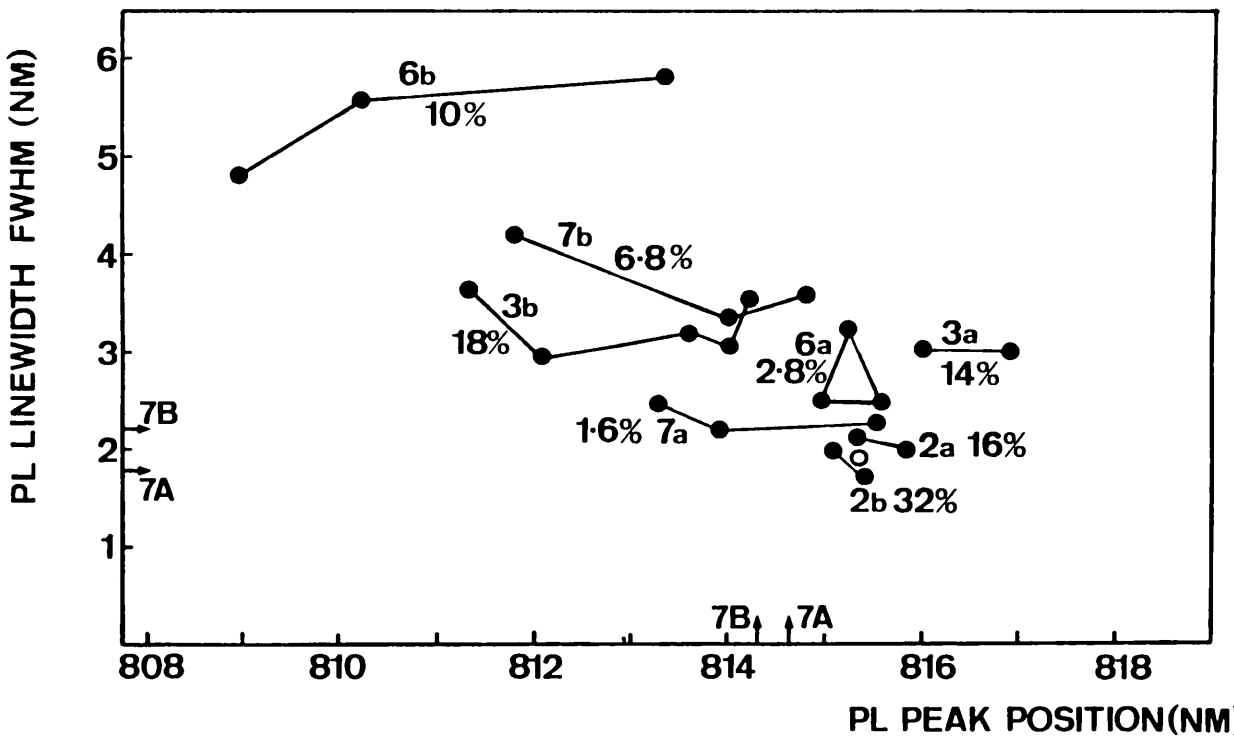


Figure 6.2 Summary of the PL linewidths and PL peak positions obtained from the samples after processing. The percentages indicate the luminescence efficiency associated with each sample relative to the as-grown wafer. Each dot represents a discrete PL spectrum. The open circle indicates the linewidth and PL peak position measured in all the samples prior to processing. The arrows indicate the calculated values of linewith and peak position (including the exciton binding energy) for samples 7a and 7b, obtained from synthesised PL spectra, as described in the text.

within ±15%. Figure 6.2 demonstrates the following results:

(1) Overall Behavior

A deviation in line position, linewidth and integrated luminescence efficiency was observed in all samples relative to the PL spectra of the unprocessed wafer. The deviation increased systematically as a function of anneal temperature. Samples 2a and 2b showed only small increases in luminescence linewidth and slight shifts in PL peak position, with the PL efficiency only reduced by around a factor of 6 and 3 respectively.

(2) PL Efficiency

All samples showed a loss in PL efficiency which increased as the annealling treatment became more severe, and which was always greater in the ion-implanted samples than in the corresponding annealed-only sample. This is attributable to transfer of non-radiative recombination centres into the well region from the surrounding AlGaAs barriers under annealing treatment. As has been previously discussed, the density of non-radiative centres is usually higher in AlGaAs due to the rather lower purity which is generally obtained in MBE growth. In the case of the implanted samples, a further loss in PL efficiency takes place due to the introduction of further non-radiative centres by implantation damage.

(3) Blue Shifts in the PL peak positions

The most severely annealled samples (6 and 7) showed

substantial blue shifts in the PL peak positions. This indicates the occurance of interdiffusion at the quantum well interfaces which mixes aluminium from the barriers into the well region, thereby raising the bandgap in the wells and reducing the effective well width. This alloy mixing was also apparant in the TEM measurements (which effectively measure the density of aluminium atoms) where a significant blurring of the quantum well interfaces were observed. The observation of alloy mixing supports the assignment of loss of PL efficiency in the annealled-only samples to motion of non-radiative centres from the barrier to the well. The implanted samples showed similar alloy mixing in TEM, but smaller blue shifts were obtained.

(4) Sample Inhomogeneity

In fig. 6.2, each dot corresponds to a single PL spectra. In the case of the samples that had received the strongest anneals (samples 6 and 7), large inhomogeneity in the PL line position was observed as the position of the excitation spot was varied. As indicated in fig. 6.2, in the case of 6b, a variation in peak position of 4.5nm was observed. However the FWHM linewidth in a given sample showed less variation, varying only over 1nm. Suprisingly, the implanted and annealled samples showed less inhomogeneity than the annealled only samples, implying that the inhomogeneity was induced by the anneal, but reduced by the presence of the implant. This effect is not explicable in terms of the PL efficiency loss, since it refers to a variation between different parts of the entire sample which are assumed to

receive the same implant damage and exhibit the same measured efficiency values.

(5) PL linewidth

In the same way, the PL linewidth increased for larger anneal temperatures and times. Again, larger linewidths were obtained for the annealled only samples in comparison to the corresponding implanted and annealled sample.

In summary, as the severity of the annealling treatment was increased, a tendency towards smaller PL efficiency, and larger PL linewidths, blue shifts and inhomogeneity was observed. Smaller PL efficiencies were observed in the implanted samples, as expected from the introduction of non-radiative centres by the implantation process. However, in terms of PL linewidth, peak position and sample inhomogeneity, the annealled only samples suprisingly exhibited the greater deviation from the as-grown wafer. The reduced blue shifts, linewidths and sample inhomogeneity in the implanted samples might suggest that the regions which particularly contribute to larger values of the above parameters in the annealled only samples lie near the surface so that in the case of the implanted samples, the PL in this region is destroyed by implant damage, thereby generating the reduced values which are observed. However, the evidence of the TEM data from the annealled-only samples shows that the annealling process produces an effect on the well profiles which is uniform throughout the depth of the sample, so that the quenching of the PL efficiency close to

the surface would not be expected to generate different PL lines, only reduced PL efficiency.

6.3 Quantitative comparison of the PL spectra with the TEM measurements

To investigate these effects further, and to attempt quantitative correlation of the PL results with the TEM measurements, calculations were made of the expected PL spectra based on the well profiles obtained from microdensiometry measurements of the TEM micrographs of samples 7a and 7b. The TEM measurements were made by co-workers at Cambridge University. Such measurements are capable of determining the aluminium mole fraction, x, through the sample to within ±0.03 [6.5]. The spectra were generated by using the TEM profiles to produce a 1D effective mass Hamiltonian for the confined electron and hole states (eqn. (2.10)), and numerically solving the resulting Schroedinger equation to obtain the free carrier ground state transition energy in the n=1 subband, and assuming an exciton binding energy of 6.8meV for a well of this width [6.6][2.9]. The contributions from the transitions in each well were then scaled to account for the absorption depth of the pump radiation using an absorption coefficient of $1.1 \times 10^{6} m^{-1}$ [1.2] and a luminescence reabsorption of $5 \times 10^{5} m^{-1}$. These weighted peak energy values were then convolved with the inhomogeneous linewidth measured in the as grown samples to obtain theoretical PL spectra from the TEM profiles. Figure 6.3 shows the

calculated spectra obtained for the implanted sample 7a. The very large blue shifted peaks (≈20nm) due to the wells close to the surface where large alloy mixing has occured due to the effect of the implant were not found in the measured PL spectra, and may be assumed to be those where the PL efficiency has been extinguished by the implant. The spectrum was therefore weighted by a profile of non-radiative centres which decays exponentially into the sample with a 1/e depth taken from Monte-Carlo simulations of the energy deposition profile of the Se implants in the MQW calculated at Surrey University (fig. 6.4). The profile indicates that the density of non-radiative centres (which is assumed to be proportional to the energy deposition) decays exponentially into the sample with a 1/e depth corresponding to four wells. The magnitude of the effect of the defects on the PL efficiency, which is governed by the ratio of the non-radiative lifetime to the radiative lifetime, was chosen to obtain the measured PL efficiency difference between the implanted and annealled-only samples when the effect of the defect profile was integrated throughout the structure. The inclusion of this factor was found to remove the higher energy lines from the spectrum, generating the final spectrum of figure 6.5. Figure 6.6 shows the corresponding spectrum for the unimplanted sample 7b. As expected, in both cases the spectra are blue shifted compared to the results from the as-grown samples. The peak positions are indicated by the arrows in fig. 6.2, and fall within the spread of measured values. However, the measured linewidths are significantly larger than those calculated by

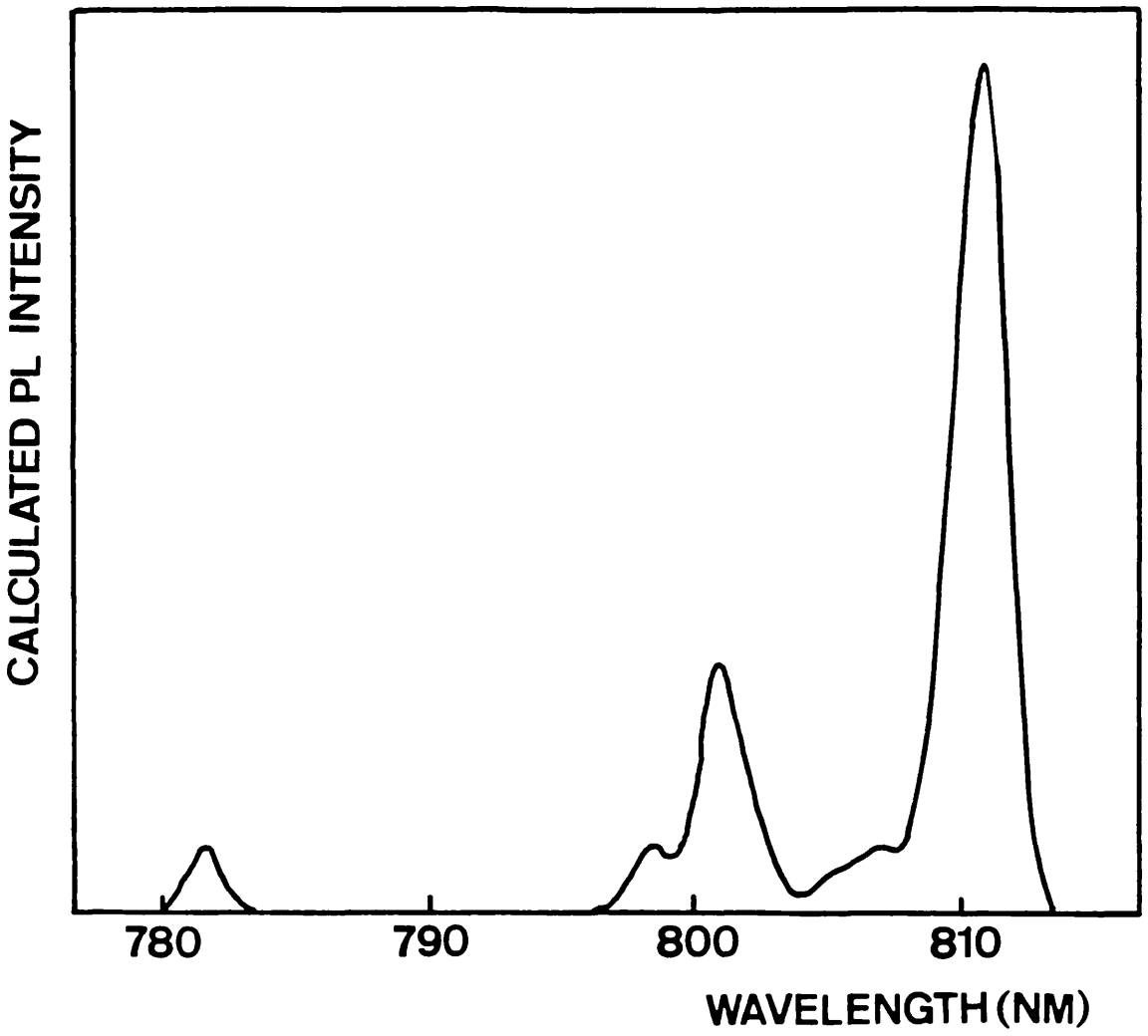


Figure 6.3 Synthesised PL spectrum for sample 7a (neglecting the exciton binding energy) calculated assuming constant luminscence efficiency throughout the sample.

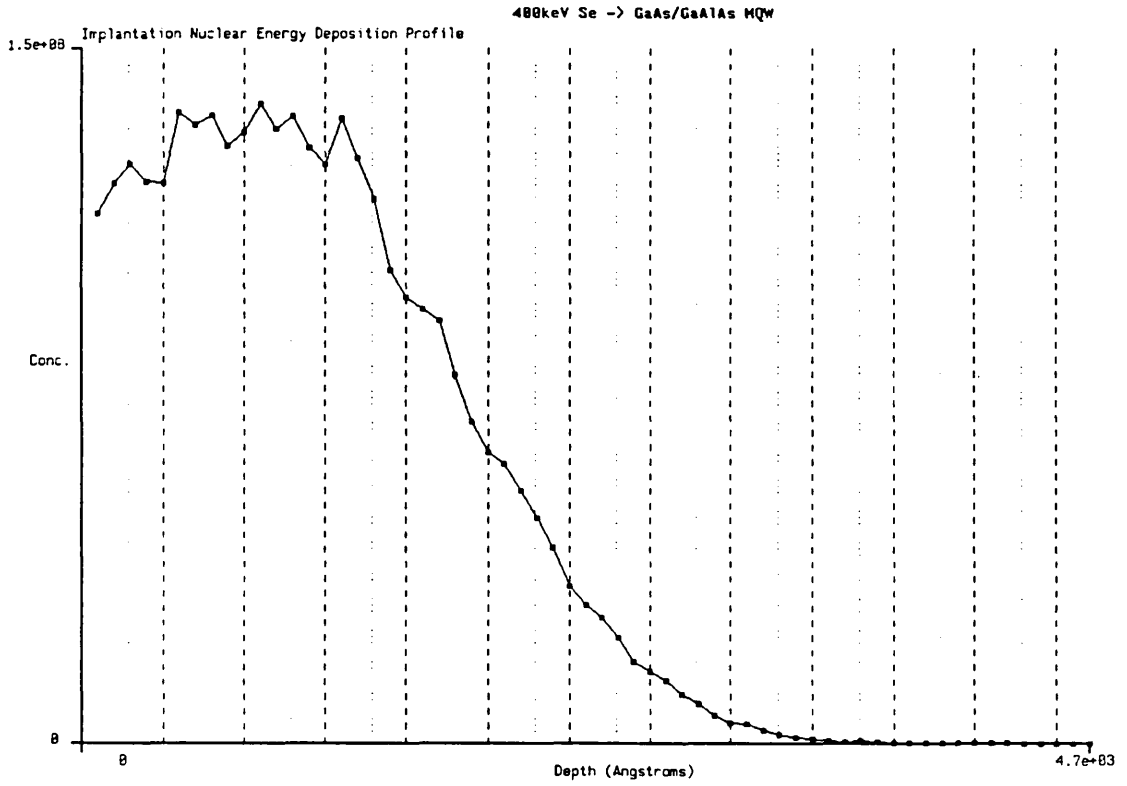


Figure 6.4 Energy deposition profile of the Se implant as a function of distance from the sample surface, as calculated by a Monte Carlo simulation (R.Gwilliam Surrey University). The wider regions (bounded on the left by the dashed vertical lines) correspond to the locations of the GaAs wells. Most of the energy is deposited within the region occupied by the first four wells.

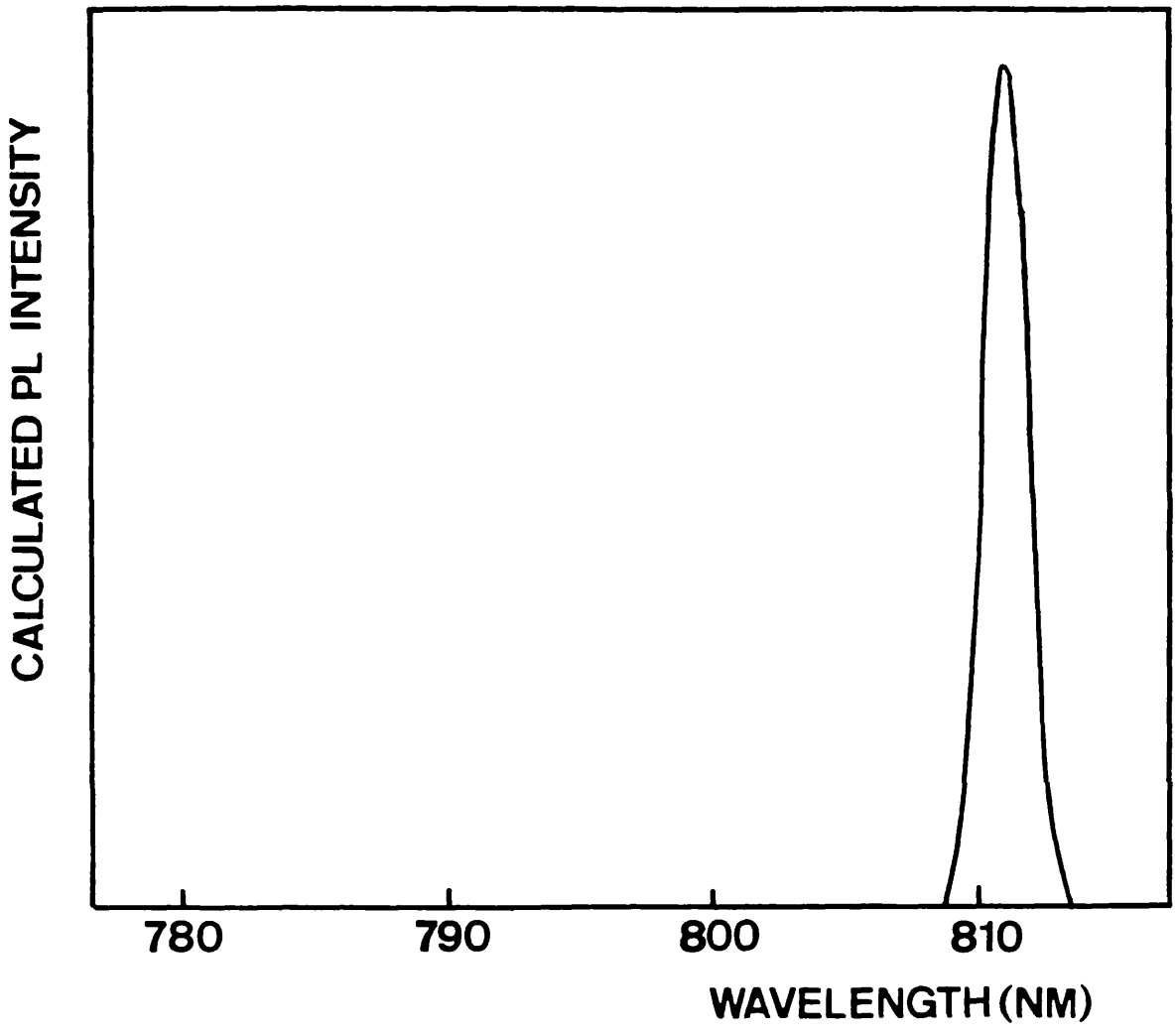


Figure 6.5 Synthesised PL spectrum for sample 7a (neglecting the exciton binding energy) assuming a concentration of non-radiative recombination centres decaying exponentially from the sample surface with a 1/e depth of equivalent to four wells.

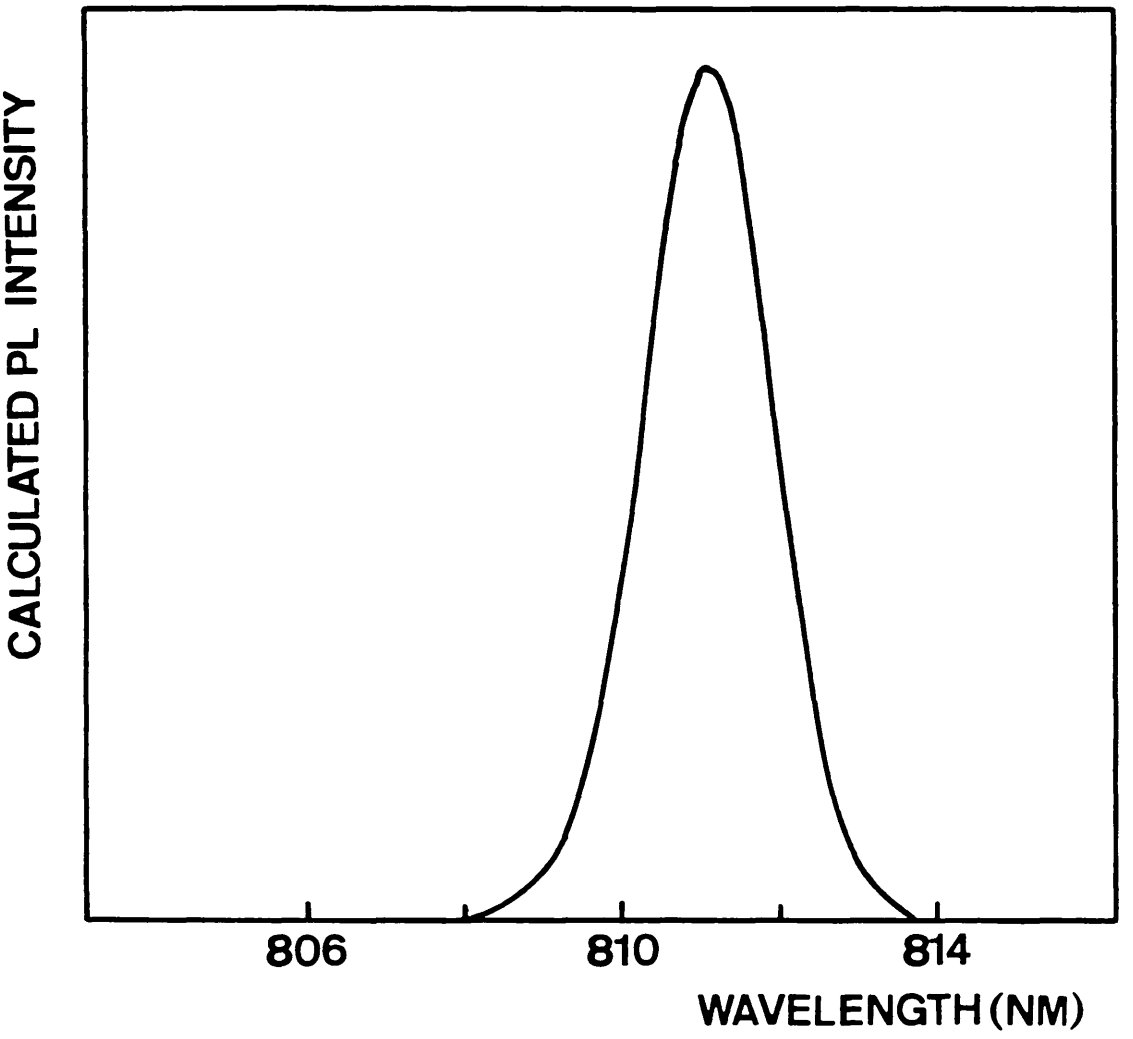


Figure 6.6 Synthesised PL spectrum for sample 7b (neglecting the exciton binding energy) calculated assuming constant PL efficiency throughout the sample.

(also indicated by arrows in fig. 6.2) using the inhomogeneous linewidths from the as-grown samples, implying that some additional broadening mechanism was introduced by the processing.

The broadening mechanism is consistent with the presence of an inhomogenous strain field produced by differential expansion between the silicon nitride capping layer and the MQW during the rapid thermal annealling process. Using [6.7]:

$$\frac{-a}{\delta a}\,\delta E_g = 21.62\text{eV} \qquad \text{eqn. (6.1)}$$

where a is the lattice constant and E_g is the bandgap. Eqn. (6.1) implies that an rms. inhomogeneous strain field of only 0.013% in 7a and 0.035% in sample 7b within the area of the excitation spot would be required to generate the observed PL line broadening. Larger values of strain are required across the sample to generate the large inhomogeneous blue shifts. The presence of such a strain field is in fact implied by the large inhomogeneity in the PL peak position observed in these samples, but is confirmed by the complementary TEM measurements and PL simulations.

The larger values of sample inhomogeneity, PL linewidth and blue shift in the annealled-only samples indicate that the implanted samples experience less strain in the region where the PL originates than the total strain of the corresponding annealled only sample. This behavior is consistent with the disordered region at the surface of

the implanted samples acting to accommodate the differential expansion between the sample and the capping layer, thereby reducing the strain further away from the surface. In this way, the implanted samples experience less strain in the region where the PL is generated, resulting in the smaller sample inhomogeneity, PL linewidths and blue shifts which are observed.

6.4 Conclusions

This study has demonstrated the use of complementary photoluminescence and TEM measurements, together with Monte Carlo simulations of implantation profiles, to obtain a consistent picture of the effect of ion-implantation and rapid thermal annealling on a multi-quantum well structure. A general trend towards greater alloy mixing at the hetero-junctions resulting in blue shifts in the PL emission of up to 6nm and larger PL linewidths of up to 6nm have been identified. However, samples treated at 900°C were shown to have values of PL linewidth and peak position which deviated by less than 0.2nm and 0.5nm respectively from the as-grown values, despite being processed at temperatures which greatly exceeded the growth temperature of the structure. Nevertheless, even these samples suffered at least a factor of 3 reduction in PL efficiency. In addition, the PL and TEM measurements were combined quantitatively in order to explain the anomalous reduction in the effect of annealling by prior implantation treatment. The combination of the two techniques has been used to demonstrate the presence of

inhomogeneous strain induced by differential expansion between the silicon nitride capping layer and the GaAs epilayers. In this way, the behavior of each sample pair at a given temperature was shown to be due largely to the effect of the anneal treatment. However, the relative behavior of the implanted and annealled-only samples for a given anneal was shown to be principally due to the capping layer. The large effect of the silicon nitride cap in this study is indicative of the inavailability of a truly ideal capping layer for thermal treatment of GaAs: the search for such a capping layer is in fact an area of active current research. In these implantation trials, the significant effect of the capping layer has been shown, and the value of complementary quantitative TEM and PL measurements as a means of studying effects of this nature has been demonstrated.

REFERENCES

Chapter 1

[1.1] D.A.B.Miller, J.S.Weiner and D.S.Chemla IEEE J. Quan. Elec. 22 (1984) 1816.

[1.2] D.S.Chemla (ed.) special issue J.Opt.Soc.Am. 2B (1985).

[1.3] M.J.Kelly and R.Nicholas, Rep.Prog.Phys. 48 (1986) 1699.

[1.4] R.Dingle Festkorperprobleme XV (1975) 21.

[1.5] F.Wooten in "Optical Properties of Solids" Academic Press (1972) 108.

[1.6] K.Seeger in "Semiconductor Physics" Springer-Verlag (1985) 337.

[1.7] C. Kittel in "Quantum Theory of Solids." Wiley (1963) 298.

[1.8] M.Shinada and S.Sugano J.Phys.Soc.Jap. 21 (1986) 1936.

[1.9] D.A.B.Miller,D.S.Chemla, T.C.Damen, A.C.Gossard, W.Weigmann, T.H.Wood and C.A.Burras Phys.Rev.Letts. 53 (1984) 2173.

[1.10] For a review see J.Shah IEEE J.Quan.Elec. QE22 (1986) 1728.

[1.11] D.L.Dexter Solid State Physics Vol.6 (1959).

Chapter 2

[2.1] J.Christen and D.Bimberg Surf. Sci. 174 (1986) 261.

[2.2] T.Matsusue and K.Sakaki Appl.Phys.Lett. 50 (1987) 1429.

[2.3] D.A.B. Miller, D.S.Chemla, T.C.Damen, A.C.Gossard, W.Weigmann, T.H.Wood and C.A.Burras Phys.Rev. B32 (1985) 1043.

[2.4] G.Bastard, E.E.Mendez, L.L.Chang and L.Esaki Phys.Rev. B28 (1983) 3241.

[2.5] S.Hong and J.Singh J.Appl.Phys. 61 (1987) 5346.

[2.6] E.J.Austin and M.Jaros Phys.Rev. B31 (1985) 5569.

[2.7] E.J.Austin and M.Jaros J.Phys.C 19 (1986) 533.

[2.8] G.D.Saunders and K.K.Bajaj Phys.Rev. B35 (1987) 2308.

[2.9] G.Bastard, E.E.Mendez, L.L.Chang and L.Esaki Phys.Rev. B26 (1982) 1974.

[2.10] J.A.Brum and G.Bastard Phys.Rev. B31 (1985) 3893.

[2.11] S. Nojima Phys.Rev. B37 (1988) 9087.

[2.12] J.Feldmann, G.Peter, E.O.Gobel, P.Dawson, K.Moore, C.Foxon and R.J.Elliot Phys.Rev.Letts. 59 (1987) 2337. Also Errata Phys.Rev.Lett. 60 (1988) 243.

[2.13] J.Lee, E.S.Koteles and M.O.Vassell Phys.Rev. B34 (1986) 8.

[2.14] L.Schultheis, A.Honold, J.Kuhl and K.Kohler Phys.Rev. 34 (1986) 9027.

[2.15] Y.J.Chen, E.S.Koteles, B.S.Elman and C.A.Armiento Phys.Rev. B36 (1987) 4562.

[2.16] S.R.Andrews, C.M.Murray, R.A.Davies and T.M.Kerr Phys.Rev. B37 (1988) 8198.

[3.1] R.Eccleston and C.C.Phillips J.Phys.E (in press).

[3.2] P.W.Smith, M.A.Duguay and E.P.Ippen Rep.Prog.Quan.Elec. 3 (1968) 1.

[3.3] M.C.Adams, W.Sibbett and D.J.Bradley Advances in Elec. and Elec. Phys. 52 (1979) 265.

[3.4] Dye Lasers ed. E.P.Schafer "Topics in Applied Physics Vol.1" Springer-Verlag.

[3.5] A.Yariv in "Quantum Electronics" 2nd. Edition. Wiley (1975).

[3.6] C.C.Davies and T.A.King in "Advances in Quantum Electronics" Vol. 3 Academic Press (1975).

[3.7] Series 2000 Ion Laser System Manual. Spectra Physics, 1250 W. Middlefield Road, Mountain View, CA 94042-7303, USA.

[3.8] J.J.L.Mulders and L.W.G.Steenhuysen Opt.Comm. 54 (1985) 295.

[3.9] 375B Dye Laser Manual. Spectra Physics, 1250 W. Middlefield Road, Mountain View, CA 94042-7303, USA.

[3.10] Applications note. IQD Ltd, North Street, Crewkerne, Somerset. TA18 7AR.

[3.11] D.J.Bradley, J.McInerney and W.M. Dennis Opt.Comm. 44 (1983) 357.

[3.12] W.E.Sleat, W.Sibbett, J.R.Taylor and D.J.Bradley Opt.Comm. 45 (1983) 411.

[3.13] "Photomultipliers" Thorn EMI Electron Tubes Ltd. Bury Street, Ruislip. Middlesex. HA4 7TA.

[3.14] "Solid State Multichannel Detectors" B+M

Spectronik Ltd.

[3.15] "BM 590CD" B+M Spectronik Ltd.

Chapter 4

[4.1] J.A.Kash, E.E.Mendez and H.Morkoc Appl. Phys. Lett. 46 (1985) 173.

[4.2] H.J.Polland, L.Schultheis, J.Kuhl, E.O.Gobel, and C.W.Tu Phys.Rev.Lett. 55 (1985) 2610.

[4.3] K.Kohler, H.J.Polland, L.Schultheis and C.W.Tu Phys.Rev. B38 (1988) 5496.

[4.4] Y.Masumoto, S.Shionoya and H.Kawaguchi Phys.Rev. B29 (1984) 2324.

[4.5] J.F.Ryan, R.A.Taylor, A.J.Tuberfield, A.Maciel, J.M.Worlock, A.C.Gossard and W.Weigmann Phys.Rev.Lett. 53 (1984) 1841.

[4.6] J.D.Dow and D.Redfield Phys.Rev. B1 (1970) 3358.

[4.7] R.C.Miller and D.A.Kleinmann J.Luminescence 30 (1985) 520.

[4.8] A.S.Plaut, J.Singleton, R.J.Nicholas, R.T.Harley, S.R.Andrews and C.T.B.Foxon Phys.Rev. B38 (1988) 1323.

[4.9] D.A.Broido and L.J.Sham Phys. Rev. B34 (1986) 3917.

[4.10] C.Priester, G.Allen and M.Lunnoo Phys.Rev. B30 (1984) 7302.

[4.11] T.Takagahara Phys.Rev. B32 (1985) 7013.

Chapter 5

[5.1] G.Peter et al. Topical Meeting on Quantum wells for

Optics and Optoelectronics, 1989 Technical Digest Series Vol. 10. (Optical Society of America, Washington D.C.).

[5.2] R.T.Harley, A.S.Plaut and G.Flynn (unpublished)

[5.3] M.K.Saker, M.S.Skolnick, P.A.Claxton, J.S.Roberts and M.J.Kane Semicond.Sci.Tech. 3 (1988) 691.

[5.4] T.Ando, A.Fowler and F.Stern Rev.Mod.Phys. 54 (1982) 437.

[5.5] A.L.Fetter Annals of Physics 88 (1974) 1.

[5.6] D.A.Kleinmann Phys.Rev. B32 (1985) 3766.

[5.7] R.R.Parsons Phys.Rev.Lett. 23 (1969) 1152.

[5.8] C.Weisbuch and C.Hermann Phys.Rev. B15 (1977) 816.

[5.9] C.Hermann and C.Weisbuch Phys.Rev. B15 (1977) 823.

[5.10] A.S.Plaut Ph.D. Thesis Oxford (1988)

Chapter 6

[6.1] E.G.Bithell, C.C.Phillips, R.Gwilliam, R.Eccleston and W.M.Stobbs (submitted to J.Appl.Phys.)

[6.2] J.J.Coleman, P.D.Dapkus, C.G.Kirkpartick, M.D.Camras and N.Holonyak Appl. Phys. Lett. 40 (904) 1982

[6.3] D.G.Deepe, L.J.Guido, N.Holonyak, K.C.Hsieh, R.D.Burnham, R.L.Thorton and T.L.Pauli Appl. Phys. Lett. 49 (510) 1986

[6.4] J.Ralston, G.W.Wicks, L.F.Eastman, B.D.de Cooman and C.B.Carter J.Appl.Phys. 59 (120) 1986

[6.5] E.Bithell and W.M.Stobbs Phil.Mag. A (1989) (in press).

[6.6] R.L.Greene and K.K.Bajaj Solid State Comm. 45 (1983) 831.

[6.7] D.Olego, M.Cardona and H.Muller Phys.Rev. B22 (1980) 894.